博士論文

Development and biosensing application of organic electrochemical transistors with highly conductive PEDOT:PSS:Poly(acrylamide)-based hydrogel channels

(高導電性PEDOT:PSS:Poly(acrylamide)ハイドロゲルをチャネルとした有機電気化学トランジスタの開発およびバイオセンシング応用)

Alex Chi-Wei Tseng

セーン　アレックス　チ　ウェイ

Abstract

Sensors built on smart, functional materials pave the way for democratized health care by providing high quality personal health data at the point-of-care. In the aftermath of the novel coronavirus pandemic, the need to advance such technologies is salient. The required materials must be mediators of electronic and ionic transport, mechanically compliant and flexible, and crucially, chemically stable and biocompatible. Hydrogels of semiconducting conjugated polymers (CPs) fit this profile exceptionally well.

PEDOT:PSS (poly(3,4-ethylenedioxythiophene) polymerized with poly(styrene sulfonate)) is one of the most widely studied CPs for technological applications, and it can be formed into hydrogels by a variety of processing methods. In this regard, the formation of composite hydrogels by interpenetrating a second polymer network is highly promising for biosensing, because of the capability for orthogonal design of electrical, electrochemical, and mechanical properties.

In this thesis, we successfully prepared double-network composite hydrogels by facile one-pot free radical polymerization of neutral and anionic acrylamide monomers dispersed into commercial-grade PEDOT:PSS. The resulting free-standing hydrogel sheets are highly conductive in the dry state and remain so when re-swelled ($\sim$20 S/cm) in analogues of physiological media (i.e., phosphate buffered saline). These outstanding properties allowed organic electrochemical transistors (OECTs) and typical electrochemical electrodes to be readily fashioned by manual forming, with low resistance ohmic contacts to Au electrodes formed by simple thermo-mechanical annealing.

Electrical transport and electrochemical characterization revealed that, while volumetric capacitances were reduced by the non-conductive second network, carrier mobilities were essentially unimpeded from that of neat PEDOT:PSS ($\sim$1 $\mathrm{cm}^2/(\mathrm{V\,s})$) indicating good compatibility between the two phases. Reliable contacts also allowed us to investigate the kinetics of electrocatalyzed reduction of dissolved O_2 on PEDOT and informed an optimal potential sweep rate to balance Faradaic and capacitive currents in the cathodic regime of operation.

Accordingly, we applied these highly conductive hydrogels towards the detection of glucose, by extracting an electrochemical signal based on the coupling of PEDOT electrocatalytic action to the boronic-boronate acid equilibrium in the presence of diol molecules. These signals could be directly amplified by using the hydrogel as the channel of an OECT—a departure from the traditional embodiment of OECT biosensors.

Finally, we observed novel redox-mediated resistance switching effects in these CP hydrogels, due to the coupling of electro-mechanical swelling of the interpenetrating second network and the formation of electronic band structure in PEDOT. This effect could be induced by surface modification of the current collecting electrodes, suggesting that the accumulation of space charge when the channel resistance is of similar magnitude to the contact resistance. Redox-mediated, reversible box-shaped hysteresis loops in various device configurations suggest the application of this phenomena in new bioelectronic devices.

Acknowledgements

This dissertation is presented in fulfillment of the requirements for the degree of Doctor of Philosophy granted by the Department of Materials Engineering, Graduate School of Engineering, at The University of Tokyo.

Herein describes the work that I undertook in the three years from April 2019 to March 2022 under the supervision of Associate Professor Toshiya Sakata. To him I am profoundly grateful, for his support of my work, insights, and his belief in my capacity even in the moments when I failed to believe in myself.

I would also like to thank the members of my committee, Professor Ryo Yoshida, Associate Professors Aya Akimoto, Yuichi Yamasaki, and Tomoyuki Yokota (Electrical Engineering) for their encouragement and interest in my work. From them I realized the value of multi-disciplinary collaboration for the future of materials research. Additionally, I am thankful for the financial support provided by a Ministry of Education, Culture, Sports, Science and Technology of Japan (MEXT) scholarship as it allowed me to focus solely on my studies.

Of course, no graduate student (or researcher, for that matter) should ever walk alone. Therefore, I express my gratitude for the staff and students in Sakata Laboratory. Their hard work ethic provided a constant stream of engaging topics to discuss and learn during our seminars. I especially thank Akiko Saito-san for her gracious assistance with sorting out matters both inside and outside the lab. Most importantly, I would not have made it to the finish line without the support of all lab members.

During my time in Tokyo, helped in no small part by the pandemic circumstances, I came to an intimate understanding of my own mental and social limitations. Thus, to the friends back home and new ones made along the way, I am thankful because your companionship has kept me sane. Finally, to my family; your unconditional love and ceaseless prayers continue to be my help and foundation. Thank you.

Alex Chi-Wei Tseng
March 2022

Contents

List of Figures

List of Tables

List of Abbreviations

g_m	transconductance, $g_m = \frac{\partial I_D}{\partial V_G}$
AAm	acrylamide
AAPBA	3-(acrylamido)phenylboronic acid
AMPS	2-acrylamido-2-methylpropanesulfonic acid
CE	counter electrode
CP	conductive polymer
CSC	charge storage capacity
CV	cyclic voltammetry
DI water	de-ionized water
DN	double-network (polymer)
EDC	1-ethyl-3-(3-dimethylaminopropyl) carbodiimide
EDL	electric double layer
IPN	interpenetrating network (polymer)
IS	(electrochemical) impedance spectroscopy
ISFET	ion-sensitive field-effect transistor
MBA	N-N'-methylenebisacrylamide
OCP	open circuit potential
OECT	organic electrochemical transistor
ORR	O_2 reduction reaction

PBA	phenylboronic acid
PBS	phosphate buffered saline
PDMS	poly(dimethylsiloxane)
PEDOT:PSS	poly(3,4-ethylenedioxythiophene):poly(styrene sulfonate)
RE	reference electrode
SAM	self-assembled monolayer
WE	working electrode

Chapter 1

Introduction

1.1 Motivation

Bio-electronic sensors built on smart, functional materials pave the way for democratized health care by providing high quality personal health data at the point-of-care [1, 2]. These provide the biological inputs that, when combined with emerging information technologies such as artificial intelligence [3], form the tools that output essential knowledge about our bodies and improve our understanding and decision-making regarding our physical well-being. An ubiquitous example is the hand-held glucose monitor based on the electrochemical signal produced by enzymatic reaction of blood glucose with glucose oxidase [4], which, despite decades of research in the field of biosensing, remains one of the few examples of successful application.

In the aftermath of the novel coronavirus pandemic of 2020, a need to advance such technologies is salient. These novel biosensors require materials that satisfy three key requirements, being that they must:

1. mediate between energy and mass transport; that is, they must ultimately couple biological and biomolecular activity to readily measurable quantities. While biosensing may be performed electromagnetically (i.e. optically) [5], electro-mechanically [6, 7], and electrochemically [4, 8], the latter is arguably the most amenable to miniaturization and hence, deployment.

2. be mechanically compliant and flexible, to interface with biological systems. This is emphasized in systems deployed for chronic use *in vivo*, as mediating the body's inflammatory response is critical to avoid a rejection reaction [9].

3. be chemically stable and biocompatible, to operate reliably and—whether directly by decomposition, or indirectly by false information—prevent harm to the user.

Hydrogels comprised of semi-conducting organic polymers fit this profile exceptionally well [10]. For instance, their electrochemical state can be controlled electrically and by interaction with the environment; their high composition of water enhances ionic mobility; and their mechanical and other properties can be tuned by composition and microstructure. Together, these advantages form the key motivators for this thesis.

1.2 Background

1.2.1 Conductive polymers

From the discovery of the semi-conducting property of polyacetylene in 1977 [11, 12], conductive polymers (CPs) have been viewed with great promise for bio-electronic applications [2, 13], in addition to other fields such as flexible, transparent conductors in displays and solar panels [14], energy generation (e.g. photoelectric [15], photocatalytic [16], and thermoelectric [17]), energy storage [18, 19], and as electrochromic panels [20].

Generally, CPs consist of long chains of conjugated molecules (poly- pyrrole, aniline, thiophene, etc.) as physical structure can be maintained through σ-bonded monomer units[1], while electronic band structure arises in π-bonding molecular orbitals [21]. This produces the physical properties that drive the technological developments noted above; namely, a large energy difference between electronic states in the highest occupied and lowest unoccupied molecular orbitals (HOMO-LUMO gaps) and the ability to form states in the mid-gap upon partial oxidation (reduction) of the CP chain. The formation of these states is often referred to as p- (n-) type doping, by analogy with solid state terminology; however, there are fundamental differences in that "dopants" need not be fixed in the structure of the CP and can be provided chemically or electrochemically at the time of device operation [22]. This is an important aspect for using CPs as electronic sensors, because their conductivity is inherently related to their (electro)chemical interaction with the environment.

In practice, a majority of CPs are p-type semi-conductors because it is simpler to remove electrons from de-localized π orbitals than the inverse, as shown in Eq. (1.1). Considering that the liberated electron will be transferred to an oxidizing agent or electrode, an anionic species must be brought into close contact to the oxidized monomer to maintain electroneutrality.

$$\mathrm{CP^o} \overset{\text{ox. agent}}{\rightleftharpoons} \mathrm{CP^+} + \mathrm{e^-} \tag{1.1}$$

[1]Polyacetylene is an interesting exception, as the main chain includes π-bonds which gives degeneracy in the doped band-structure, but also increases its chemical reactivity (i.e. poor stability in air)

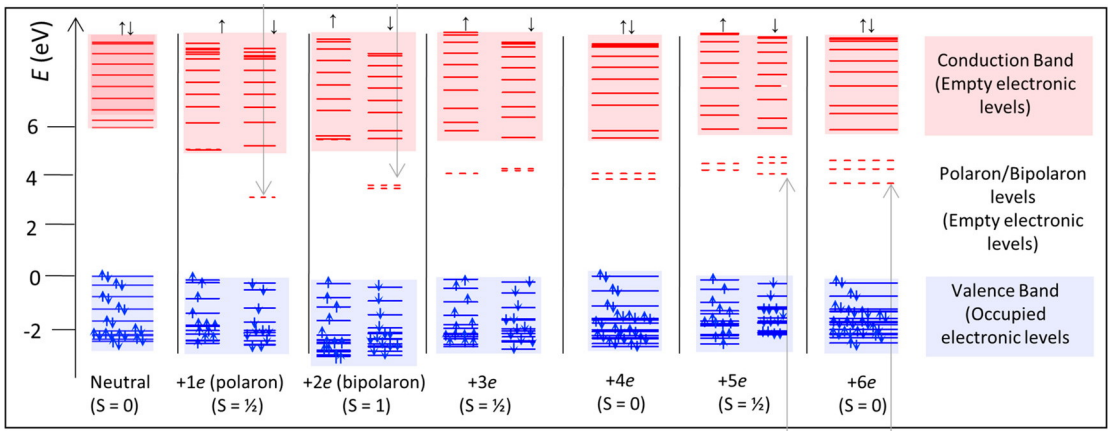

Figure 1.1: Band diagram for polaron and bipolaron states in PEDOT with increasing oxidation, as determined by DFT simulations. Adapted with permission from [23]. Copyright 2019 American Chemical Society.

At the same time, for the positive charge of CP^+ to become mobile, its wavefunction must be de-localized over the entire polymer chain. That is, the formation of a hole in the valence band by excitation of an electron into the conduction band. In inorganic materials with a high degree of crystallinity, this process is straightforward because of overlapping atomic orbitals; however, polymers are semi-crystalline at best, with regions of high and low disorder serving to make long range de-localization energetically unfavourable.

Rather, the charge of CP^+ becomes locally "de-localized" over the overlapping $\pi - \pi$ orbitals of a few (3) monomer units by the deformation of the polymer chain [21]. This accommodation strongly couples the molecular conformation with the electronic state, i.e. phonon-electron coupling, giving a polaron quasiparticle as a positive charge carrier. With increasing oxidation, the formation of coupled polarons, so-called bipolarons, becomes even more energetically favourable despite Coulombic repulsion. These polaronic states exist in the mid-gap and overlap to form unfilled bands, as depicted in Fig. 1.1. While the exact nature of polaronic and bipolaronic bands in CPs (and the transition between them with oxidation state) remains a topic of discussion [23], both seminal and modern studies demonstrate the existence of mid-gap bands that allow highly doped/oxidized CPs to realize near-metallic degrees of conductivity.

PEDOT:PSS

PEDOT:PSS (poly(3,4-ethylenedioxythiophene) complexed with poly(styrene sulfonate)) has emerged as one of the most widely studied CPs for technological application, demonstrating excellent chemical stability [24] in addition to high conductivity (cf. 1 to 10^3 S/cm) that may be readily optimized [25–27] and deployed as thin-films by solution-based pro-

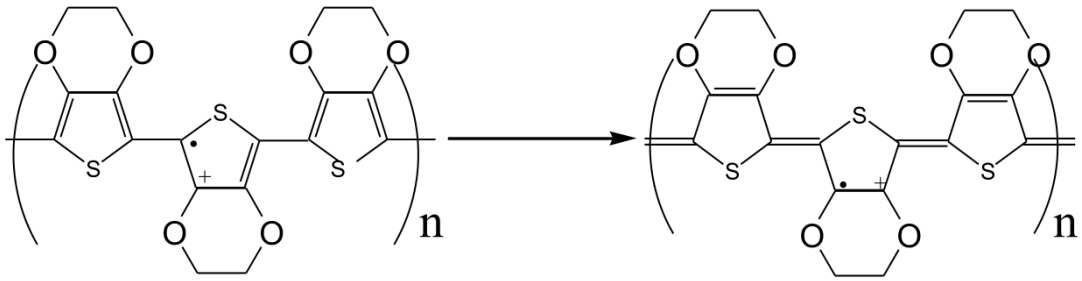

Figure 1.2: Molecular structure of PEDOT undergoing oxidation reaction. An unpaired electron and positive charge on the PEDOT chain are represented by a 'dot' and 'plus' sign, respectively. Reprinted with permission from [27]. Copyright 2004 Elsevier.

cessing. Note that as preparation for the main body of work in this thesis, thin-film PEDOT:PSS devices were fabricated and characterized and for this discussion, refer to Appendix A.

Owing to the wealth of knowledge amassed over the past three decades on PEDOT, high performance formations of chemically oxidized PEDOT:PSS are now commerically accessible. In the laboratory, PEDOT may also be readily synthesized by electropolymerization of 3,4-ethylenedioxythiophene (EDOT) in the presence of PSS (serving as the accompanying counter-ion) as in Eq. (1.1), giving:

$$\mathrm{PEDOT^{o}} + \mathrm{PSS^{-}M^{+}} \underset{\text{red}}{\overset{\text{ox}}{\rightleftharpoons}} \mathrm{PEDOT^{+}{:}PSS^{-}} + \mathrm{e^{-}} + \mathrm{M^{+}} \tag{1.2}$$

That is, the sulfonic acid moiety of PSS, which is a strong organic acid (pKa $\sim$ -2.1) [28, 29] and normally dissociated (i.e. anionic) in aqueous solution, becomes electrostatically complexed with cationic oxidized PEDOT. Due to the bonding structure of (bi)polaronic PEDOT shown in Fig. 1.2 (i.e. quinoid, with positive charge coupled to the conformation of three monomer units), maximum doping is ca. 33 % and $\mathrm{PSS^{-}}$ is in excess in the polyelectrolyte complex. Accordingly, the water solubility of PEDOT in this complex is significantly enhanced, enabling the aforementioned solution processabilty [30].

While highly crystalline PEDOT may be prepared via chemical vapor deposition techniques [31], PEDOT:PSS in solution exhibits phase segregation, with lamellar sheets of shorter PEDOT chains forming a semi-crystalline core surrounded by an extended, amorphous PSS-rich shell. The microstructure therefore forms droplets of micro-gels, becoming suspended in water as a colloid and can be condensed out into thin-films as depicted in Fig. 1.3. The interaction of PEDOT and PSS is highly sensitive to changes of ionicity in the solvent medium [32], and the resulting structure changes (e.g. coil to expanded-coil

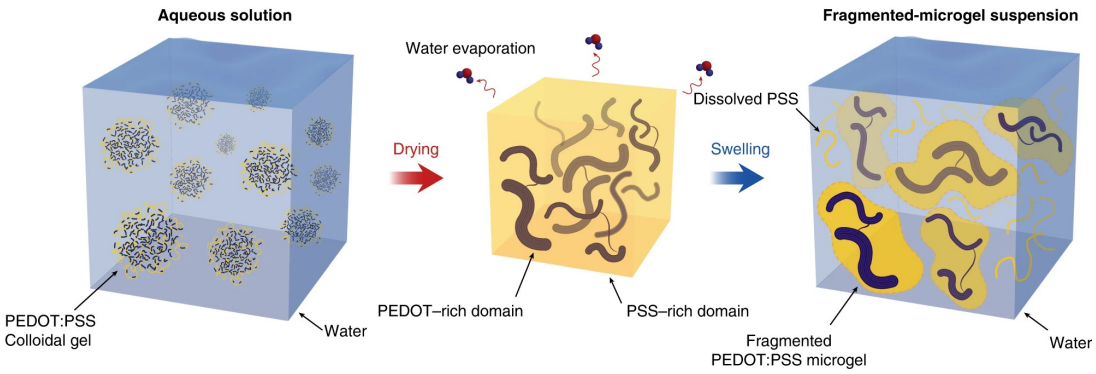

Figure 1.3: Schematic of PEDOT:PSS micro-gel structure and morphology changes upon dehydration and rehydration. Adapted with permission from [39] under a Creative Commons Attribution 4.0 International License (CC BY 4.0).

conformation of PEDOT) and phase reorganization decreases the barrier for hopping of carriers between PEDOT-rich phases [27, 33–35] and forms the physical rationale for conductivity optimization by the addition of high boiling point co-solvents and surfactants as "secondary dopants" [27] or re-crystallization [36, 37] (see also Appendix A). For the interested reader, a recent review provides more comprehensive insights into the structure-property relationships for electronic transport in PEDOT [38].

A confluence of gel structure and "dopant" charges as counter-ions (Eq. (1.1)) affords PEDOT:PSS with exceptional ionic-to-electronic coupling [40–42]. That is, the semiconductivity of PEDOT is strongly dependent on the species and activity of cations in the vicinity of an oxidized monomer unit [43, 44]; for instance, increasing cation activity shifts the equilibrium of Eq. (1.2) rightward and depletes the carrier concentration[2]. At the same time, the change in oxidation state of PEDOT during "de-doping" alters the phonon-electron coupling, producing a shift in the (bi)polaron bands and manifests as a change in its absorption spectrum, shown in Fig. 1.4. Namely, polaronic states are removed and absorption shifts to the visible range corresponding to a HOMO-LUMO transition [21, 23]. This change is visually obvious as the PEDOT:PSS film changes colour from transparent with a blue tinge to an opaque deep-blue, and can be used to track the ionic diffusion front [45, 46].

1.2.2 Organic electrochemical transistors (OECTs)

Less than a decade following the polyacetylene discovery, White et al. described the electrochemical modulation of polypyrrole film conductivity between two (source and drain) electrodes by small ionic currents applied by a third (gate) electrode when immersed in

[2]In essence, PEDOT is reduced with the required electron being supplied by contacting electrodes.

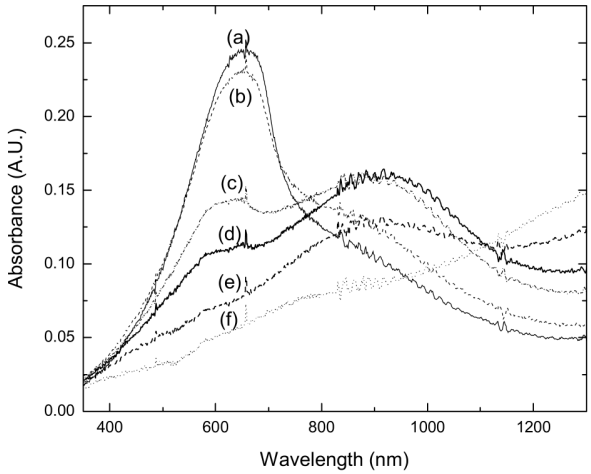

Figure 1.4: UV-Vis-NIR absorption spectrum of PEDOT:PSS during in-situ electrochemical de-doping in 0.1 M NaCl at (a) −0.7 V, (b) −0.4 V, (c) −0.2 V, (d) −0.1 V, (e) 0.1 V, (f) 0.5 V vs. Ag/AgCl. Reprinted with permission from [27]. Copyright 2004 Elsevier.

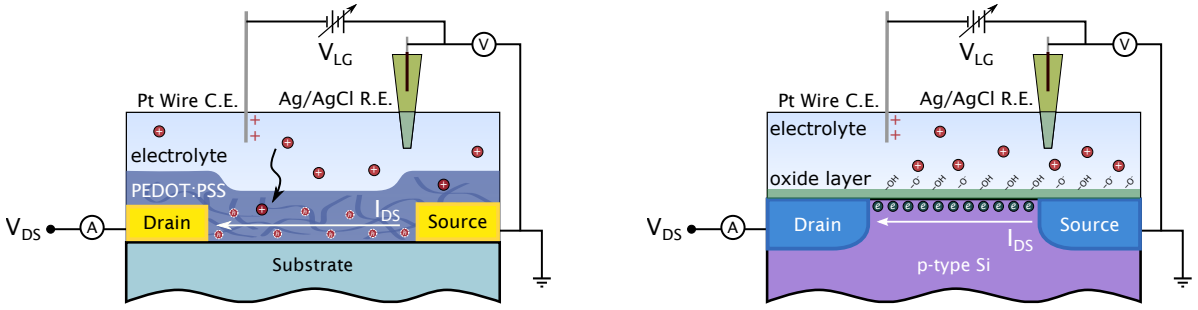

(a) OECT (b) ISFET

Figure 1.5: Comparison between OECT and ISFET device structures. In the OECT, device current is modulated by ions injected into the bulk of the conductive polymer, whereas the ISFET is controlled by the potential at the interface between semiconductor and electrolyte.

aqueous electrolyte [47]—the first report of what are now known as organic electrochemical transistors (OECTs) (Fig. 1.5a). Similarities with the operation of solid state transistors were immediately noted, with the device turning on at a threshold voltage approximately equal to the oxidation potential of the CP. Moreover, such devices exhibit current saturation at particular combinations of gate and source-drain potential, and mathematical treatments of charge transport similar to field-effect transistors can be used to describe the steady-state current flowing in an OECT [48, 49].

When the source-drain potential is small relative to the gate, a positive applied gate

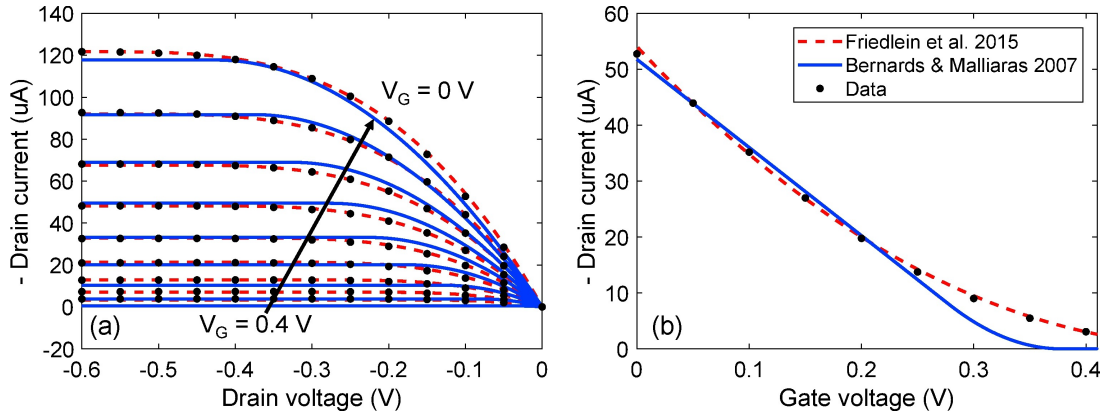

Figure 1.6: Output (a) and transfer (b) curves of a PEDOT:PSS OECT fit by two models. Reprinted with permission from [52] under a Creative Commons Attribution 4.0 International License (CC BY 4.0).

potential acts to deplete the channel and the OECT operates linearly [49]:

$$\frac{I_D}{V_D} = \frac{W \cdot d}{L} \mu_o C_g \left(V_p - V_G + \frac{V_D}{2} \right) \tag{1.3}$$

where W and L are the channel width and length, respectively; d is the thickness of the CP channel; μ_o is the mobility of charge carriers; C_g is the volumetric capacitance of the ionic circuit formed between the gate electrode and CP; V_p is the pinch-off, or threshold voltage equal to the potential required to deplete the CP of its initial doping charges, p_o ($V_p = ep_o \frac{WLd}{C_g}$); and V_D and V_G are the applied potentials at the drain and gate, respectively.

When the source-drain potential becomes large enough to reduce the CP, the OECT current saturates when the CP at the drain becomes depleted of charge carriers (i.e., pinch-off), giving a quadratic dependence on V_G [49]:

$$\frac{I_D}{V_D} = \frac{W \cdot d}{L} \mu_o C_g \left(V_p - \frac{V_G^2}{2V_D} \right) \tag{1.4}$$

and the saturation potential is $V_{D,\text{sat}} = V_G - V_p$. Fits to experimental data with these equations and one that includes non-ideal effects [50] is shown in Fig. 1.6. It is immediately obvious that Eqs. (1.3) and (1.4) are analogous to the field-effect transistor equations [51], with the geometric dependence of C_g being volumetric as opposed to areal. This reflects the fact that applied gate potentials must drop across the electric double layer (EDL) surrounding each CP chain because of permeability to ions in electrolytes [41].

This volumetric gating highlights the key difference in OECTs versus planar devices based on organic thin-films or inorganic semiconductors (e.g., Si) used for sensing in aque-

ous media, such as the ion-sensitive field-effect transistor (ISFET) depicted in Fig. 1.5b. That is, the figure-of-merit for the amplification of a surface potential change upon detection of environmental charge—transconductance—is enhanced by adding a third dimension [53] (i.e., $g_m = \frac{\partial I_D}{\partial V_G} \propto \mu C_{\text{vol}}$). At the same time, mass transport in the ionic circuit of the gate-channel creates a trade-off in the response time (i.e., ionic transit time, $\tau_i = R_{\text{sol}} C_{\text{vol}} \propto d\sqrt{WL}$) [54, 55] of OECTs versus the planar alternatives. However, by tuning the operating point [56, 57], channel geometry [58–60], swelling behaviour [61], or ionic mobility with ionic liquids [62] or hygroscopic polysaccharides [63] as secondary dopants, high amplification and sufficient frequency response for the detection of cellular events (ca. 0.1 to 1 kHz) [55, 56, 59, 60, 64–67] or fast scan voltammetry [68] can be realized.

Though the Bernards model [49] takes the simplifying assumptions that both gate capacitance and carrier mobility are constant and which are invalid in certain regimes of operation with large carrier densities[3] [50, 52, 69], it nevertheless remains highly useful for understanding the basic function of OECTs and extracting device parameters. For instance, the product of μ_o and C_g in Eqs. (1.3) and (1.4) (i.e., geometry and bias normalized g_m) is now used as a figure-of-merit for OECTs employed as ionic amplifiers [70].

1.2.3 OECTs as biosensors

In the development of transistors as biosensors that operate in electrolytic media, the location of the specific functionality (R^*) that binds to the analyte can be used to classify approaches into four categories, shown in Fig. 1.7. For example, for traditional ISFETs employing an amphoteric oxide membrane, R^* is decorated on the surface of the transducer such that the additional potential evolving from the change in surface charge density modulates the carrier density in the semiconductor [71, 72]. However, when the channel is actively being gated through the electrolyte by V_G (i.e., not floating) without a reference electrode, a potential evolving at the gate can produce a similar signal, albeit inverted [73]. This is because the output of the transistor as a biosensor is determined by the entire electrochemical cell[4].

On the other hand, this fact can be utilized to separate the location of detection and amplification, allowing for disparate optimization strategies. This is the typical approach taken by sensing studies using so-called electrolyte-gated FETs, extended-gate FETs, and OECTs as well. In this case, R^* need not remain bound to the surface as any binding

[3] Similar to the application of FET equations to nanostructured semiconductors, the ideal forms cannot account for non-monotonic transconductance because of mobility reduction due to scattering, for instance.

[4] Actually, a potential developed at any point along the gating stack will serve to provide a signal; for example, by placing an ion-selective membrane between two electrolytes [74].

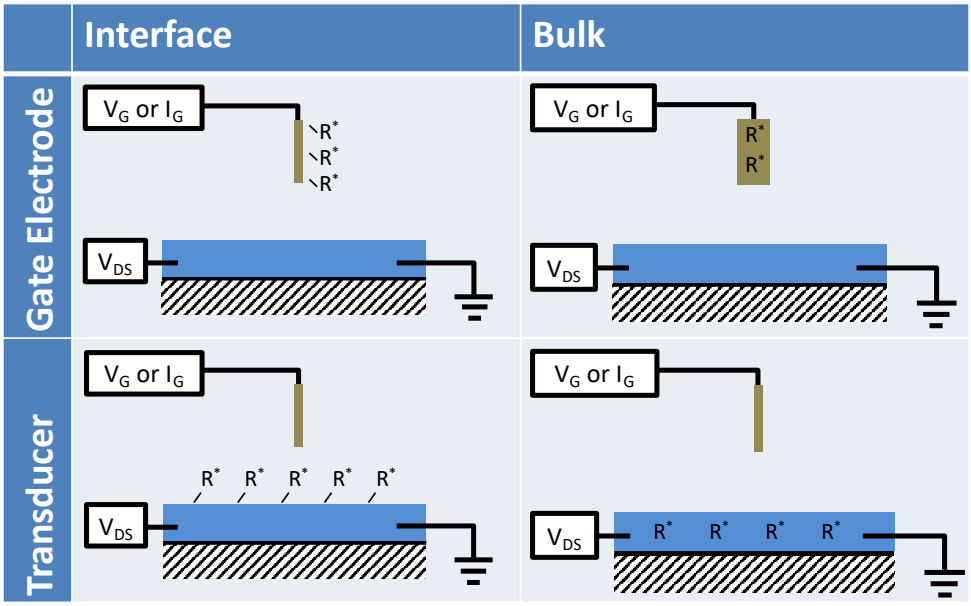

Figure 1.7: Optimization schemes for specificity in transistors operated as biosensors in electrolytes. Four classifications are distinguished based on the location of a specific binding site, R^*, for targeted analyte molecules.

event that affects the impedance of the ionic circuit connecting gate to transducer can be leveraged to produce a sensing signal. Accordingly, the ratio of gate capacitance to channel capacitance can be minimized to ensure that gating charges produce the largest modulation of carrier density in the transistor [75–78]. Moreover, Faradaic (i.e., redox) interactions that transfer charge into the electrolyte can be exploited to produce even greater signals[5] [79, 80].

Therefore, a majority of OECT biosensor studies investigate the functionalization of the gating electrode [81]. Though we do not attempt to be exhaustive here, we will note a few interesting studies which use PEDOT:PSS for both the gate and OECT channel. The simplest include those devices made by spin-coating a commercial PEDOT:PSS solution, with electrodes defined by a physical mask [82–84]. Here, the intrinsic ability of PEDOT to oxidize small biomolecules such as ascorbic acid [82], dopamine [83], uric acid [83], and adrenaline [84] produces additional Faradaic currents that can be localized on either the gate or channel depending on the operating point (i.e., V_G). It was noted that, regardless of where oxidation occurred, the OECT current decreases with addition of reducing agent which allowed for the optimization of device operation and a selective response based on the redox potential of the biomolecule [83].

Besides spin-coating, the use of PEDOT at the gate allows for facile fabrication of functionalized interfaces by electro-polymerization following Eq. (1.2). For example, pH

[5]That is, the difference between using a polarizable and non-polarizable electrode as the gate.

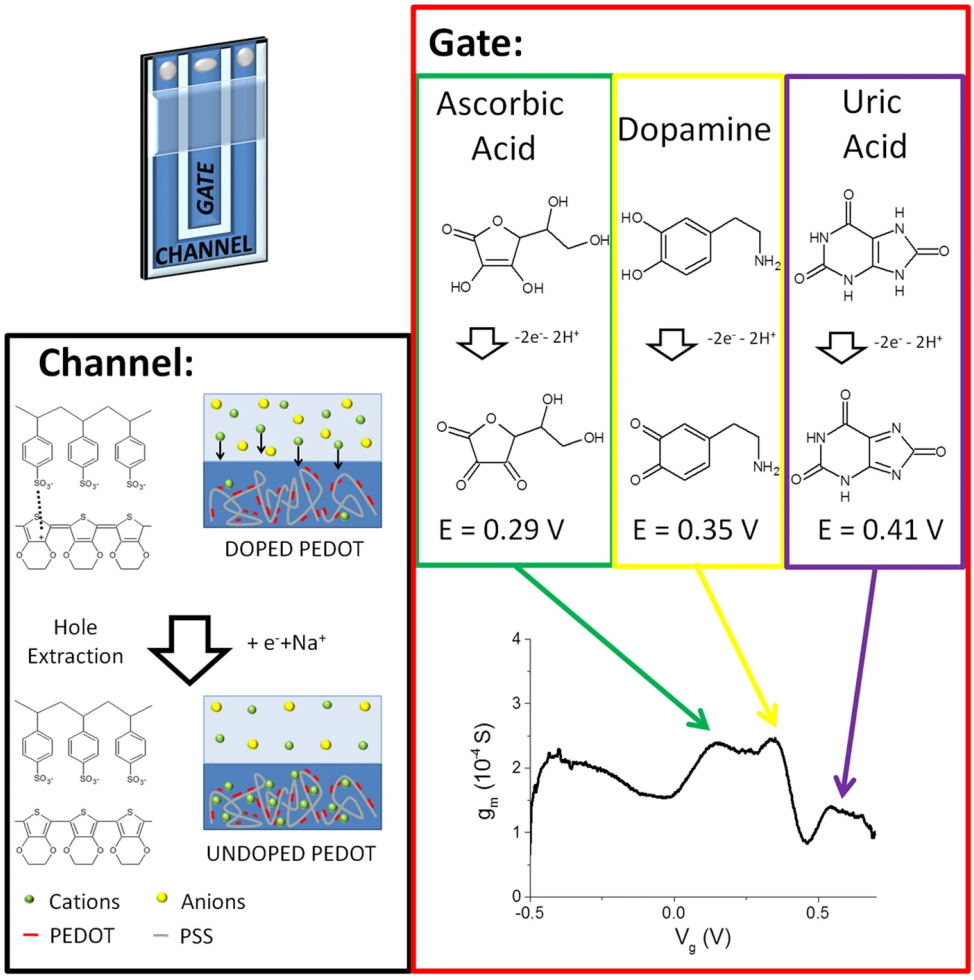

Figure 1.8: Selective sensing of ascorbic acid, dopamine, and uric acid based on oxidation potentials in an all-PEDOT:PSS OECT. The sensing change in OECT output due to the injected current from the PEDOT:PSS gate can be readily distinguished in the transconductance curve. Reprinted with permission from [83] under a Creative Commons Attribution 4.0 International License (CC BY 4.0).

sensors with super-Nernstian response[6] were prepared by EDOT polymerization with pH indicator dyes as counter-ions [85]. This approach also makes it simple to use novel conjugated monomers grafted with functional groups that may not be produced in sufficient yield for bulk processing [86]. For instance, by replacing the ethylenedioxy group in EDOT with longer oligmers of ethylene oxide, ion-selective crown-ethers could be tethered directly to the aromatic thiophene backbone for Na^+ and K^+ sensing [87]. In another study, biomimetic interfaces consisting of randomly co-polymerized EDOT monomers grafted with either hydroquinone or phosphorylcholine gave electrode surfaces with resistance to non-specific binding and redox-controllable immobilization of peptides (and cells) [88].

[6]That is, a surface potential change greater than ca. 60 mV per pH unit, corresponding to factors in the Nernst equation for a monovalent ion (H^+).

Perhaps owing to these benefits, studies that investigate the inclusion of R^* directly into the OECT channel are few, although mixed thin-films of PEDOTs grafted with alkylsulfonic acids have been studied as a means to tune the electronic structure by self-doping and control the OECT threshold voltage [89] or absorption spectrum (i.e. colour) [90]. For this approach to work for biosensing, the optimization strategies noted earlier must be updated as, when R^* is located in the channel, large capacitances make it difficult for a change in charge density to shift the potential of the CP. In this case, R^* should be designed to enhance charge transfer with the CP corresponding to analyte interaction[7], while maintaining high carrier mobilities to maximize the output signal. Such devices would simplify the miniaturization of OECT biosensors, as a functionalized gate would not be required. Additionally, proper reference electrodes can then be used to provide thermodynamically defined potentials.

1.2.4 Forming hydrogels from PEDOT:PSS

At the same time, researchers in the field of PEDOT-based biosensors have noted that, in addition to electrical and electrochemical functions, advanced healthcare devices will require materials that perform a structural role, being more than simply flexible but also mechanically compliant for biocompatibility [91] and ease of processing [92]. To endow PEDOT devices with structural function, a number of approaches have been reported; for instance, by printing PEDOT:PSS suspensions onto flexible substrates such as textiles [84], plastic [93], or paper [94], freeze-drying of mm-thick sheets [95], or by photo-curing of 3D-printed CP and acrylate resin blends to create bulky composites [96].

Such approaches remain constrained to the mechanical properties of a flexible substrate, or the stiffness of semi-crystalline PEDOT:PSS. While this may be considered a design function—for instance, to develop artificial scaffolding for culturing of osteocytes [95]—the tuning of stiffness by variation of composition is an important determinant for the biofunction and biocompatibility of the material. For example, compliant PEDOT:PSS hydrogels formed by complexation with peptide-polyethylene glycols of various cross-linked structures supported the culture and differentiation of mesenchymal stem cells into softer myocardiocytes embedded within [97].

In this regard, achieving structure by way of a hydrogel is appealing, since a high degree of hydration is simultaneously beneficial for ionic transport and compliance matching with biological tissues [91]. As discussed in Section 1.2.1, the micro-gel structure arising due to the electrostatic interaction of cationic (PEDOT) and anionic (PSS) polyelectrolytes is highly sensitive to conditions that affect inter-chain interactions such as ionic strength [32].

[7]That is, the signal should be electrochemical as opposed to electrostatic in nature.

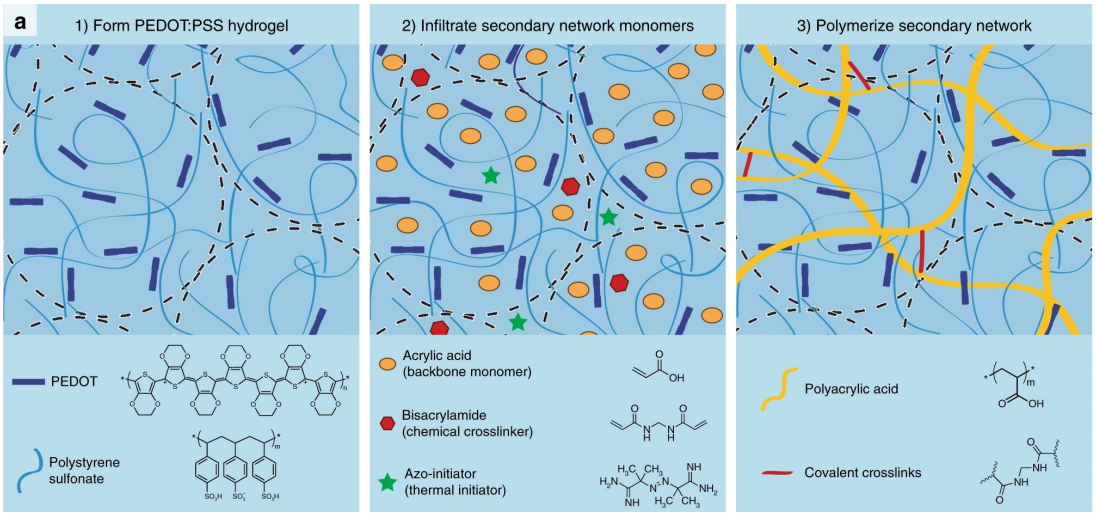

Figure 1.9: A process to form IPN hydrogels of poly(acrylic acid) and PEDOT:PSS. Aqueous solutions of PEDOT:PSS are firstly gelled by addition of an ionic liquid, followed by infiltration with monomers, cross-linker, and initiator. IPN is formed upon thermally initiated radical polymerization. Adapted with permission from [100] under a Creative Commons Attribution 4.0 International License (CC BY 4.0).

Accordingly, extended gelation can be readily induced by removing excess PSS with H_2SO_4 washing [98], solvent-assisted annealing [39], mixing with peptides [97], or the addition of surfactants at room temperature [99], for example.

Moreover, it has been shown that the elastic properties of PEDOT:PSS hydrogels can be tuned while keeping sufficient electrical conductivity by polymerizing acrylamide or acrylic acid monomers impregnated into pre-formed CP hydrogels [99, 100], forming so-called interpenetrating or double-network (IPN or DN) polymers. Electrical conductivity of these modern hydrogels (cf. 10^{-1} S/cm) is improved by two orders of magnitude over older reports taking the inverse approach—where EDOT monomers are polymerized inside poly(acrylamide)-based networks [101, 102]. This has been attributed to improved CP inter-chain connectivity because PEDOT and PSS complexes are prioritized in the pre-formation of CP hydrogel before polymerization of the IPN as depicted in Fig. 1.9.

This modern embodiment of conductive, IPN composite hydrogels is advantageous, as it allows commercially available CP formulations to be used. In fact, an even simpler approach of directly blending PEDOT:PSS with ultra-high molecular weight poly(acrylamide) solutions produced hydrogels with surprisingly high water swollen electrical conductivities of 17 S/cm and failure strain of 110 % at a composite loading of 64 wt % filler [103], which was attributed to enrichment of CP phase at the hydrogel surface because of partial poly(acrylamide) dissolution in water. Importantly, the use of a second network extends the composition space, enabling designs incorporating polymers that give, for instance,

self-healing capabilities [104] or swelling behaviour responsive to the binding of diols on phenylboronic acid moieties [105]. It is this extension of the design space that we will target in the present work.

To get a sense of how our experimental results will compare to the reported literature, a comparison of PEDOT-based hydrogels discussed herein is provided in Table 1.1. As the application of CPs is fundamentally a multi-disciplinary endeavour, the experimental goals, methodologies, and analyses are widely varied. We highlight two important results:

1. Ref. 39 reports the highest conductivities of PEDOT hydrogels at ca. 40 and 20 S/cm while swollen in water and phosphate buffered saline (PBS), respectively. However, this approach does not functionalize the CP.

2. Ref. 99 provided the first report of a PEDOT:PSS hydrogel used as an OECT channel in cetyltrimethylammonium bromide solution, albeit in a freeze-dried state and coated with chitosan. OECT characterization was not expanded upon.

1.3 Outline of the thesis

Having now reviewed the literature, we come to the realization that studies directly applying thick CP hydrogels as OECT channels are lacking. This is perhaps the outcome of two factors: first, limited interest in biosensor strategies that dispense with convenient gate functionalization; and second, poor conductivity or bonding of composite hydrogels not directly electro-polymerized on electrodes, thus making reliable device fabrication difficult.

Accordingly, in this thesis we first endeavour to fabricate and accurately characterize OECTs using CP hydrogels based on PEDOT:PSS in a composite with poly(acrylamide), focusing on their electrical and electrochemical characteristics. This is done to elucidate the best operating conditions for biosensing application of this material. The work for this part is presented in Chapter 2.

Next, the biosensing application of our CP hydrogel towards glucose is investigated. Here, selectivity for the saccharide molecule is designed into the hydrogel by the inclusion of acrylamide monomers bearing phenylboronic acid. The work for this part is presented in Chapter 3.

In Chapter 4, a novel reversible resistance switching phenomenon which was observed in a subset of fabricated devices is studied. This effect is likely caused by the coupling of electromechanical behaviour of the IPN and electronic structure of PEDOT.

Finally, Chapter 5 will summarize the experimental results achieved in the course of this thesis and offer some insight into the continuation of the work.

Table 1.1: Comparison of selected PEDOT-based hydrogels

Composition[a]	% CP	σ (S/cm)	Mechanical Property[b]	Gelation Method[c]	Ref.
PEDOT:PSS: EMIM BF_4	100 %	1.2×10^{-2}	G': $\leq 10^2$ Pa	ionic liquid	[32]
PEDOT:PSS	100 %	$\leq$8.8	G': 10^2 kPa	H_2SO_4 wash	[98]
PEDOT:PSS	100 %	$\sim$20 (PBS) $\sim$40 (H_2O)	E: $\sim$2 MPa	anneal w/ DMSO	[39]
PEDOT:PSS: peptide-PEG	1 %	1.5×10^{-2}	G': 3–10 kPa	electrostatic cross-link	[97]
PEDOT:PSS (:PAAm)	100 %	10^{-1}	E: $\sim$1 (–10^2) kPa	DBSA micelles	[99]
PAAm:PEDOT-PSS	42.7 %	2.2×10^{-3}	σ_f: $\sim$1 MPa	DN (EDOT)	[101]
PAMPS-PAAm: PEDOT	N/A	1.4–1.6×10^{-3}	E: 330–550 kPa	DN (EDOT)	[102]
PEDOT:PSS: P(NAGA-*co*-AMPS)	$\leq$10 vol %	0.2–2.2×10^{-2}	E: 30–110 kPa	monomer mixture	[104]
PEDOT:PSS: PAAc or PAAm	1.1 wt %	1.2–2.3×10^{-3}	E: 8–374 kPa	DN (AAc/AAm)	[100]
PEDOT:PSS: PAAm	37 wt %	17	E: <10 MPa	polymer mixture	[103]

[a] EMIM BF_4: 1-ethyl-3-methylimidazolium tetrafluoroborate, PEG: polyethylene glycol, PAAm: poly(acrylamide), PAMPS: poly(2-acrylamido-2-methylpropanesulfonic acid), PNAGA: poly(N-acryloyl glycinamide), PAAc: poly(acrylic acid)

[b] G': storage modulus, E: Young's modulus, σ_f: fracture strength

[c] DMSO: dimethyl sulfoxide, DBSA: 4-dodecylbenzenesulfonic acid, DN: double-network (infiltrating monomer)

Chapter 2

Fundamental properties of PEDOT:PSS hydrogels

Among the many methods to form electrically conductive hydrogels with PEDOT described in the literature, we deemed the composite approach to be the most suitable for the development of biosensing materials with structural functions. This is because the compositing material may be carefully engineered to tailor its electrochemical and mechanical properties. However, in the state-of-the-art, this approach has not yet produced such CP hydrogels with sufficient conductivity to be employed as OECTs.

Therefore, we sought to revisit the problem by opening up the composition space of conductive IPN/DN hydrogels and investigate the combination of PEDOT:PSS and crosslinked poly(acrylamides). A simple method of dispersing acrylamide monomers into stock PEDOT:PSS solutions produced remarkably good results. In the following chapter, the discovery process is documented briefly, with a focus on the electrical, electrochemical, and OECT device characteristics of the best performing compositions. A schematic overview of the DN hydrogel OECT is shown in Fig. 2.1.

2.1 Composition and structure

2.1.1 Design of second network polymer

DN hydrogels were prepared by combining off-the-shelf formulations of PEDOT:PSS (Orgacon™ ICP 1050, Sigma-Aldrich) and pre-mixed cocktails of acrylamide monomers and an azo radical initiator. The cocktail contained 11 wt % precursors in de-ionized (DI) water (18 MΩ cm, Komatsu Electronics UL-Pure) and was mixed in a 1:10 ratio with PEDOT:PSS (ca. 1.1 wt % solids) to give a dry composite fraction of ca. 0.5. A flowchart

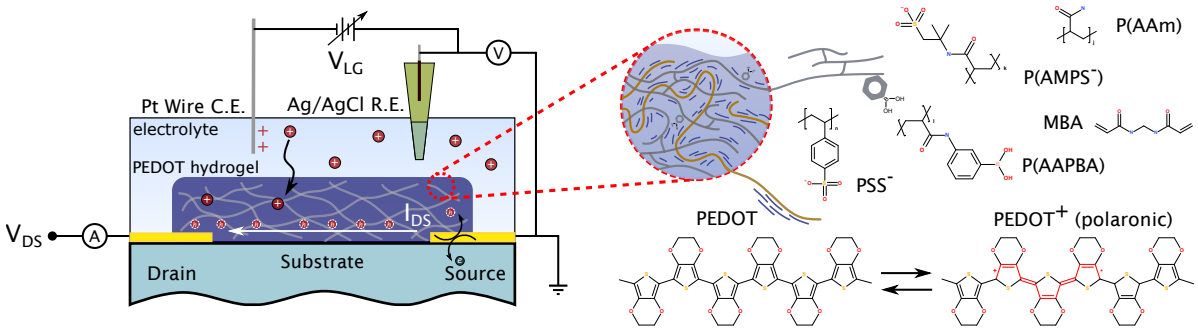

Figure 2.1: Schematic diagram of double-network PEDOT hydrogel containing PBA used as channel of an organic electrochemical transistor (left). Molecular structure of polymers composing the hydrogel (right). P(AAm) is poly(acrylamide), P(AMPS$^-$) is poly(2-acrylamido-2-methylpropanesulfonic acid), P(AAPBA) is poly(3-(acrylamido)phenylboronic acid) together randomly cross-linked in a network by MBA (N-N'-methylenebisacrylamide).

of the process to prepare the precursor mixture, with the concentration of stock solutions used for each constituent, is provided in Fig. 2.2.

In the second network, acrylamide (AAm, 99.0 + %) was used as the backbone, co-polymerized with 2-acrylamido-2-methylpropanesulfonic acid (AMPS, 97.0 + %), and cross-linked by N-N′-methylenebisacrylamide (MBA, 97.0 + %). The use of AMPS was previously suggested to act as a dopant of PEDOT (due to the sulfonic acid) [102], or improve the processability of the pre-mixture due to its hydrophilicity [104]. Here, we have selected AMPS as a co-polymer because we hypothesize that its acidic, polyanionic nature may displace some PSS—similar to sulfuric acid treatments [26, 36, 106]—and improve the intermixing of acrylamide and PEDOT-rich phases.

To investigate the biosensing application of this material described in Chapter 3, 3--(acrylamido)phenylboronic acid (AAPBA, 97.0 + %), an acrylamide monomer bearing a phenylboronic acid (PBA) moiety, was additionally co-polymerized to provide a specific site for diol binding. Its proportion displaces a corresponding amount of AMPS to keep the AAm:functional monomer ratio constant. Because of its limited solubility in acidic solutions (i.e., boronic acid is very weakly dissociating), stock solutions containing acid groups and PEDOT:PSS needed to be neutralized.

The process of raising the pH of stock PEDOT:PSS solutions has been studied in the design of solar panels that use PEDOT as a transparent interconnect, due to the deleterious effects of high acidity on other metallic structures in the panel design [107, 108]. Here, it is found that the use of organic bases, such as guanidine or imidazole, as opposed to strong inorganic bases, such as NaOH, retain the electrical properties of PEDOT.

Thus, we used imidazole (98.0 + %), prepared as a concentrated 3.7 M stock solution,

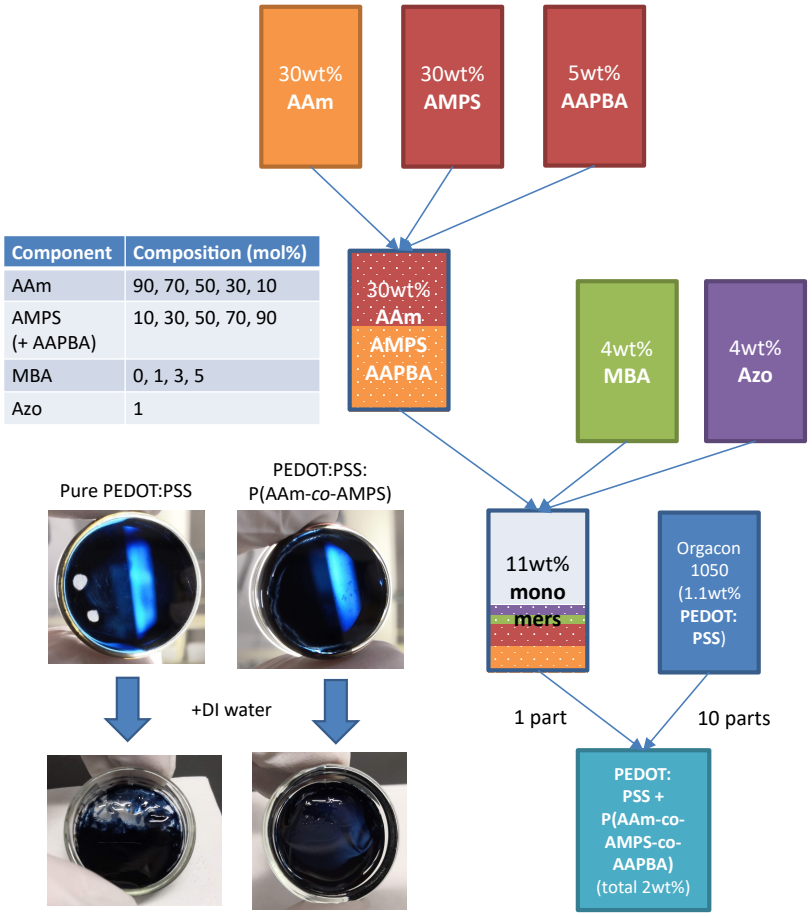

Figure 2.2: Overview of processing of polymer precursors and the monomer composition space. Photographs demonstrating the stabilization of PEDOT:PSS hydrogel structure by the formation of IPN during re-swelling with DI water.

to displace a portion of the required mass of aqueous solvent in acidic pre-mixtures[1]. The total addition equated a slight stoichiometric excess to all acidic polymer units (assuming a 1:2 molar ratio of PEDOT to PSS). Finally, we note that all reagents in the cocktail, with the exception of AAPBA (Tokyo Chemical Industry), were sourced from Fujifilm Wako Pure Chem. Corp. and all were used as-received.

Choice of azo initiator

In the precursor mixture, the effect of ionic strength significantly informs the design process because of the colloidal nature of PEDOT:PSS [32]. Besides the monomers, the choice of water-soluble azo initiator is also an important factor to mitigate undesirable early gelation or phase separation (e.g., due to ionicity or activation temperature). To that end,

[1]Guanidine is typically available as the hydrochloride, which unduly raises the ionic strength of the premixture and causes phase separation of PEDOT. Imidazole is also used in commercial solutions of neutralized PEDOT:PSS.

we investigated the following, sourced from Wako Pure Chem. Corp.:

- 2,2'-azobis(2-methylpropionamidine) dihydrochloride (V-50, 97.0 + %; at 70 °C)
- 2,2'-azobis[2-methyl-N-(2-hydroxyethyl)propionamide] (VA-86, 98.0 + %; at 90 °C)
- 2,2'-azobis[N-(2-carboxyethyl)-2-methylpropionamidine] n-hydrate (VA-57, 95.0 + % anhydrous; at 60 °C)

V-50, though it is the most commonly used out of these azo initiators, was deemed unsuitable because of the presence of Cl^- causing early gelation. This created significant structural inhomogeneity due to the inclusion of large gelled aggregates. VA-86, while being non-ionic, activates at high temperatures which cause solvent loss and concomitant phase separation of acrylamides during polymerization. Finally, we found that VA-57, being a zwitterion [109] and activating at moderate temperatures, had a manageable effect on early gelation. Accordingly, all pre-mixtures were freshly prepared and dispensed within 10 to 15 min of monomer dispersion, which was assisted by vorticing in conical tubes.

Narrowing of the composition space

As shown in the table inset in Fig. 2.2, the composition space of the acrylamide gel network considered five molar ratios of AAm:AMPS (later, AMPS+AAPBA) and four compositions of MBA cross-linker, while the composition of azo initiator and PEDOT:PSS was kept constant at 1 mol % and 50 wt %, respectively. This gave the number of possible combinations as 40, so to simplify the investigation, we first investigated the ratio of monomers and MBA cross-linker in poly(AAm-*ran*-AMPS) in the absence of PEDOT:PSS.

For this, 1 mg (actual mass: 0.985 ± 0.062 mg) of gels were prepared in pre-weighted sample vials and mass swelling upon successive additions of DI water after removal of loose liquid was determined by taring (Fig. 2.3a). We observed that polymers with high AMPS content did not form cohesive gels, while those with high AAm content formed gels regardless of the amount of cross-linker used. Only the 70 AAm:30 AMPS composition exhibited a proportional trend with increasing cross-linker.

Subsequently, the same compositions were prepared, but now mixed with PEDOT:PSS. Aliquots of 200 µL gave 3.34 ± 0.52 mg of dried gels. Larger portions were also prepared in polystyrene culture dishes for observation. After the inclusion of PEDOT:PSS, compositions that previously did not form gels could be stabilized owing to the electrostatic interaction with PEDOT:PSS. However, it was apparent that, at high AMPS content (>50 %), the change in surface tension caused dried gel films to be cracked and voided. Moreover, gels with 90 % AAm fractured during re-swelling in DI water.

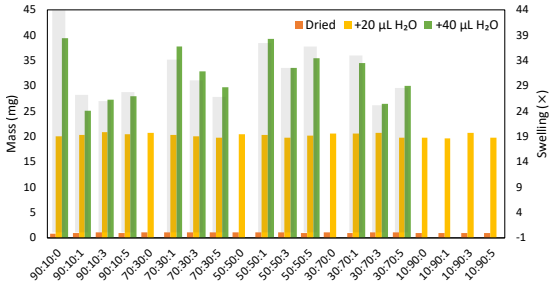

(a) without PEDOT

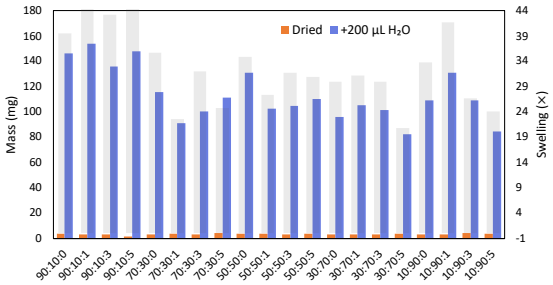

(b) with PEDOT

Figure 2.3: Mass swelling of hydrogels vs. AAm:AMPS:MBA ratios with additions of DI water. Loose water was decanted after allowing 2 h for uptake. Grey bars correspond to the ratio of swollen to dry mass (right axes).

To move quickly into the next phase of the study, the 70 AAm:30 AMPS composition with 3 mol % MBA was deemed to be the most robust in terms of consistent re-swelling of DN hydrogels in DI water. To demonstrate the effect of including PBA in the DN, 6 mol % of AMPS was replaced with AAPBA. Therefore, in the following discussion, material compositions will be distinguished by the PBA content (e.g. PBA-0 or PBA-6).

2.1.2 Fabrication of hydrogel devices

DN hydrogels for the fabrication of devices were prepared from 1 mL aliquots of the precursor mixture dispensed into 30 mm diameter, flat-bottomed glass dishes cleaned by sonication in acetone, methanol, and DI water for 5 min each. Free radical polymerization was thermally initiated by heating the mixture in a N_2-filled reactor following two purges in rough vacuum and proceeded at 60 °C for 6 h. This produced large films of desiccated PEDOT:PSS:poly(AAm-*ran*-AMPS) or poly(AAm-*ran*-AMPS-*ran*-AAPBA), which were subsequently re-swelled in 1 × phosphate buffered saline solution (PBS, pH 7.4, Gibco). Mechanical strength depended on the ionic strength of the re-swelling medium, with PBS giving DN hydrogel films that readily detached from their dishes and were free-standing. Accordingly, various device geometries could be shaped by manually cutting the swelled films. DN hydrogels were then stored in fresh PBS at 4 °C overnight or until needed.

Electrode structures for electrochemical and electrical transport characterization were prepared from Cr/Au deposited on glass substrates (Kyodo International Inc.) and cleaned similarly to the reaction dishes. For a description of lithographic techniques used to prepare electrodes, see also Appendix A. Optical micrographs of such devices are depicted in Fig. 2.4. In the dry state, ohmic contacts were achieved by simply de-swelling shaped hydrogels positioned on the electrode surfaces; however, improved contact reliability in electrolytes could be obtained by a simple thermo-mechanical annealing process, described

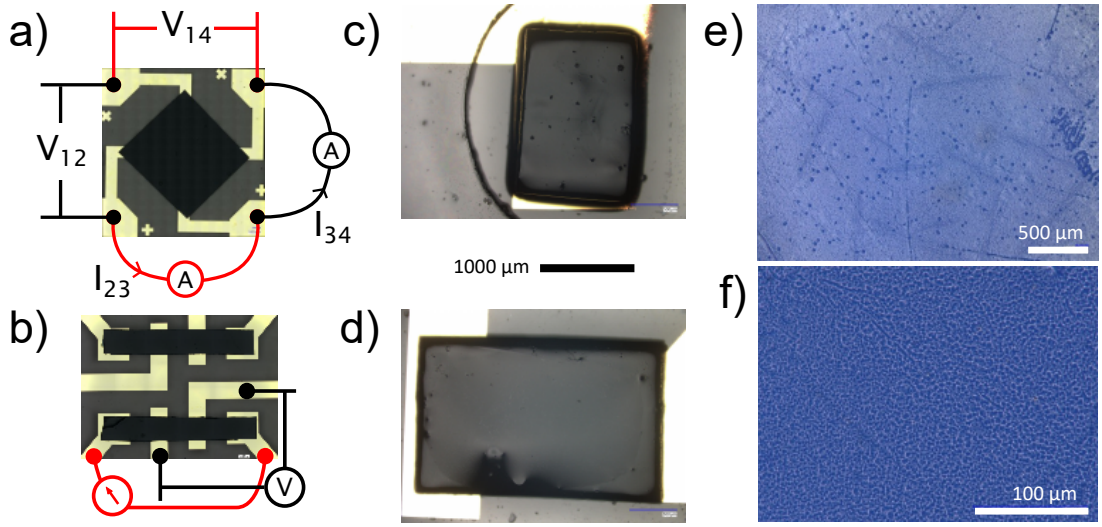

Figure 2.4: Optical micrographs of DN hydrogels serving as large-area films for van der Pauw (a) and monolithic channels for transmission line and four-point (b) measurements with electrical connections as indicated, and as electrochemical electrodes (c) and OECT channels (d). Surface features at 100 and 1000 × (e, f), with transmitted white light providing the colouration.

below. This ensured a low contact resistance (see discussion in Section 2.2.1), even with repeated re-swelling cycles or prolonged storage in solution.

First, a few drops of DI water were applied to rinse the devices and carefully wicked away to prevent re-crystallization of salt residues and to swell the hydrogels beyond their equilibrium in PBS. This rinsing was repeated 2 to 3 times. Alternatively, cut hydrogels were rinsed by immersion for 30 s in DI water prior to positioning on electrodes. Afterwards, flowing N_2 was used to partially de-swell the hydrogels, whereby a protective sheet of poly(dimethylsiloxane) (PDMS) could be overlaid on the devices and a weight applied without slipping. Typically, a pressure of ca. 100 to 150 kPa while heating at a hot-plate temperature of 90 to 95 °C for 30 min was sufficient to produce devices reliable for characterization. Anecdotally, we also note that passing a current of few mA following this step, as may be routine in the battery of characterization tests, appears to help the bond. This may be due to covalent binding of a monomer on to the Au surface.

2.1.3 Anisotropic structure

Morphology

DN hydrogels swollen in PBS were prepared for scanning electron microscopy (SEM) by flash-freezing under liquid N_2 and lyophilization overnight (9 Pa, Eyela EDS-2000). Lyophilized samples were subsequently cross-sectioned by cutting or ductile fracture and

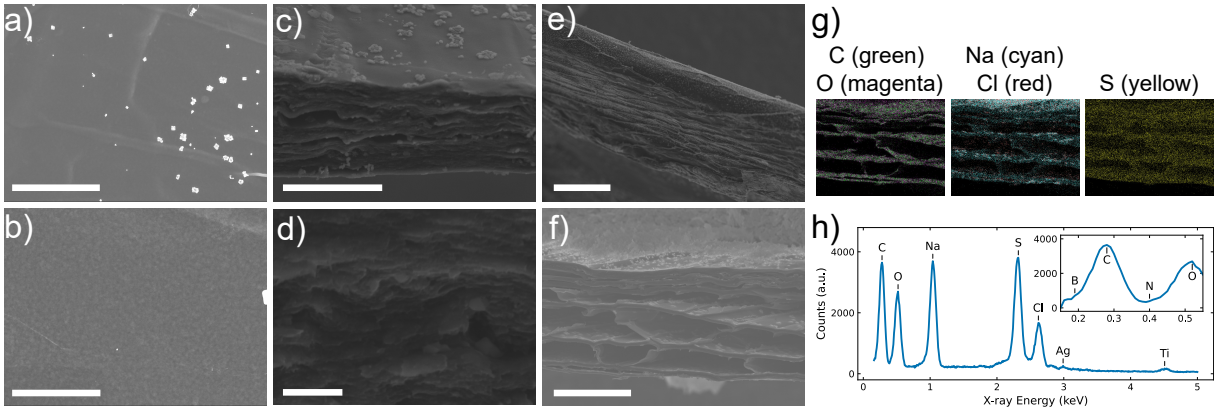

Figure 2.5: Scanning electron micrographs (a-f) of lyophilized PBA-6 hydrogel. Scale bars are 40, 10, 20, 2, 80 and 40 µm, respectively. Accelerating voltage of 10 kV was used for all except (b) which was taken at 5 kV to show surface morphology. Elemental mapping (g) and corresponding EDS spectrum (h) of the cross-section shown in (f).

mounted on Ti substrates using Ag paste. Figure 2.5 presents micrographs taken by either a Topcon SM-200 (Fig. 2.5c-e) or JEOL JSM-7001F (Fig. 2.5a,b,f) scanning electron microscope. The latter was also used to perform elemental mapping (50 passes at 10 kV) via energy dispersive x-ray spectroscopy (EDS) (Fig. 2.5g,h).

Outward surfaces of lyophilized hydrogels are generally flat, with some ridges and micro-scale roughness that becomes apparent at lower accelerating voltages (Fig. 2.5b). A lamellar structure is observed in cross-sections (Fig. 2.5c,e,f), with thicknesses ranging from 15 to 150 µm. This variability in cross-sectional thickness observed by SEM is likely due to handling during sample preparation that partially collapses the gel structure. Regardless, a hierarchical structure can be observed, with small platelets (Fig. 2.5d) condensing to form large planes that are inter-linked through the thickness direction (Fig. 2.5f).

Owing to the swelling medium of PBS, re-crystallized salt residues with diameters ca. 0.5 to 1 µm are observed on exposed surfaces, including those internal to the hydrogel. Elemental mapping via EDS (Fig. 2.5g) confirms the composition of these crystals[2] as NaCl, which is the majority component of PBS (ca. 150 mM). A signal from Na is also present throughout the bulk, on account of the anionic nature of poly(AAm-*ran*-AMPS) which includes cations to maintain electro-neutrality.

From the EDS spectrum (inset of Fig. 2.5h) it is apparent that signals from low atomic mass elements such as B or N, corresponding to PBA moieties or the acrylamide back-bone, respectively, are too low to be taken with confidence. However, strong peaks from C and O are observed and their spatial map correlates with the polymer bulk observed in the

[2]Note that diametrically opposed colours were chosen for the two-component maps such that overlapping regions give increased contrast.

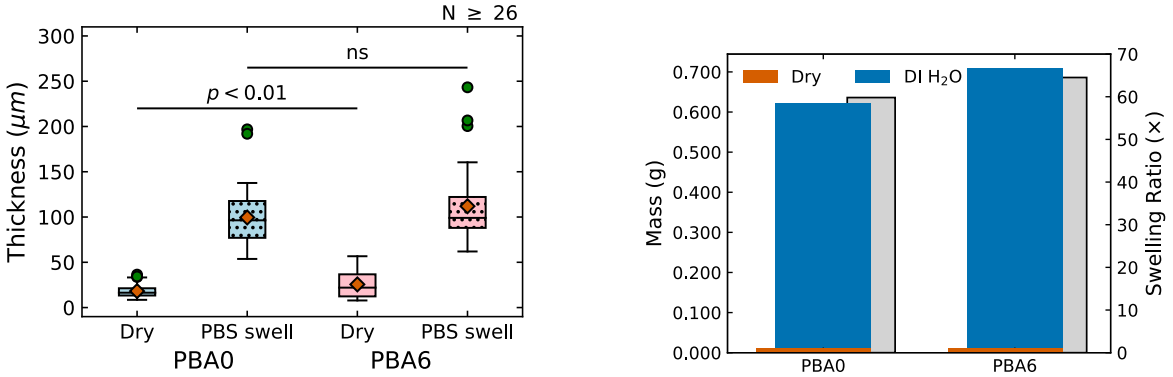

(a) (b)

Figure 2.6: Thickness (a) and mass swelling ratio (b) of PEDOT hydrogels with 0 and 6 mol % PBA in the dry state or swollen in PBS or DI water. Statistical significance in (a) is determined by unequal variances (Welch's) t-test.

secondary electron image. Moreover, a strong S peak produced a highly uniform map, suggesting that the second polymer network containing AMPS was well dispersed with PEDOT:PSS (cf. 0.3 and 1 S/mer, respectively). From the mapping of NaCl crystals, it may be deduced that any likely phase segregation occurs on a length scale below the observable limit of EDS (ca. 1 µm).

Reversible re-swelling

Optical microscopy (Keyence VHX-7000) of DN hydrogels in the dry state corroborated the SEM observations of micro-scale surface roughness (Fig. 2.4e,f). In addition to the hierarchical structure discussed previously, this highly porous microstructure endows DN hydrogels with rapid and efficient uptake of electrolytes during (re)swelling.

Thicknesses determined by optical confocal measurements are shown in Fig. 2.6a. When dry, DN hydrogels of both PBA-0 and PBA-6 compositions had average thicknesses of (18 ± 7) and (26 ± 15) µm, respectively. This increased by $\sim 5\times$ to (100 ± 33) and (112 ± 45) µm, respectively, when swollen in PBS. The inclusion of PBA appears to affect the thickness of hydrogels—increasing both the mean and variance of the sampled measurements—although this is not statistically significant in the swollen state. In contrast, the surface area changed by only ca. 10 % during swelling, characteristic of significant anisotropy in the underlying polymer structure.

Mass swelling of PBA-0 and PBA-6, shown in Fig. 2.6b, for samples that were slowly dessicated in refrigerated storage over the course of 30 days and finally re-swelled in DI water indicate that the DN hydrogel can absorb up to 98 wt % of water. In more applicable electrolyte media, the volume change represented by the ratios of dry and

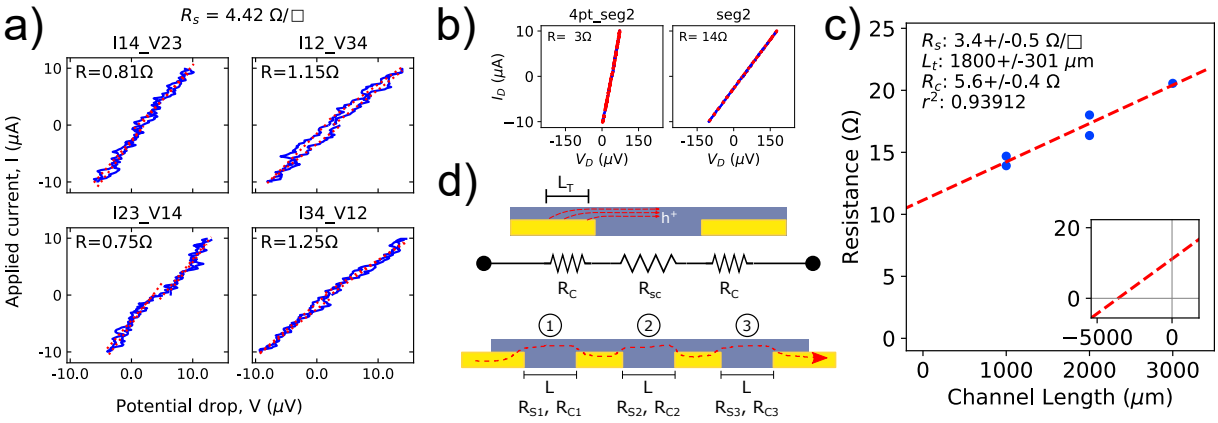

Figure 2.7: Current-voltage curves for conductive DN hydrogel (PBA-6) from a van der Pauw (a) and four-point measurement (b). Graphical method (c) for fitting to a transmission line model, schematized in (d). Red dashed lines are the linear regression lines used to fit each set of data to extract sheet resistance, R_S.

swelled thickness show that 70 to 80 vol % consists of liquid. This is a highly promising result for the application of these DN hydrogels as bioelectronic interfaces.

2.2 Electrical and electrochemical properties

2.2.1 Electrical conductivity

Methods

To determine the electrical conductivity, σ, of these DN hydrogels, van der Pauw, four-point, and transmission line measurements were used. This duplicity of methods was employed to confirm that measurements were not distorted by the effect of contact resistances. To minimize the possibility of deleterious effects arising from passing too much current (e.g. joule heating, electrochemical reaction), small supply current of 10 to 20 µA was used. This required instrumentation with µV resolution, as the dry hydrogels were highly conductive. For this, either a Keysight B1500A parameter analyzer or Solartron 1470 potentiostat was used. Afterwards, linear regression was used to extract resistances from each quadrant of the I-V curves measured in a cyclic sweep, with the average value reported as to limit the effect of DC offset voltages of the instrumentation and connections (e.g., thermovoltage).

In the dry state, sheet resistance (R_S) was extracted from van der Pauw measurements

by numerically solving for R_S in the transcendental equation [110]:

$$\begin{aligned} 1 &= e^{-\pi \frac{R_A}{R_S}} + e^{-\pi \frac{R_B}{R_S}} \\ R_A &= \frac{1}{2}\left(\frac{V_{12}}{I_{24}} + \frac{V_{34}}{I_{12}}\right) \\ R_B &= \frac{1}{2}\left(\frac{V_{14}}{I_{23}} + \frac{V_{23}}{I_{14}}\right) \end{aligned} \tag{2.1}$$

where the subscripts of V_{ij} and I_{kl} indicate the contact points for the supply of current and probing of potential, as depicted in Fig. 2.4a. A home-built switch box was used to facilitate the change over of connections, mitigating the effect of errors arising from replacing the alligator clips used to contact the planar electrodes.

These results were compared to four-point measurements of DN hydrogels cut from the same batch (shown in Fig. 2.4b), where the resistance is related geometrically to R_S:

$$R = \frac{1}{\sigma}\frac{L}{tW} = R_S\frac{L}{W} \tag{2.2}$$

where L, W, and t are the length, width, and thickness of the channel, respectively. The contact resistance, R_C, can be estimated by simply comparing the four-point and two-point resistances. Better yet, a simple transmission line model [69] can be applied to vary L by measuring the series resistance of adjacent junctions between probe electrodes (Fig. 2.7d):

$$R_T = \frac{R_S}{W}L + 2R_C = \frac{R_S}{W}(L + 2L_T) \tag{2.3}$$

where R_T is the total series resistance and L is the equivalent length, discounting portions overlapping with probe electrodes (which are equipotential) [111]. Thus, L is the multiple of channel length and assuming a constant aspect ratio allows extraction of R_S and R_C from the plot of R_T vs. L (i.e., slope and intercept). Furthermore, stating R_C in terms of R_S (i.e., $R_C = R_S\frac{L_T}{W}$) defines a metallurgical contact length, L_T, that describes the distance charge carriers travel in the conductive film before being collected by the electrode.

For resistance measurements of DN hydrogels in the swelled state, a reference/counter electrode pair (as described in the following Sections 2.2.2 and 2.3.1) connected in series with a 1 MΩ resistor was used to provide a reference potential of 0 V vs. Ag/AgCl in the electrolyte (1 × PBS). As opposed to a floating measurement, the use of a thermodynamic reference allows for reproducible results over time by setting the equilibrium carrier density in the channel. The series resistance prevented undesirable current fluctuations during changes of polarity in the measurement due to the inherently low input impedance of the DN hydrogel in an OECT configuration.

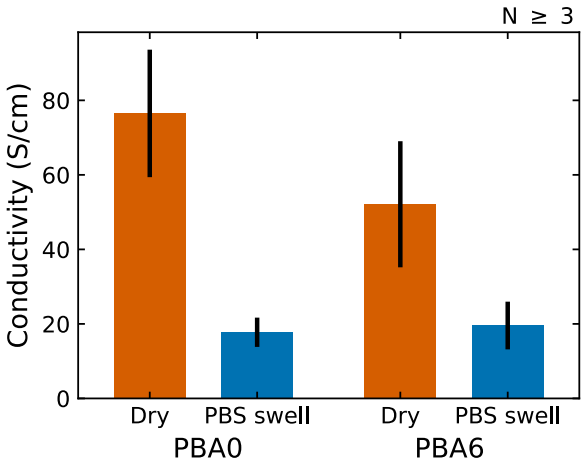

Figure 2.8: Electrical conductivity of DN hydrogels in dry and swollen states determined from correlated sheet resistance and thickness measurements. Error bars represent sample standard deviation.

High electrical conductivity

Accordingly, low R_S averaging 5.8 Ω/□ were determined for both PBA-0 and PBA-6 hydrogels. Considering the difference in film thicknesses, this corresponds to electrical conductivities, σ, of (76±17) and (52±17) S/cm in the dry state as shown in Fig. 2.8. These values are surprisingly high, considering that no enhancing additives [25] (e.g., ethylene glycol) were included in the composition, and suggest that inter-mixing of PEDOT:PSS and the second network during hydrogel fabrication had a synergistic effect.

When swollen in PBS, R_S remains approximately the same, with a drop in conductivity proportional to the increase in hydrogel thickness by swelling. Accordingly, σ is (18 ± 4) and (20 ± 6) S/cm for both tested DN hydrogel compositions when swollen in PBS. This is 2 to 3 orders of magnitude better than the PEDOT:PSS:PAAm composites compared in Table 1.1 and comparable to the state-of-the-art [39, 103], but with the capacity for functionalization via the second polymer network.

Contact resistance

At the same time, R_C from transmission line measurements was also determined to be ca. 5 to 6 Ω for both PBA-0 and PBA-6 when the hydrogel was appropriately bonded to the Au electrodes. These values were quantitatively similar to PEDOT:PSS thin-films spin-coated directly on to Au (see also Appendix A), indicating that the electrical connection made by simple de-swelling or thermo-mechanical annealing was good.

On the other hand, when DN hydrogels were operated in electrolyte media, some

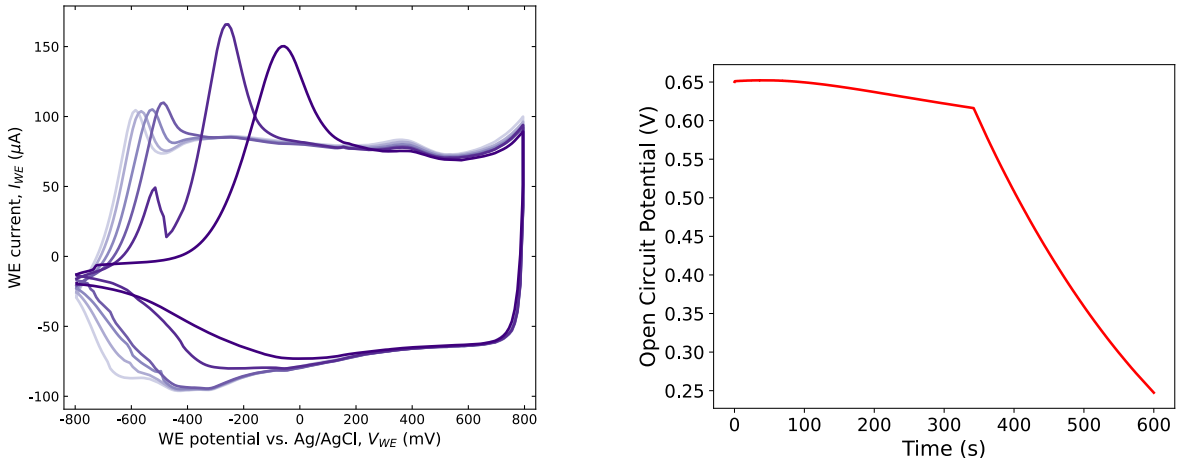

(a) (b)

Figure 2.9: Disconnection of a DN hydrogel during cyclic voltammetry (a) and open circuit potential (b) measurement. Shading of lines in (a) correspond to progression of cycles.

samples with insufficient annealing experienced gradual or sudden disconnection during characterization. Figure 2.9 shows two examples occurring during cyclic voltammetry (CV) and open circuit potential (OCP) measurements. During CV, oxidation peak potentials related to hole injection into PEDOT [41] begin to drift towards more positive potentials until a sudden break causes a large shift. During OCP measurement, the same gradual drift of V_{oc} was observed, with an acceleration at an intermediate time around 300 s. Note that the magnitude of V_{oc}, which is related to the reduction potential of PEDOT, is inverted due to the connection to the potentiostat for this measurement.

Voltammograms with the shape of the final cycle in Fig. 2.9a were also observed in CV measurements when the current collector did not fully encompass the hydrogel area. This suggests that the oxidation peak shift is related to the potential drop within the DN hydrogel, thus requiring additional overpotential to access the chemical state of PEDOT monomer units furthest away from the current collector. Moreover, broadening of the Gaussian peak is indicative of increasing disorder in CPs [112]. Accordingly, when properly referenced to a thermodynamically stable potential through the RE, this oxidation peak position can be used to evaluate the bond between Au and the DN hydrogel in electrolyte.

This peculiar behaviour of contacts in highly conductive hydrogels is likely due to the confluence of two factors. First, the inclusion of polyelectrolytes (e.g., PEDOT, PSS, PAMPS) imparts an electro-mechanical property due to the conformation change of these polymers with their local charge environment [61, 101, 113–116]. Second, comparable values of R_C and R_S (N.B., $R_S = R_{\text{channel}}$ when aspect ratio is 1) means that a significant portion of the applied potential drops across the contacts. This leads to the formation of

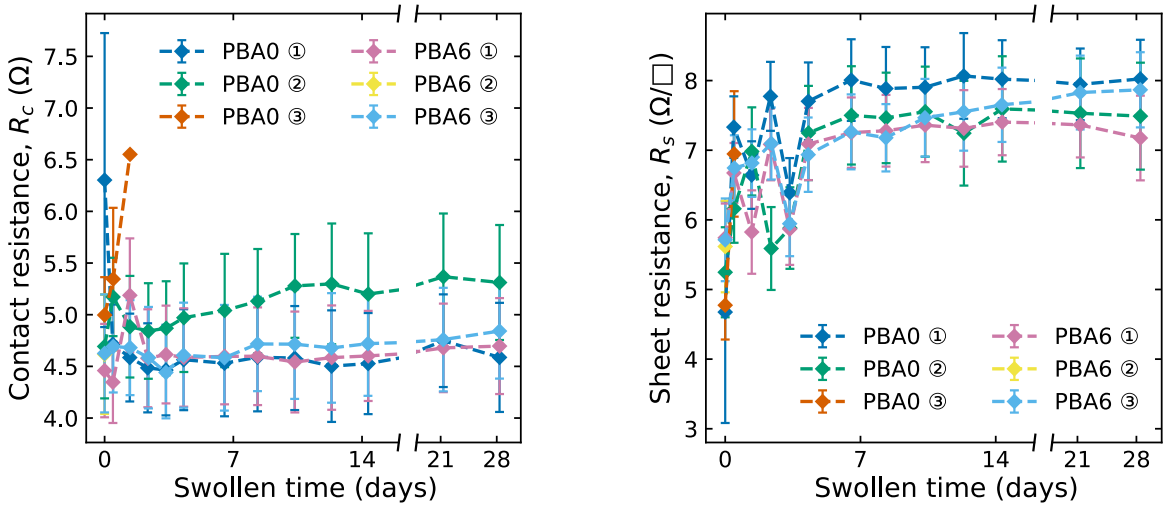

(a) (b)

Figure 2.10: Extracted contact (a) and sheet (b) resistances over time from transmission line measurements of DN hydrogels. Following initial dry characterization ($t = 0$), device substrates were maintained in a swollen state in 1 × PBS. Error bars represent the standard error in the linear regression used to extract parameters.

a space charge[3], thus inducing an actuation and weakening the connection.

A strategy to circumvent this problem by interpenetrating PEDOT:PSS hydrogels with a polyurethane adhesion layer has been proposed [117]. However, this method adds complexity due to the need for amine surface functionalization, in addition to hydrogel formation *in situ* on the substrate. For robust devices on flexible plastic substrates such as polyimide, this method is promising; however, for fundamental characterization on Au electrodes, we believe that simple thermo-mechanical annealing is sufficient.

Time stability

To that end, stability testing was performed on DN hydrogel channels bonded to Au by thermo-mechanical annealing as detailed previously. After taking four-point and transmission line measurements in the dry state ($t = 0$), hydrogels were re-swollen in 1 × PBS for 6 h and measured again while immersed in fresh PBS. Following re-characterization, device substrates were immediately replaced into fresh PBS and this process was repeated for a total duration of 4 weeks. At no point during testing were the hydrogels allowed to de-swell. Accordingly, the contact resistance data presented in Fig. 2.10a represent the stability of the bond formed by thermo-mechanical annealing against interfacial failure due to initial swelling or gradual ingress of water at the adhesive joint.

[3]This is implied by L_T being larger than the physical length of the current collector in Fig. 2.7c.

In a cohort of 6 devices (i.e., 3 per hydrogel composition), the yield after 1 d was 67 %. Full or partial delamination of failed bonds was quickly apparent after re-swelling and remaining successful bonds demonstrated remarkable stability thereafter. R_C remained approximately the same between dry and swelled states, whereas R_S increased slightly upon re-swelling. This is likely on account of the anisotropic structure of these DN hydrogels, in which re-swelling occurs primarily in the thickness direction allowing the bottom surface to stay in good contact with Au electrodes whereas through-plane connections may be slightly worsened. Over the time tested, both resistance values maintained ca. ±10 % of their initial values, giving confidence towards the use of this method to prepare devices.

2.2.2 Pseudo-capacitance

Methods

As a conjugated polyelectrolyte system, PEDOT:PSS is rich in electrochemical features owing to both the accessibility of π-bonded electrons to external electromagnetic fields and to the gel structure which allows for the exchange of ions (i.e., intercalation) [41, 115, 118, 119]. Accordingly, our DN hydrogels are expected to be highly pseudo-capacitive. As such, we used cyclic voltammetry (CV) and impedance spectroscopy (IS) to characterize the electrochemical properties of the system, using either an ALS 618E electrochemical analyzer or Solartron 1470 potentiostat/1455 frequency response analyzer.

In all electrochemical testing, unless otherwise noted, DN hydrogels were equilibriated in fresh 1 × PBS (pH 7.4) for at least 15 min. A typical three-terminal electrochemical cell was assembled on device substrates by first blocking the majority of exposed Au using a PDMS gasket cut from a 10 µm sheet (as required), placing a silicone o-ring to encircle the solution area, and clamping a glass ring on top. Into the solution chamber, a Ag/AgCl wire in saturated KCl was connected as a reference electrode (RE) via an agar gel salt bridge fashioned from a micro-pipette tip. A Pt wire coiled around the tip without shielding its opening served as the counter electrode (CE). This allowed for positioning the RE within 2 to 3 mm of the working electrode (WE) and minimized the effect of solution resistance.

For IS, a consistent electrochemical state was first established in the DN hydrogel by running CV measurements between cathodic and anodic potentials to PEDOT with a sufficient number of cycles. Thereafter, OCP was measured for enough time to stabilize the drift in V_{oc}. Unless otherwise noted, a standard set of parameters was used for IS, with a DC potential of 0 V vs. Ag/AgCl and an AC signal of 10 mV. Fitting of impedance spectra was performed by complex non-

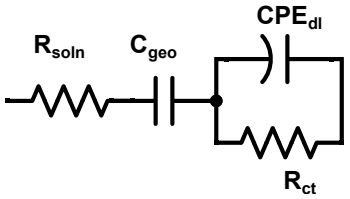

Figure 2.11: Equivalent circuit for EIS fitting.

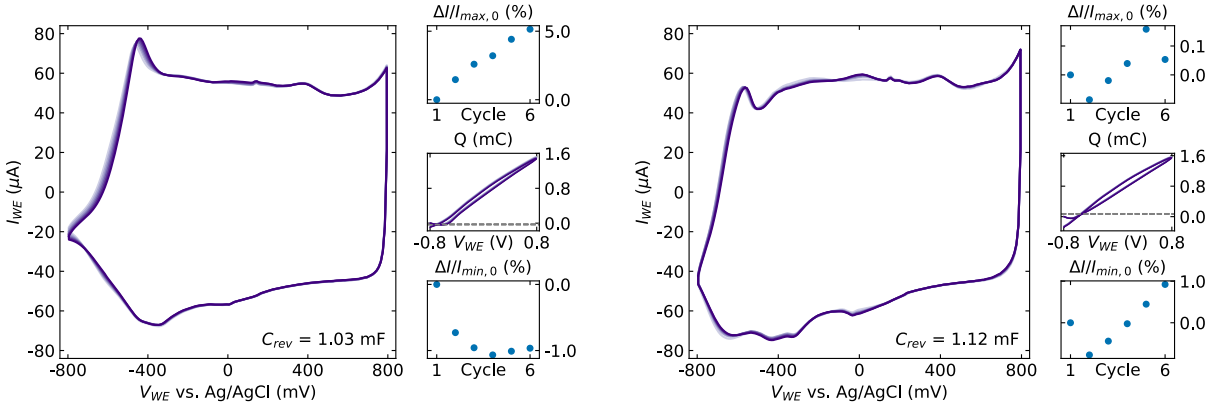

(a) PBA-0 (b) PBA-6

Figure 2.12: Cyclic voltammetry of DN hydrogels in 1 × PBS at a sweep rate of 50 mV/s. Later cycles appear in darker shades. Auxiliary plots show the percent change in peak currents with repeated cycles, in addition to coulovoltammograms obtained by numerical integration. In the latter, a dashed line indicates the point of intersection to define Q_{loop}.

linear least squares (CNLS) [120] in a custom written Python 3.8 library employing solvers included in *optimize.least_squares* (SciPy 1.7.x) with the equivalent circuit depicted in Fig. 2.11. This simple 4 lumped element circuit empirically describes the frequency dependent impedance of solution/series electrode resistances by R_{soln}, volumetric charge storage by C_{geo}, and Faradaic reactions by the parallel combination of a constant phase element, CPE_{dl}, and charge transfer resistance, R_{ct} in:

$$Z_T(\omega) = R_{\text{soln}} + \frac{1}{j\omega C_{\text{geo}}} + \frac{R_{\text{ct}}}{(j\omega)^n C_{\text{dl}} R_{\text{ct}} + (j\omega C_{\text{dl}}^{1/n})^{2n}} \tag{2.4}$$

Additional elements such as Warburg impedance to represent diffusion-controlled charge transfer may be considered, but generally speaking the impedance of CPs subject to space-charge limited current (i.e., conductance determined by current injection) can be well modelled by simplified equivalent circuits with R_{ct} and C_{geo} as key parameters [121, 122].

By cyclic voltammetry

Figure 2.12 shows CV of typical DN hydrogels in PBS. Large, box-shaped curves are observed and are characteristic of ion-permeable CPs with large capacitance afforded by the high areal density of EDLs arising due to charge transfer involved in oxidation of polarons to bipolarons [119]. A concomitant shift in chemical potential of the CP results in a built-in potential that drives the spatial separation of holes and counter-ions [41].

The charge storage capacity (CSC) is estimated by the change of reversible charges

during a potential cycle:

$$Q = \int I_{WE}\, dt$$
$$C_{\text{rev}} = \frac{Q_{\text{max}} - Q_{\text{loop}}}{(V_{\text{max}} - V_{\text{loop}})} \tag{2.5}$$

where Q_{max} is the total charge injected when reaching the anodic turning point, V_{max} (i.e., the constant of integration sets Q to zero at the cathodic starting point). The point (V_{loop}, Q_{loop}) is defined at the intersection of anodic and cathodic Q curves, which closes the loop and serves as an estimate of the reversible charges[4] injected by the potentiostat [115, 118]. The average value over the measured sweeps is reported in Fig. 2.12. When normalized to the geometric volume, a volumetric capacitance of ca. 2.5 F/cm^3 is obtained, a factor of 100 away from PEDOT:PSS hydrogels optimized as supercapacitors [98].

Besides the capacitance value, a few qualitative observations can be made. First, both compositions of DN hydrogel exhibit an oxidation peak near −500 to −600 mV which is typical of (slow) hole injection into PEDOT [41]. In PBA-6, this peak is lower and more negative, suggesting that PEDOT in this composition is more readily oxidized. At the same time, larger reductive currents are observed and irreversible negative charges are evolved during the cathodic portions of CV in PBA-6 as indicated by the coulovoltammograms. This is likely related to the electro-catalyzed reduction of dissolved O_2 as discussed in Chapter 3. It may also be viewed as a secondary doping effect of PBA, which increases the carrier concentration in the DN hydrogel. Finally, voltammograms of both compositions exhibit minimal change in their shape with repeated cycling to cathodic potentials, demonstrating good stability of the material and the electrode contacts.

By impedance spectroscopy

Figure 2.13 shows the impedance spectra for the same samples of hydrogel as in Fig. 2.12. At low frequencies <100 Hz, significant capacitive character is observed, as evidenced by the vertical trace in complex capacitance space and phase angles approaching −90°. Accordingly, the values of C_{geo} extracted from fitting (ca. 1.0 mF) are in excellent agreement with the CSC determined by CV, as expected for fully ion-permeable CPs [119]. At V_{DC} = 0 V vs. Ag/AgCl, these DN hydrogels are already fully oxidized, leading to low impedance features at high frequencies which, by their nature, are more prone to instrument/apparatus artefacts [123, 124] and are difficult to fit by the simple RC element in Fig. 2.11, as indicated by large systematic errors in the fit residuals.

[4]For an ideal capacitor, this is simply the cathodic Q_{min}. The presence of a reversible redox couple introduces a symmetric increasing and decreasing step into the integrated Q, and is thus included. However, any irreversible charges will be asymmetric, shifting the point at which the loop closes.

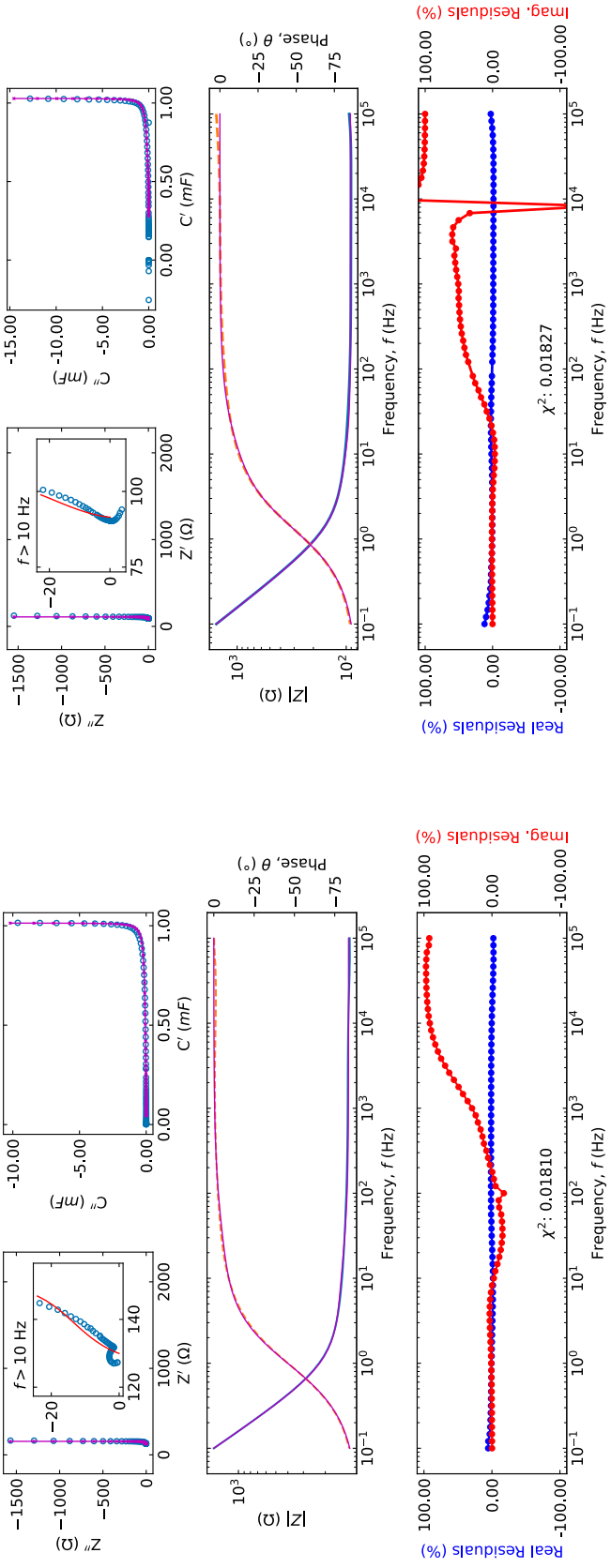

(a) PBA-0 (b) PBA-6

Figure 2.13: Impedance spectra presented as a Nyquist plot with inset showing higher frequency components (top left), transformed into complex capacitance (top right), Bode plots (middle), and the residuals from equivalent circuit fitting (bottom). Data was obtained at $V_{DC} = 0\,\mathrm{V}$ vs. Ag/AgCl and $\Delta V = 10\,\mathrm{mV}$, in PBS.

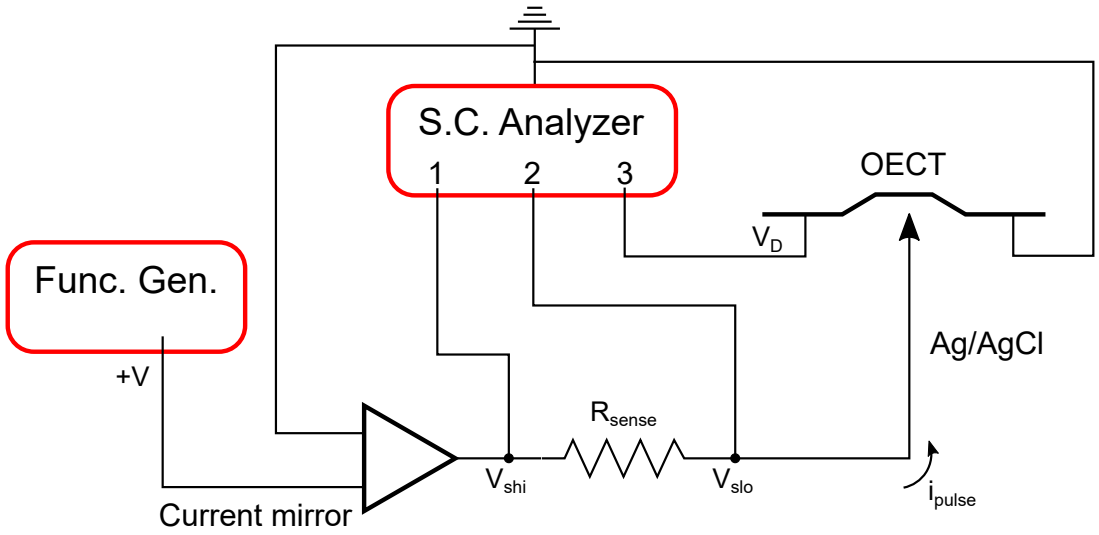

Figure 2.14: Schematic diagram for the electrical connections used in time-of-flight measurements.

Large C_{geo} and inversely proportional small R_{ct} arises as a physical consequence when the filling of a Gaussian distribution of states in the HOMO is tightly controlled by the applied potential [121, 122]. Whereas R_{ct} additionally depends on the electrolyte/semiconductor interface, C_{geo} is determined by the behaviour in the bulk. Therefore, it is sufficient to consider simply the low frequency spectra to extract C_{geo}.

2.2.3 Time-of-flight carrier mobility

Methods

The gated three-terminal structure of OECTs allows for the measurement of the time-of-flight of injected carriers. That is, the time required for the applied electric field across the OECT channel to sweep hole charges to ground potential. Typically, carrier injection is performed by photoinduced carrier generation (i.e., photoelectric effect), however, in organic semiconductors, permeability to ions allows this to be done ionically [49].

A gate current pulse[5] of 10 s duration was applied via the non-polarizable Ag/AgCl RE by a Tektronix AFG3102 function generator and a home-built current mirror circuit. To provide a stable interface for Faradaic current injection, the RE surface area was increased and applied current was monitored simultaneously with OECT channel current (at $V_D = -100\,\text{mV}$) via the potential drop across a 6.8 kΩ sense resistor connected in series with RE (i.e., $I_{\text{sense}} = (V_{shi} - V_{slo})/R_{\text{sense}} = i_{\text{pulse}}$), using the Keysight B1500A as depicted in Fig. 2.14. After reaching steady-state of I_D with applied V_D, the potential at the low end

[5] A potential pulse may be used as well, as is common for organic thin-film FETs [125, 126], though in this case, the amount of injected carriers depends on the capacitive coupling of the gate to the channel.

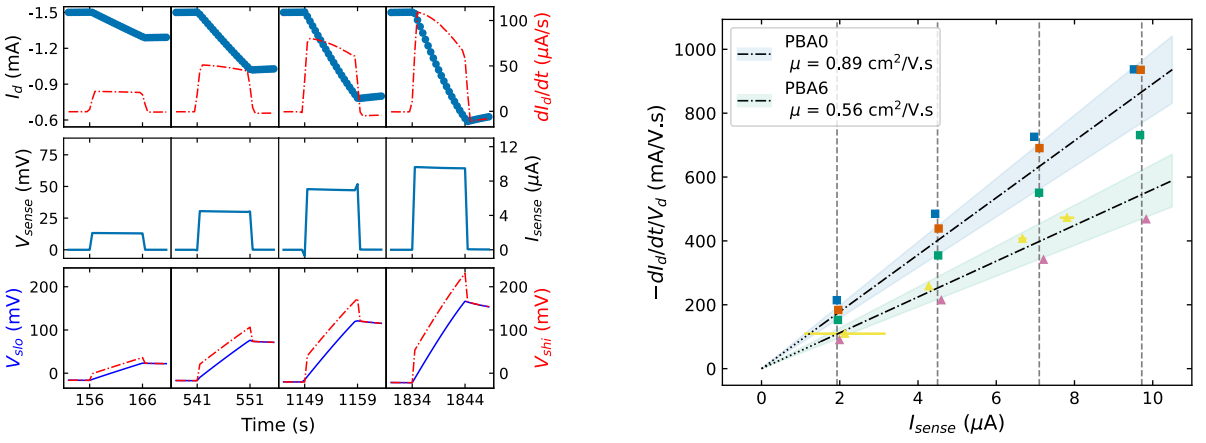

(a) (b)

Figure 2.15: Time-of-flight measurement to determine carrier mobility in DN hydrogel OECTs. Current transients (a) show the change of I_D at $V_{DS} = -100\,\text{mV}$ with applied current from the gate. Distribution of mobilities (b) for PBA-0 (□) and PBA-6 (△) hydrogels. Shaded regions show the first standard deviation, with dot-dashed lines showing the regression lines. Vertical dashed lines show the current output of the current mirror circuit when in compliance.

of the sense resistor was noted, which corresponds to the OCP of the channel vs. Ag/AgCl (i.e., $I_g = 0$). After each current pulse, sufficient quiescent time was allowed for the channel to reach this potential again before applying the subsequent pulse.

The carrier mobility can be extracted by applying current pulses of varying magnitude and taking the slope of the $\partial I_D/\partial t$ vs. I_g plot [49]:

$$\begin{aligned} I_D(t, I_g) &= I_o - I_g(f + \frac{t}{\tau_e}) \\ \tau_e &= \frac{L^2}{\mu V_D} \\ -\frac{\partial I_D}{\partial t} V_D &= \frac{\mu}{L^2} I_g \end{aligned} \tag{2.6}$$

where I_o is a baseline starting current related to the initial carrier density in the channel, I_g is the applied gate current, f is a factor ranging from 0 to 0.5 that relates to the electrochemical state of the CP (i.e., redox currents from the gate) and asymmetry due to source-drain bias [49, 55], and τ_e is the characteristic time constant for carrier drift. The carrier mobility relation, assuming a planar electric field of V_D across L, gives μ from the slope of the graph. Note that in our OECTs, $L = 0.1\,\text{cm}$.

High carrier mobilities

The current transient data of a typical time-of-flight measurement, sectioned to the duration of the applied pulses, are shown in Fig. 2.15a. With $V_{DS} < 0\,\mathrm{V}$, the response of the channel to return to the initial steady state current was significantly faster than for positive V_{DS} (raw data not shown). This response is determined by the rate at which ions can exit the DN hydrogel, though in this experimental set up, the means of connecting of the RE (i.e., via a salt bridge) will be a limiting factor since the potential at the Ag/AgCl interface must change accordingly when the oxidation state of PEDOT is altered. Regardless, the extracted slopes did not significantly differ based on the sign of V_{DS}.

The data for extraction of time-of-flight mobility as in Eq. (2.6) is summarized in Fig. 2.15b for both DN hydrogel compositions. In the absence of PBA, a value of $0.89 \pm 0.10\,\mathrm{cm^2/(V\,s)}$ is extracted and is remarkably high considering the composite structure (cf. optimized thin-film PEDOT:PSS at 1 to $2\,\mathrm{cm^2/(V\,s)}$ [40, 70]). With PBA included, mobility is decreased ∼60 % to $0.56 \pm 0.08\,\mathrm{cm^2/(V\,s)}$. Note that μ in this measurement describes the mobility of carriers near the Fermi level of heavily doped PEDOT [49]. Considering the similar values of swollen conductivity, this suggests that carrier density is nearly twice as large in PBA-6 compared to PBA-0 hydrogels, with $p \sim 10^{20}/\mathrm{cm^3}$ for both. Given the influence of PBA on measured CV, in addition to larger I_D for PBA-6 OECTs observed at this operating point, the reduction of μ is most likely the result of carrier self-interactions at high densities [50, 127–129].

2.3 OECT device characteristics

Having now independently determined estimates for the carrier mobility and volumetric capacitance of our DN hydrogels, we can compute the μC_{vol} figure-of-merit [70], used to benchmark CP materials for ionic amplification. Here, we obtain μC_{vol} ranging from 1.4 to $2.2\,\mathrm{F/(cm\,V\,s)}$, which is an order of magnitude off from optimized thin-films or thick layers of printed PEDOT:PSS [93, 94]. However, compared to previous reports of composite PEDOT:PSS prepared by 3D printing [96], these DN hydrogels are an order better because of high carrier mobilities arising from good phase compatibility between PEDOT:PSS and the poly(acrylamide)-based second network.

Note that μC_{vol} is most relevant when the input signal is evolved in the ionic circuit under the action of applied (effective) gate potential. In response, large C_{vol} produces the greatest change in carrier density. However, when the signal arises within the channel, this perspective changes as large C_{vol} hinders the shift of channel potential. In this case, μ should be prioritized over C_{vol}, as exhibited in our DN hydrogels employed as OECTs.

2.3.1 Output and transfer curves

Methods

For characterization of OECT devices, the aforementioned RE/CE configuration used to ensure proper thermodynamic referencing for electrochemical characterization was applied to measurements with the Keysight B1500A semiconductor analyzer. This was achieved by connecting the RE to the sense and the CE to the force terminal of a source-measure unit in a modified Kelvin contact, to achieve a similar arrangement of feedback circuitry as in traditional potentiostats [130]. In this set-up, the WE is established by the grounded source contact when exposed to electrolyte.

In this way, full accounting of charge in the electrochemical cell is made possible, enabling coordinated studies of conduction in the channel with electrochemical processes occurring at the gated interfaces [131–133] (see also Appendix A). For such a measurement, the leakage current to the gate can be considered as a voltammogram, though its orientation/sign convention is inverted with respect to electrochemical customs. Its value represents current contributions between both source and drain [55] and may be affected by fluctuations of the surface condition of the CE. Therefore, we performed all OECT characterization with generally the same procedure as in Section 2.2.2, except where blocking of exposed Au would interfere with adjacent devices on the same chip.

Results

Figures 2.16 and 2.17 present the steady-state output (a, b) and extracted transfer characteristics (c) in the saturation regime ($V_{DS} = -500\,\mathrm{mV}$) of DN hydrogel OECTs. Both compositions exhibit the expected p-type conduction, with I_D being suppressed at sufficiently large positive V_{LG} due to the drift of cations into the DN hydrogel. Moreover, the lineshape of I_G in (Fig. 2.16d and Fig. 2.17d) confirms that I_D saturation is due to pinch-off of the channel by de-doping of the drain contact. That is, by taking the local electrode potential as $V_D - V_{LG}$, it is apparent that the trace follows I_{WE} of the CV in the cathodic region (cf. Fig. 2.12).

Pinch-off or threshold potentials, V_p, extracted by extrapolating a linear regression of $\sqrt{I_D}$ vs. V_{LG} to the abscissa (transformed data not shown) were on average 0.41 V for both compositions ($\mathrm{N} \geq 3$). Unfortunately, the tested sample size is not large enough to meaningfully determine a statistically significant difference. However, qualitatively speaking, the cathodic tails of I_G in Fig. 2.16d and Fig. 2.17d appear to taper more slowly in DN hydrogels containing PBA. This suggests that PBA is electrochemically active as a secondary dopant of PEDOT, though additional characterization of its effect on the density

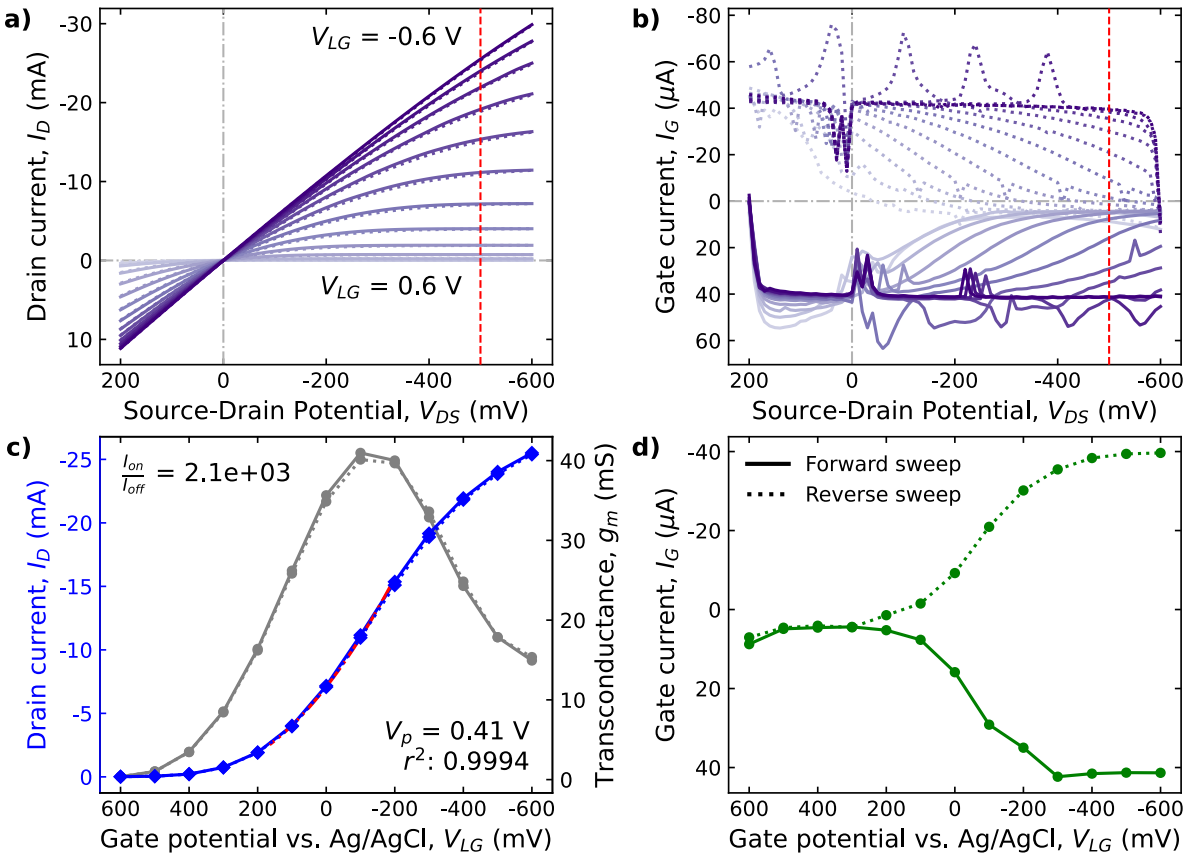

Figure 2.16: Steady-state output (a, b), extracted transfer (c), and gate leakage (d) curves of a representative PBA-0 hydrogel OECT in PBS (pH 7.4). Average $dV_{DS}/dt = 66\,\mathrm{mV/s}$ for V_{LG} ranging from -600 to $600\,\mathrm{mV}$, with accumulating V_{LG} in darker shades. Red dashed lines show the slice at $V_{DS} = -500\,\mathrm{mV}$ to extract (c, d). Right axis of (c) shows the transconductance, g_m, by numerical differentiation. In all subfigures, solid lines represent the data from the first half of a cyclic sweep.

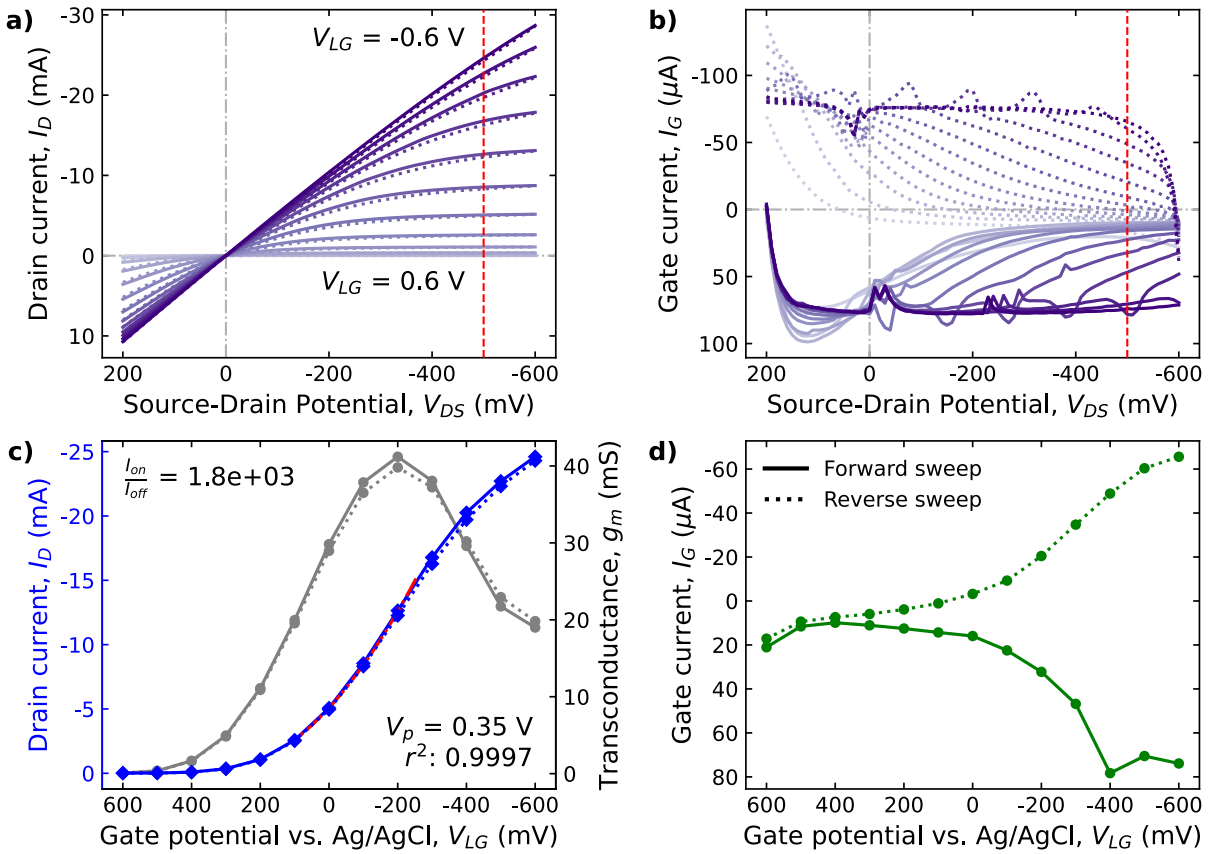

Figure 2.17: Steady-state output (a, b), extracted transfer (c), and gate leakage (d) curves of a representative PBA-6 hydrogel OECT in PBS (pH 7.4). Average $dV_{DS}/dt = 66\,\text{mV/s}$ for V_{LG} ranging from -600 to $600\,\text{mV}$, with accumulating V_{LG} in darker shades. Red dashed lines show the slice at $V_{DS} = -500\,\text{mV}$ to extract (c, d). Right axis of (c) shows the transconductance, g_m, by numerical differentiation. In all subfigures, solid lines represent the data from the first half of a cyclic sweep.

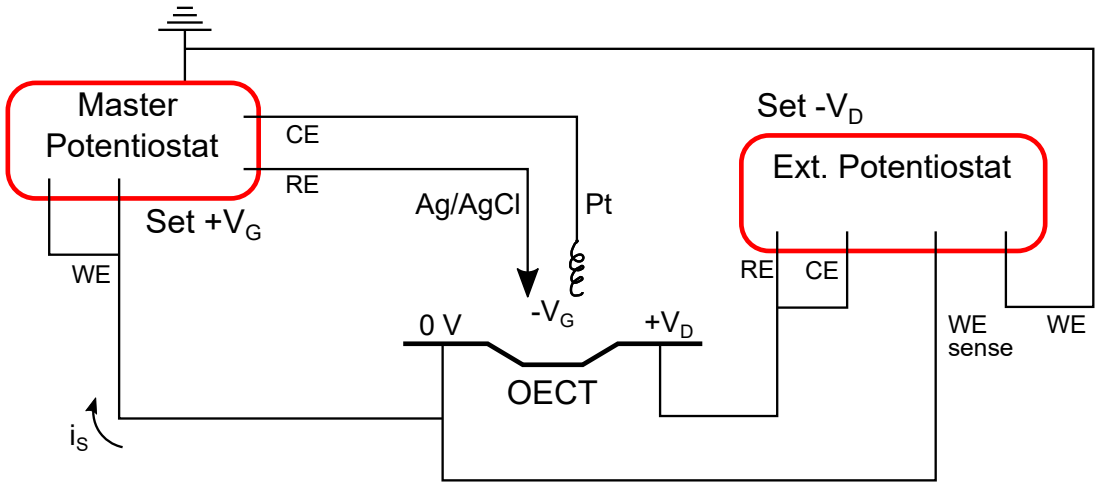

Figure 2.18: Schematic diagram for a bi-potentiostat connection used for small signal transconductance measurements. A potentiostat with a built-in signal generator and frequency analyzer is used as the master. The WE and WE-sense terminal of an external potentiostat connected as shown allows all channel current (I_S) to flow into the master.

of states (e.g., defect/trap states near the HOMO edge) using electro-spectrophotometry or EIS measurements will be needed to corroborate this interpretation.

The devices depicted demonstrate exceptional switching performance for OECTs, with high on-off ratios $\sim 2 \times 10^3$ and peak transconductance around 40 mS at $V_{LG} = -200$ mV. In other DN hydrogel device samples on-off ratios of 700 to 1200 were typical, while the highest g_m of 58 mS was also observed. These large g_m are afforded by the large thickness [58] of swelled hydrogels—although C_{vol} is $\sim 100\times$ smaller, channel thickness is $\sim 1000\times$ larger with respect to typical thin-film PEDOT:PSS OECTs.

Non-monotonic g_m vs. V_{LG} is apparent and has been identified as an intrinsic property of electronic transport in CPs due to the effect of structural disorder on the density of states [127] (see also Section 2.2.3). At the same time, comparable values of contact and channel resistance further suggest that extracted g_m may also be diminished by parasitic losses (i.e. an additional V_D drop at the drain contact) [52, 69]. Regardless, our DN hydrogel OECTs routinely demonstrate efficient ion-coupled gating and exhibit steady-state characteristics on par with the state-of-the-art.

2.3.2 Small-signal (AC) transconductance

Methods

To determine the frequency response of DN hydrogel OECTs, small-signal (AC) transconductance measurements were conducted in the same manner as IS (see Section 2.2.2), with V_D provided by a second potentiostat (PS-14D, Toho Technical Research) connected to

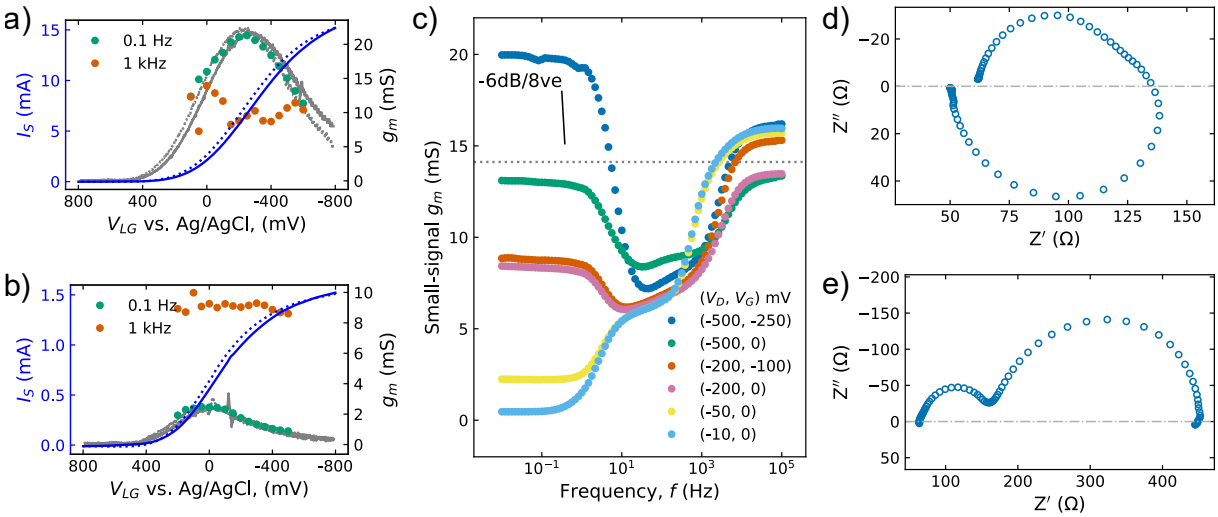

Figure 2.19: Transfer curves (a, b) of a PBA-0 DN hydrogel OECT collected at a sweep rate of 25 mV/s using a bi-potentiostat at $V_D = -500$ and -50 mV, respectively. DC and small-signal transconductance is plotted against the right axis. Small-signal g_m (admittance) versus frequency (c) for various operating points (V_D, V_G). Inset shows the attenuation of a first-order filter and corresponding -3 dB cutoff based on (-500, -250). Complex impedance plots (d, e) for the (-500, -250) and (-50, 0) mV curves in (c), respectively.

the drain (RE/CE) and source (WE sense) of the OECT. To complete the circuit without diverting currents from the OECT channel, the WE terminal of the second potentiostat was bridged to instrument ground of the primary potentiostat. This arrangement is shown schematically in Fig. 2.18. The operating point of the OECT is fixed by V_D and V_G set by two potentiostats and the built-in measurement procedure to perform impedance spectroscopy by the primary potentiostat gives directly the small-signal g_m as the calculated admittance output (i.e., $1/Z(\omega) = i_S/v_G$).

In this manner, AC measurements can be made simply on OECTs using equipment common to electrochemical laboratories, as opposed to previous studies [55, 56, 59, 60, 65, 134] using separate instruments for waveform generation, phase-correlated signal amplification, high-bandwidth read-out (i.e., digital storage oscilloscope), and custom software-based measurement control. However, we note that having these as separate instruments is more flexible for experimental design, and may potentially have greater bandwidths.

Results

When compared to g_m of the DC steady-state transfer curves (Fig. 2.19a,b), the AC values show good agreement at low frequency for both linear and saturation regime operation, whereas at high frequency g_m becomes independent of DC V_{LG}, with both measurements at 1 kHz approaching the same value of ca. 10 mS. Figure 2.19c shows the frequency

dependence of small-signal g_m for a PBA-0 DN hydrogel OECT at various operating points spanning linear and saturation regimes. In all curves, a transition at low frequency ca. 10 Hz corresponding to a pole in the transfer function (i.e., $H(\omega) \equiv \text{output/input} = g_m$) is observed. When the OECT is in saturation (Fig. 2.19d), this appears as the part of Z in the first quadrant (i.e., $\text{Im}(Z) > 0$) and is characteristic of a voltage controlled current source. That is, when operating as an amplifier, the output i_S will match an oscillating input v_G in phase until g_m begins to cut-off and i_S will show a delayed and eventually no response to the control of v_G (i.e., positive phase as i_S leads v_G).

Hence, a characteristic cut-off frequency can be determined using the customary definition for a first-order filter, that is, -3 dB, or when g_m has decreased to $1/\sqrt{2}$ of its original value. This limit is shown as the dotted line in Fig. 2.19c for the most performant operating point and matches the transition point discussed above. However, g_m does not remain attenuated and increases again with frequency. This corresponds to the semi-circle in the third quadrant of the complex impedance plot and is similar to the spectra expected for a simple parallel RC circuit. This suggests that the limited frequency response is due to the ionic circuit formed at exposed contacts in electrolyte. Interestingly, when the OECT is in the linear regime, no cut-off of g_m is observed; rather, the output proceeds to the same electrolytically dominated behaviour above 1 kHz. Therefore, relatively slow ionic uptake into the bulk and the influence of exposed contacts limits operation of our DN hydrogels to the low frequency regime (<10 Hz), requiring consideration towards minimizing surface area or thickness of the channel (i.e., $\tau_i \propto d\sqrt{WL}$) and targeting suitable applications.

For instance, real-time measurement of small signal g_m has been proposed as a method to extact more stable signals from OECT biosensors [134]. In the typical implementation, the interface potential changes according to electrochemical reactions of analyte at the gate (i.e., a Nernstian response) with a concomitant g_m curve shift. Thus, the bandwidth of typical thin-film OECTs employed as ionic amplifiers is sufficiently large and the frequency dependence of the sensing signal was not a subject of consideration in Ref. 134. However, a low cut-off frequency in thick DN hydrogel OECTs poses the question of whether an inherently formed low-pass filter may be used to reject noise in physiological contexts. That is, in addition to an applied DC potential providing thermodynamic control, the selected AC frequency may serve to provide kinetic control of electrochemical signals.

2.3.3 Bias scaling of device parameters

High electrical conductivity and low resistance ohmic contacts to DN hydrogels invite the operation of OECTs in the linear bias regime, which was dismissed in early OECT studies as a way to tune device characteristics (e.g., V_G at maximum g_m) for sensing applications

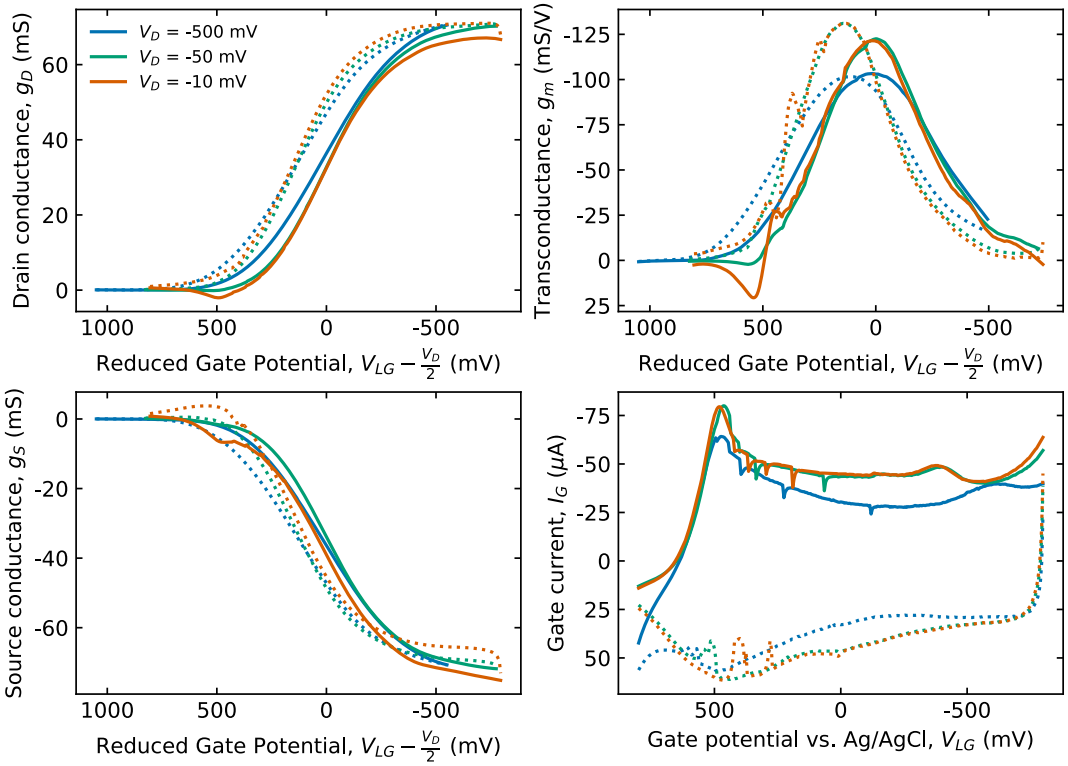

Figure 2.20: Drain and source conductances (I/V_D), transconductance based on the drain, and gate current for a transfer measurement of a PBA-6 DN hydrogel OECT in PBS. V_D was varied to bias the OECT in the linear and saturation regimes, with a gate sweep rate of 27 mV/s. Solid (dashed) lines represent the leading/anodic (trailing/cathodic) sweep.

[56]. The reason for this lies in the considerable Faradaic leakage from the contact regions, which dominates the measured output as can be seen in Fig. A.8 for a thin-film OECT. Instead, it was suggested that the optima of g_m be controlled via channel geometry (i.e., aspect ratio [56], thickness [58]) in conjunction with saturation bias to increase its value. This is apparent by taking the derivative of Eqs. (1.3) and (1.4):

$$g_m \equiv \frac{\partial I_D}{\partial V_G} = \begin{cases} \frac{-W \cdot d}{L} \mu_o C_g V_D, & V_D > V_{D,\text{sat}} \\ \frac{-W \cdot d}{L} \mu_o C_g V_{D,\text{sat}}, & V_D < V_{D,\text{sat}} \end{cases} \tag{2.7}$$

where $V_{D,\text{sat}} = V_G - V_p$ has been substituted into the second expression in saturation. Accordingly, g_m ought to scale linearly with V_D until saturation at a specified V_G and thus represents the maximum amplification. However, it has been noted that accurate methods to estimate V_p are required to truly identify the optimum point of $V_{D,\text{sat}}$ [50]. This is due to the bias dependence of both carrier mobility and electric double-layer capacitance.

On the other hand, coordinated OECT measurement and gate voltammetry can provide

estimates for both of these parameters simultaneously as the bias point is varied. To illustrate, Fig. 2.20 presents transfer curves for a PBA-6 DN hydrogel OECT normalized by V_D (i.e., drain/source conductance). Also note that the curves are translated by the average potential in the channel (i.e., $V_D/2$), to correct for the influence of V_D on applied V_{LG} (see Eq. (1.3)). This causes the curves at various bias points to collapse on each other, except where non-linear effects are present, such as oxidation or saturation.

Even at the lowest operating bias of $V_D = -10\,\mathrm{mV}$, lateral conduction from source to drain is observed. Furthermore, redox peak features in the gate voltammogram, such as the oxidation of PEDOT near $V_{LG} = 500\,\mathrm{mV}$ are more clearly distinguished in g_D and g_S during cyclic sweeps in the linear regime. At the smallest bias, these Faradaic current features are shared between source and drain according to the f-factor in Eq. (2.6) that approaches 0.5 with decreasing $|V_D|$ [55]. Moreover, these features are amplified in the g_m curves calculated by numerical differentiation but are strongly attenuated as the magnitude of V_D increases.

This is due to the increased electric field in the channel which decreases the time (and probability) for an electrochemical interaction of a charge carrier before being swept into the contact. Hence, at $V_D = -500\,\mathrm{mV}$, non-linearity in the gate voltammogram is observed as a squeezed box shape and anodic peak shift of the oxidation feature nominally at $V_{LG} = -400\,\mathrm{mV}$. At the same time, the cathodic PEDOT oxidation peak remains at a consistent potential $\sim$500 mV because the channel is depleted. Whereas attenuation of Faradaic leakage currents in saturation may be desirable for stable operation as an ionic amplifier in typical OECT biosensor applications, when the desired signal is electrochemical in nature and originates within the channel directly, operation in the linear regime will rather maximize the response. Here, small V_D allows both source and drain regions to contribute to the gate current.

Furthermore, g_m in the linear regime reaches its maximum in anodic sweeps at $V_{LG} \approx 0\,\mathrm{V}$ when compared to the saturation regime, since applied gate potential no longer needs to counter-act large V_D to reach the same operating point. In Fig. 2.20, a lower value for the the normalized g_m peak is also observed, which stems from an underestimate of g_m/V_D because $V_{D,\mathrm{sat}}$ is not used. To quantitatively determine the bias scaling of device parameters, values were extracted graphically by combining Eqs. (2.5) and (2.7):

$$-\frac{\partial I_D}{\partial V_{LG}}\frac{1}{V_D} = \frac{\mu_{OECT}}{L_{ch}^2}\frac{C_{\mathrm{rev}}}{1+\frac{L_{con}}{L_{ch}}} \tag{2.8}$$

where the volumetric C_g is replaced by the CSC determined from the gate voltammogram simultaneously collected. All geometric factors apart from the ratios of contact and

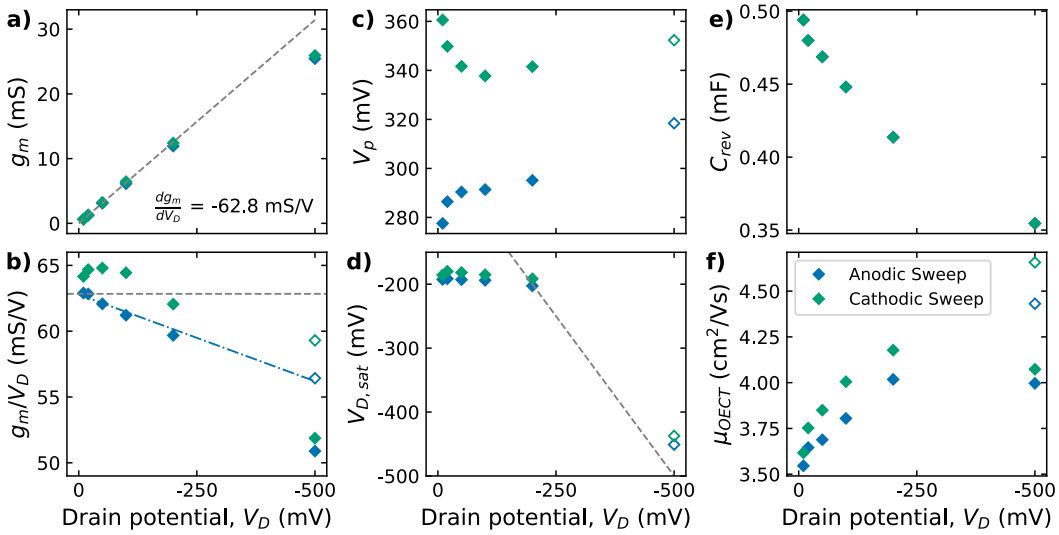

Figure 2.21: Drain potential dependence of transconductance (a), normalized transconductance (b), pinch-off voltage (c), saturation drain potential (d), reversible charge storage capacity (e), and OECT mobility (f) of a PBA-0 DN hydrogel. Data extracted from transfer curves in PBS with a gate sweep rate of 27 mV/s. Dashed lines in (a,b) indicate the short-circuit g_m by regression in (a). Dot-dashed line in (b) serves as a guide-to-the-eye of the trend in g_m/V_D. Dashed line in (d) indicates the boundary of the inequality where $V_D = V_{D,\mathrm{sat}}$. Unfilled data markers represent points corrected using $V_{D,\mathrm{sat}}$.

channel lengths cancel, giving a capacitance which is reduced by a factor of $1 + L_{con}/L_{ch}$. $\partial I_D/\partial V_G$ is determined by regression in a linear region with respect to V_{LG} (linear) or V_{LG}^2 (saturation). Accordingly, V_p is also extracted from the regression parameters, with correction for $V_D/2$ in the linear regime or without in the saturation regime (see Eqs. (1.3) and (1.4)). The mid-point potential of this region was taken as V_{LG} to determine $V_{D,\mathrm{sat}}$, which was used in place of V_D for data from saturation regime. Thus, an estimate for μ_{OECT} can be extracted from a single transfer measurement.

Figure 2.21 presents this analysis for a PBA-0 DN hydrogel OECT. Un-scaled g_m in Fig. 2.21a deviates from a linear relationship with V_D in saturation at -500 mV. A limiting value for g_m/V_D (i.e., at short circuit) can be extracted by linear regression of these data, giving a value of -63 mS/V. For small V_D, normalized g_m in Fig. 2.21b approach this value[6], whereas $g_m/V_{D,\mathrm{sat}}$ remains low even after correcting for the operating point. Figure 2.21c,d shows the values of $V_{D,\mathrm{sat}} \approx -200$ mV predicted from linear transfer curves, with the corresponding (filled) data points falling below the boundary line (i.e., $V_D > V_{D,\mathrm{sat}}$). As expected, the corrected point in saturation lies above the boundary. From the idealized model of Eq. (2.7) a monotonically decreasing trend of g_m/V_D cannot

[6]Higher values observed in the cathodic sweeps may be due to a shift in channel potential by capacitive charging during a transfer sweep.

be explained, therefore suggesting that parasitic losses arise with increasing V_D.

Drain bias-dependent capacitance (Fig. 2.21e) is also apparent, with C_{rev} decreasing non-linearly by 30 % over the range of V_D. This agrees with qualitative observations of the shape of I_G in Fig. 2.20. Neglecting a change in effective channel length with the onset of pinch-off[7], this decrease is greater than the trend in g_m/V_D. Accordingly, extracted μ_{OECT} (Fig. 2.21f) is observed to increase monotonically after correcting for $V_{D,\text{sat}}$. This agrees with the expected trend of mobility with increasing carrier (hole) concentration in disordered semiconducting polymers [128, 129]—in this case, by lowering $V_{D,\text{sat}}$. Therefore, while earlier studies have astonishingly dismissed the linear regime of OECT operation, we propose that so long as the output current is sufficiently large for easy read-out (i.e., $g_m(V_D = -10\,\text{mV}) \approx 1\,\text{mS}$), low-bias operation should prove to be the most sensitive for electrochemical signals directly originating in the OECT channel.

2.4 Conclusions

In this chapter, we detailed a simple method to prepare conductive polymer hydrogels using a double-network approach with PEDOT:PSS and rationally designed poly(acrylamides). Additionally, a thermo-mechanical annealing process was considered and produced electrical contacts that were surprisingly stable and reliable even in physiological, wet media. Despite this, fast and reversible swelling in electrolytes was obtained, with structurally-significant thickness of $\sim$100 µm corresponding with water content similar to biological soft tissues.

By carefully characterizing the fundamental properties of DN hydrogels, we came to the realization that their remarkable electrical transport (i.e., $\mu \sim 1\,\text{cm}^2\,\text{s/V}$, $C_{\text{vol}} \sim 2.5\,\text{F/cm}^3$, $\sigma \sim 20\,\text{S/cm}$ in PBS) arises from good phase compatibility between PEDOT:PSS and the second network. Accordingly, we determined the OECT figure-of-merit for these hydrogels to be convincing for the continued development as high performance materials for a biosensing platform. To successfully achieve this, the diffusively limited frequency response ($f < 10\,\text{Hz}$) of hydrogel OECTs will need to be addressed by a combination of miniaturization, composition, device operation, and targeted application.

Importantly, these hydrogel OECTs have the requisite properties to enable operation in the linear regime (i.e., low potential) which is highly promising for improved biocompatibility. At the same time, the inclusion of PBA moieties in second network produces a noticeable change in the electrochemical properties of the composite hydrogel. For instance, carrier concentration and capacitance is increased although the amount of anionic

[7]This is reasonable considering the long channel and expected potential drop at the drain [111].

charge in the polyelectrolyte ought to be decreased as the pKa of PBA is higher than the pH of PBS. This secondary doping effect is also observed in the altered depletion behaviour of PBA-6 hydrogel OECTs, indicating that a change to the electronic structure of PEDOT is at play. Therefore, our results establish these conductive hydrogels as a viable platform for the engineering of soft materials for biosensing.

Chapter 3

Electrochemical detection of glucose with PEDOT:PSS hydrogels

3.1 Background

In recent years, the reversible esterification reaction between (aryl)boronic acids and vicinal diols has been the subject of considerable attention for engineering detection sites to target diagnostically relevant biomolecules such as glucose or dopamine [135–137]. Stability of the ester depends on the local pH, as the formation of esters is favourable when boronic acid is in its boronate form (pKa ∼9). This provides an external handle on the affinity of the complex, with an equilibrium constant given by [138]:

$$pK_{eq} \approx (pK_{a,\text{acid}} + pK_{a,\text{ester}})/2 \tag{3.1}$$

where pK_a describes the negative logarithm of the association constant of the acid and boronate-ester, respectively. This fact drives the interest in this system because the stability of the complex can be controlled by both environmental (i.e., pH) and fixed (i.e., electronegativity of B) factors, offering a chemically rational design path [139].

For application as detection sites, phenylboronic acids (PBA) have emerged as the most established system because of straightforward chemistries to graft side groups on to the benzene ring. On the other hand, more stable boronic acid ligands can be designed from related aromatic molecules [140]. When employed within CP hydrogels as electrochemical electrodes for biosensing OECT systems, it has been reported that the formation of negatively charged boronate esters induces an observable capacitance change due to an increase in swelling [105]. Alternatively, the ion permeability of a CP layer on the gate electrode is altered by the binding of larger biomolecules [141]. In either case, the

impedance of the ionic circuit connecting gate to OECT channel changes and manifests as an input signal for amplification.

When integrating PBA into bulky DN hydrogels used directly as OECTs, we considered the need for re-investigation as these materials represent a significant departure from the previous work because of their thickness and inclusion of additional polyanions besides PSS. Thus, we hypothesized that a few factors would emerge to form a kinetic basis for a biomolecular signal originating in the channel. First, the local pH in the hydrogel could be lower than bulk due to the presence of anionic polyelectrolytes like PSS [142]. Therefore, when cations are injected by the gate, a local change in ion activity could modulate the equilibrium constant by Eq. (3.1). Second, a kinetic pathway for the reduction of dissolved O_2 to H_2O_2 electro-catalyzed by reduced PEDOT was recently elucidated [143]. The reaction products, involving OH^-, could then be coupled to the PBA equilibrium.

3.2 Methods

Kinetics of electro-catalysis

Firstly, to investigate the kinetics of electro-catalyzed reduction of O_2 on reduced PEDOT, CV was performed according to the procedures discussed in Section 2.2.2 at a series of sweep rates ranging from 361 to 4 mV/s in 1 × PBS (pH 7.4). To control for effects of accumulated irreversible charges (e.g., from the evolution of peroxides), the number of CV sweeps were varied with fast sweeps down to 169 mV/s swept 9 times each, then intermediate sweeps down to 25 mV/s swept 6 times each, and finally the remaining slow sweeps were performed 3 times each. Electrolyte was exchanged for each change of sweep rate, starting from the first intermediate sweep.

The current densities evolved during CV were assumed to originate from two sources: first, the pseudo-capacitance of the interface; and second, a well-defined, diffusion-limited redox couple. Such currents may be distinguished by their sweep rate dependence [18]:

$$\begin{aligned} i(V) &= i_{\text{cap}} + i_{\text{diff}} \\ &= k_1\nu + k_2\nu^{0.5} \end{aligned} \tag{3.2}$$

where k_1 and k_2 are rate constants that describe the contributions of each type of current to the overall peak current, and $\nu = dV/dt$. By plotting $i(V)/\nu^{0.5}$ vs. $\nu^{0.5}$, k_1 and k_2 can be extracted graphically via the slope and intercept, respectively. In the data presented, auxiliary plots corresponding to oxidative peak currents near $V_{WE} = -450$ mV, the current at 0 V in the anodic sweep, and reductive peak currents near $V_{WE} = -450$ mV are plotted

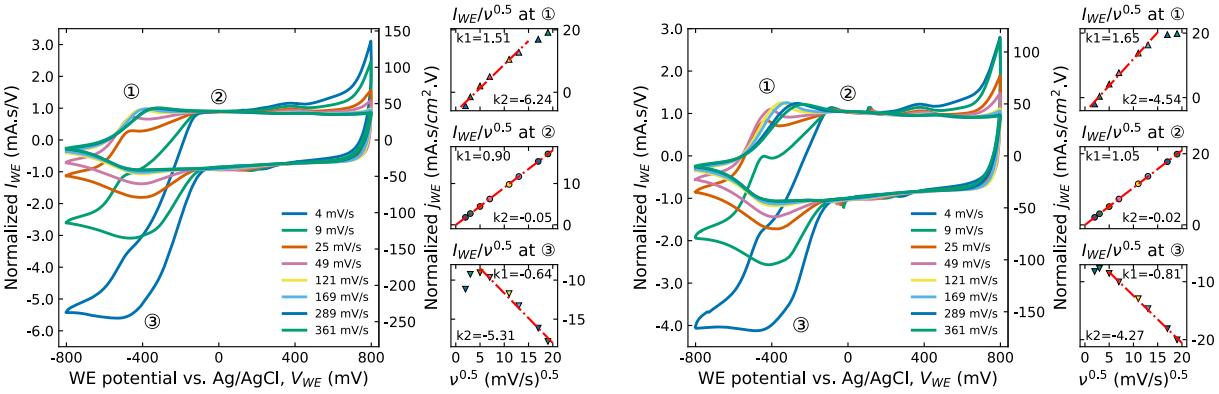

(a) PBA-0 (b) PBA-6

Figure 3.1: Cyclic voltammetry of DN hydrogels in 1 × PBS at various sweep rates. Current and current density data are normalized to the sweep rate to allow for comparison. The final sweep in a series is shown. Auxiliary plots show the sweep rate dependence of oxidative peak currents near $V_{WE} = -450\,\text{mV}$ (top), 0 V (middle), and reductive peak currents near −450 mV (bottom). Dashed lines represent a linear regression to the monotonically changing data points.

in the right-hand side from top to bottom, respectively. Monotonically changing data points are used for linear regression.

Glucose detection

Physiologically relevant concentrations of D(+)-glucose (98.0 + %, Fujifilm Wako Pure Chem. Corp.) in a range of 0.5 to 16 mM were dissolved in PBS as test analyte solutions. EIS, CV, or cyclic OECT transfer measurements with PBA-0 and PBA-6 DN hydrogels were performed as described in Sections 2.2.2 and 2.3.1. After characterization in pure PBS, [glucose] was raised by exchanging ca. 1 mL of analyte over 3 aliquots. Hydrogels were then conditioned in each solution by tracking the open circuit potential before and after EIS, which amounted to a total exposure time of ca. 15 min, after which 6 cycles of CV were performed. The same number of cycles were used in OECT measurements, after a static conditioning time of ca. 15 min. The final set of data from all sweeping measurements are presented.

3.3 Results and Discussion

3.3.1 Kinetics of electro-catalysis

Figure 3.1 shows the family of sweep rate-dependent voltammograms for both compositions of DN hydrogel. After normalization by the sweep rate, it is clear that two regimes of

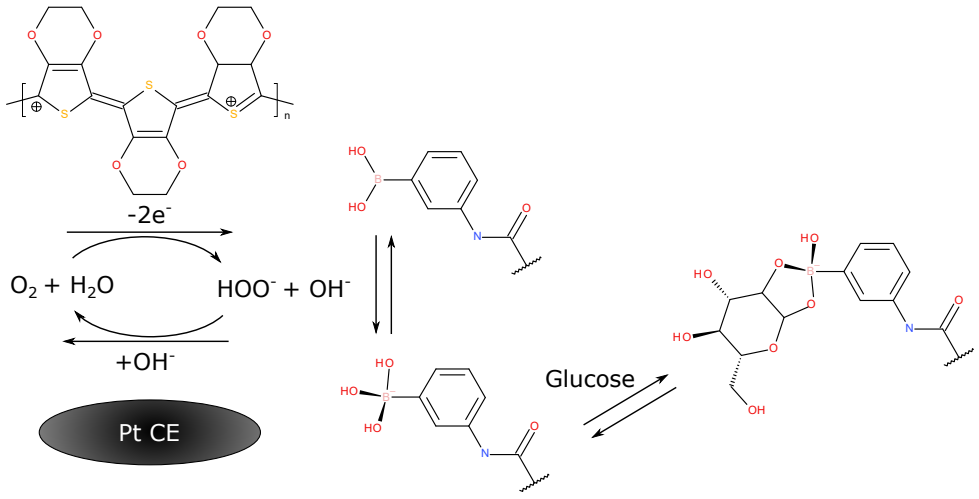

Figure 3.2: Proposed mechanism for the coupling of boronic-boronate acid equilibrium to oxidation state of PEDOT in basic conditions.

electrochemical behaviour occur in these materials. In the anodic region ($V_{WE} > 0\,\mathrm{V}$), nearly pure capacitive character is observed. This is also demonstrated by the middle-right auxiliary plot, which is linear and intercepts the axes close to 0 (i.e., $k_1 \sim 1$ and $k_2 \sim 0$). At the slowest rates and most anodic potentials, peak currents increase according to the evolution of O_2 by electrolysis.

As V_{WE} is cycled to cathodic potentials, significant rate-dependent currents appear at an onset of ca. $-200\,\mathrm{mV}$, which agrees with the intermediate pathway for O_2 reduction reaction (ORR) to H_2O_2 discussed by Ref. 143. Particularly, at the potential for reductive peak currents (bottom-right auxiliary plots), the rate-dependence of I_{WE} is non-monotonic, thus indicating a change of regime. Accordingly, a critical sweep rate for this change is inferred as the turning point in this graph, corresponding to a sweep rate of 25 to 50 mV/s. Therefore, cycling the electrochemical potential at this rate will serve to balance the capacitive and electro-catalytic currents flowing to the DN hydrogel, ensuring that neither regime dominates the electrochemical signal from the other.

3.3.2 Glucose detection

Having verified the occurrence of the electro-catalytic pathway for H_2O_2 generation, which was initially investigated for PEDOT applications as fuel cell electrolyzers, we now propose the following mechanism for its application for biosensing in our DN hydrogels. In mildly basic conditions (i.e., pH 7.4), the dissociation of H_2O_2 into peroxide and hydroxide ions alters the equilibrium of boronic-boronate acid, which serves as a hydroxide sink. The net reaction is:

$$O_2 + H_2O + 2\,e^- \rightleftharpoons HO_2^- + OH^- \tag{3.3}$$

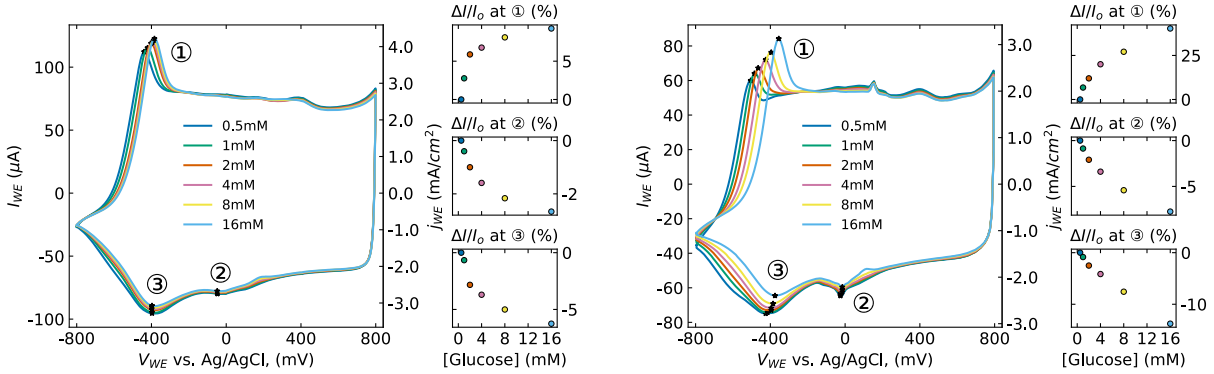

(a) PBA-0 (b) PBA-6

Figure 3.3: Cyclic voltammetry of DN hydrogels in 1× PBS with increasing [glucose], taken at a sweep rate of 50 mV/s. The final sweep in a series of 6 is shown. Auxiliary plots show the relative change of peak currents extracted from the redox features indicated.

At the same time, the peroxide ion may irreversibly oxidize PBA into phenol and boric acid; however, such degradation appears at odds to the stability observed in CV during kinetic testing. Rather, considering that the Pt CE is not blocked from the electrolyte, HO_2^- may be electrostatically repulsed from the hydrogel cathode and preferentially oxidized at the Pt anode instead, thus completing the mass transport circuit.

Therefore, consumption of the reduction products provides a forward driving force for ORR and increases reduction peak currents, since the PEDOT monomer units used as catalyst are oxidized while the elctrode is cathodically biased (i.e., regenerated by the power supply). Therefore, the presence of PBA moieties in proximity to reduced PEDOT lowers kinetic barriers for during oxidation into the H_2O_2-coordinated intermediate, thereby acting as a secondary dopant (cf. discussion in Section 2.2). In the presence of diols, the boronic acid-boronate ester equilibrium is shifted to toward the ester, reducing the ability of the second network to take up OH^- and decreasing the rate of ORR.

Cyclic voltammetry

To determine the electrochemical signal arising from the binding of glucose on PBA, we tracked the values of three redox peak currents during CV as shown in Fig. 3.3. According to the proposed mechanism, the electrochemical behaviour of peaks 1 and 3 must be considered in tandem, because the oxidation of PEDOT during ORR (peak 3) shifts the doping state of PEDOT and thus changes the amount of holes injected when the electrode is made anodic again (peak 1). Thus, an inverse relationship is seen in their peak currents, that is, as the additional reductive current decreases—corresponding to reduced PEDOT remaining reduced—the oxidative current increases after the cathodic turning point.

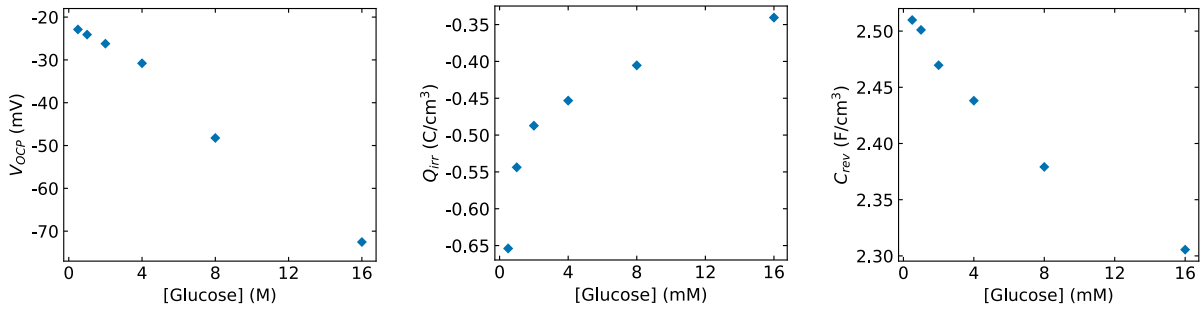

(a) OCP (b) irreversible charge (c) CSC

Figure 3.4: Additional quantities extracted during CV of PBA-6 hydrogel in 1 × PBS with increasing [glucose]. OCP was taken after reaching steady-state following a CV measurement. Irreversible charge and CSC were determined by integration of CV, following the methods in Section 2.2.2.

In the absence of PBA, the relative changes (i.e., $\Delta I/I_o \equiv \frac{I-I_{0.5}}{I_{0.5}}$) in peak currents of 1 and 3 with the addition of glucose is small (ca. 6 to 7 %) and track closely, as expected. In contrast, when glucose is added to the PBA-6 hydrogel, the behaviour of these peaks changes greatly, with a ca. 5 × increase of the signal from peak 1. At peak 3, the additional reductive current is suppressed with increasing [glucose], suggesting that the capacity for boronic acid to sink generated OH^- is reduced, on account of the equilibrium being shifted towards boronate-diol ester. Moreover, the ratio of the relative changes of peaks 1 and 3 in Fig. 3.3b is close to 2, corresponding with the stoichiometric ratio of electrons to product in Eq. (3.3). Finally, we note that behaviour of the peak current at 2 is qualitatively similar to peak 3, which may be related to the formation of intermediate.

Trends with [glucose] in other electrochemical quantities are presented in Fig. 3.4, such as an increasingly negative OCP measured after CV, similar to previous reports of glucose detection a PEDOT and PBA hydrogel electrode [105]. This was attributed to the accumulation of negative charge, as more boronate esters formed with additions of glucose. At the same time, irreversible charges (i.e., the remaining charge from the numerator of Eq. (2.5)) induced by CV decrease with [glucose], in agreement with the reduced rates of ORR as discussed previously. However, extracted CSC data contrast with the results of Ref. 105, who observed increasing capacitance due to significant swelling of 100 nm thin hydrogels and uptake of cations with charging of PBA. In our 100 µm thick hydrogels, the small (ca. 8 %) decrease in capacitance with [glucose] may be due to the orders of magnitude difference in thickness, or to the inclusion of PAMPS in our hydrogels, which already includes negatively charged sulfonate groups, thereby minimizing the relative change of capacitance due to changes in geometry or permittivity. It is also apparent by comparison of IS data that our hydrogels are dominated by bulk capacitance

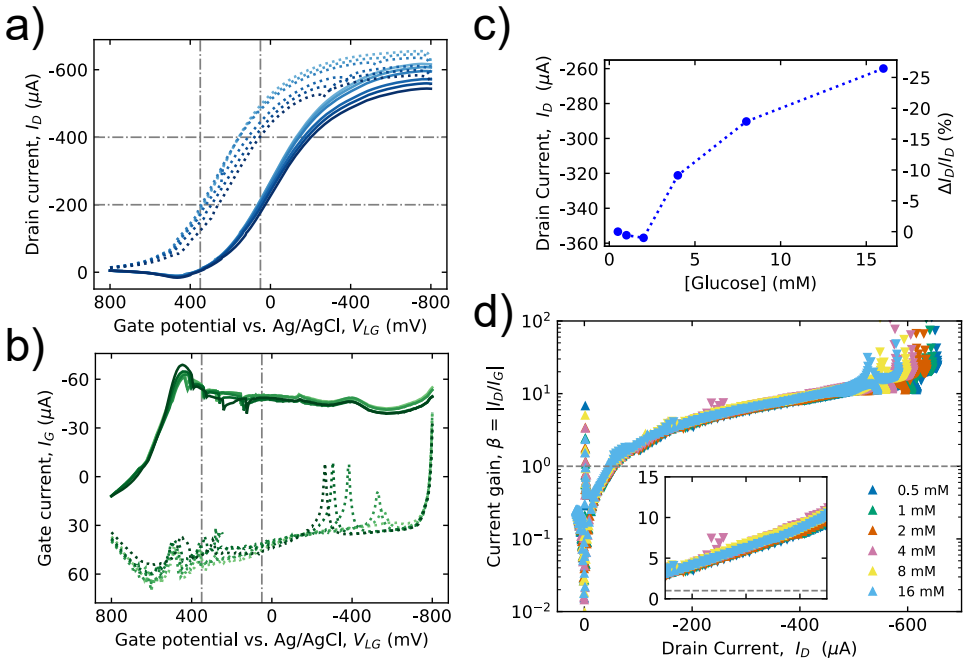

Figure 3.5: Transfer curves (a) and gate leakage (b) of a PBA-6 DN hydrogel in 1 × PBS with increasing [glucose]. OECT was operated at $V_{DS} = -10\,\text{mV}$, at a sweep rate of $27\,\text{mV/s}$. Darker shades indicate higher [glucose] and the last sweep of 6 cycles is shown. Drain currents (c) read out from the decreasing cathodic sweep at $V_{LG} = 200\,\text{mV}$ (the mid-point potential of the region enclosed by dashed lines in (a)). The calculated |current gain| (d) on a log scale, with the inset on a linear scale for the region of interest.

(i.e., Z at low frequency), whereas Ref. 105 is dominated by interfacial capacitance (Z at high frequency). This is consistent with their interpretation of a signal produced via swelling, whereas our signal is determined directly by a shift of electrochemical state.

OECT signal amplification

Having identified the origin of the electrochemical signal arising from glucose binding on PBA in our DN hydrogels, we repeated the sensing experiment with a new sample used as OECT channel. As previously discussed (cf. Section 2.3.3), the operation of OECTs at the smallest possible V_{DS} allows the applied gate potential to control electrochemical behaviour throughout the entirety of the channel. The corresponding transfer curves and gate voltammograms are shown in Fig. 3.5a,b. Although the gate voltammogram exhibits the expected capacitive behaviour in its box-shape, because I_G is measured at the CE, not all currents involving charge transfer with transported carriers in the channel will be counted. Namely, shifts of the PEDOT oxidation peak with [glucose] observed in Fig. 3.3 are absent, as holes are rather injected by the source electrode. However, because the mass transport circuit for re-oxidation of generated HO_2^- is completed by the Pt CE, a

similar decreasing trend in the reductive currents in the cathodic sweeps (i.e., when the CE is oxidizing to HO_2^-) is duly observed. Therefore, we analyzed the OECT output at the same operating regime ($dV_{LG}/dt > 0$).

At the same time, the gate voltammogram exhibits measurement artifacts related to the sensitivity of surface processes to the choice of steps in the staircase sweep of V_{LG} [144], or other stochastic events related to mass transport. This may account for part of the non-monotonicity observed when extracting currents at constant V_{LG} (Fig. 3.5c), and artificially limits the dynamic range of the measurement. Therefore, a region-of-interest (ROI) was identified in a regime of stable linear current gain ($\beta = |dI_D/dI_G|$) as shown in the inset of Fig. 3.5d. Here, the potential range of cathodic transfer curves passing through the ROI was ∼400 mV and its mid-point was used to extract $I_D(V_{LG} = 200\,\text{mV})$. Conveniently, this point also coincides with peak g_m in the cathodic transfer curves. Figure 3.5c shows the extracted I_D vs. [glucose] and its relative change is remarkably similar to that of PEDOT oxidation in glucose sensing CV, suggesting that it is indeed accounting for the additional hole current injected by the source and swept into the drain when PEDOT is oxidized during catalysis.

According to average $\beta \approx 6$ at this operating point, the magnitude of I_D is 6 × amplified compared to the measurement at the gate. Although the apparent limit of detection is still quite high at 2 mM, these results demonstrate a working proof-of-concept for the direct amplification of the electrochemical signal produced by the binding of diols on PBA incorporated in a hydrogel OECT channel. To further optimize the sensor response, the channel geometry or composition (i.e., fixed charge density) can be adjusted based on the rate-limiting step in the mechanism. That is, to ensure that the measured signal corresponds to the PBA equilibrium, electro-catalyzed ORR should not be rate-limited by diffusion of either O_2 in or HO_2^- out of the hydrogel. Ideally speaking, as the mass transport flows in a closed loop without conversion of the analyte, the evolved signal is a measure of the resistance towards driving ORR forward with externally supplied current. Therefore, we expect the device to be stable, because the activity of the catalyst (PEDOT) is thermodynamically and externally controlled. Simultaneously, we anticipate that the use of small signal (AC) measurements can be applied to exert additional control over the kinetic factors.

3.4 Conclusions

In this chapter, we investigated the kinetically controlled electro-catalytic behaviour of PEDOT in our DN hydrogels towards ORR as originally proposed by researchers working in

the development of fuel cells. This required device operation in cathodic potentials, which is a regime conventionally avoided in CP biosensors because of the possible deleterious effects of evolved hydroxyl radicals and H_2 gas from the use of aqueous media. However, our DN hydrogels demonstrate the requisite stability to operate in this regime, as evidenced in our sweep-rate controlled CV study.

We observed electrochemical signals corresponding to diol binding on PBA arising directly in the bulk of the channel, in contrast with previous work which was interface dominated. The mechanism we propose to explain this behaviour reveals that the PBA equilibrium is coupled to the activity of PEDOT during ORR due to the sinking of OH^- reaction products. Furthermore, because of the closed-loop in the mass transport of O_2 and produced H_2O_2, the device response is controlled by the regeneration of PEDOT catalyst via an external power source, thus forming a basis for kinetically controlled biosensing of glucose. On account of the species involved, this mechanism is highly reminiscent of the enzymatic action of glucose oxidase [145].

Finally, we demonstrate that the glucose signal arising directly within the bulk of the hydrogel is amplified in a transistor operation, with a signal gain of $\sim 6\times$. This result is significant because it offers a way around a limited frequency response in thick hydrogel devices used for ionic amplification. Further study on the optimal composition and operating conditions will be necessary to understand the limits of this approach—although the detection of [glucose] was made at the level found in blood, enhancing the lower limit by an order of magnitude is a pre-requisite for a shift towards non-invasive monitoring.

Chapter 4

Reversible resistance switching in PEDOT:PSS hydrogels

4.1 Background

In ion-permeable conjugated polymers, the electrochemical potential (i.e., Fermi level) is strongly coupled to applied gate potentials because of the ease of charge injection according to Eq. (1.1). When the solvent is non-aqueous (e.g., acetonitrile) and ions are non-interacting (e.g., tetrabutylammonium hexafluorophosphate), a large window into the electronic bandstructure is opened, making it possible to measure a characteristic non-monotonic conductivity [146] and probe the HOMO and LUMO levels of CPs electrochemically [121, 122, 128, 129, 147]. After Ref. 146, similar studies have been repeated with all manner of technolgically applied CPs, including PEDOT [148], polypyrrole [149], polydicarbazole [150]], and polythiophenes prized for diode heterostructures [131, 151, 152]. Notably, the role of potential-stable solvent and ion can be taken up simultaneously by the use of ionic liquids [131]. For the sake of illustration, simultaneous CV and conductance measurements for polyaniline and PEDOT are shown in Fig. 4.1.

The reason for non-monotonic conductance is thus attributed to the emptying of HOMO states at high potentials, leaving no free carriers available for transport—in other words, the transport band is fully occupied by holes. Depending on the electronic structure of the CP, this transition may be accompanied by both a decrease or increase of redox current (see Fig. 4.1), although both are described as "overoxidation". Reversibility (or the lack thereof) is observed to be dependent on both the largest potential reached and the time spent there, and has been exploited to produce so-called write once read many (WORM) memories [153, 154]. Reversible memristance has also been designed by leveraging interfacial dipoles [154] or coupling the gate to a ferroelectric material [155].

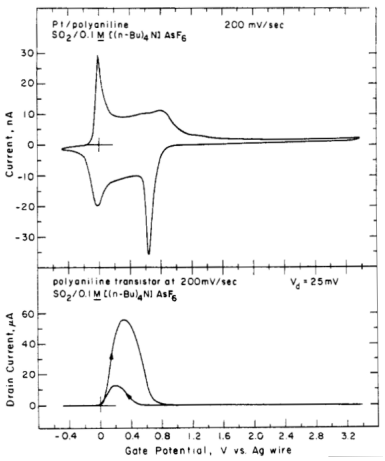

(a) polyaniline

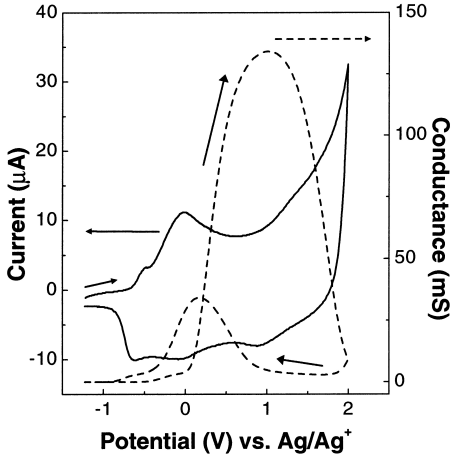

(b) PEDOT

Figure 4.1: Simultaneous cyclic voltammograms and conductance measurements taken in non-aqueous media for polyaniline (a) and PEDOT (b). Adapted with permission from [146] and [148]. Copyright 1990, 2000 American Chemical Society.

These previous descriptions of reversible resistance switching in CPs have in common large applied potentials in non-aqeuous/dry conditions because of the need to access electrochemical potentials beyond electrolysis of water. In contrast, to our best knowledge we have made the first observation of electrochemically controlled, reversible resistance switching at very low potentials (i.e., <1 V) during operation in aqueous media in our DN hydrogels. Our working hypothesis is that this phenomena arises due to the coupling of the electro-mechanical action of non-conductive polyelectrolytes (e.g. PAMPS) included in the hydrogel scaffold that works to disrupt the formation of polaronic bands required for electronic conduction in PEDOT. That is, a structural change that reduces the relaxation energy associated with a (bi)polaron, making it energetically unfavourable.

For instance, under the action of large electrolyzing electric fields[1], the structure of P(AMPS-*co*-AAm) hydrogels can contract and de-swell, serving as draw agents to move water in electro-osmotic applications [116, 156]. To a lesser degree, microscopic internal strains that arise due to electrophoresis of ions and accumulation in the polyelectrolyte gel leads to macroscale bending and electro-actuation applications [101, 157, 158]. While CP hydrogels are indeed expected to experience conformation changes and swelling during low potential operation as electrochemical devices [61, 113–115], the reversible switching effect we observe is remarkably drastic and complete. This is most likely due to the large electric fields in the space charge region formed when the contact and channel resistance are of similar magnitudes.

[1]Though it was not reported, a rough estimate using photographs provided by Ref. 116 suggests that a field of 0.5 V/mm is sufficient to induce de-swelling.

(a) as cleaned Au (b) SAM decorated Au

Figure 4.2: Static contact angles determined by a 2 µL drop of DI water.

4.2 Methods

Operation of DN hydrogel electrochemical electrodes and OECTs follows the procedures detailed in Section 2.2. Qualitatively, we found that hydrogels which had been thermo-mechanically annealed rarely displayed reversible switching. This hints towards a strong structure dependence of this effect and its possible occlusion from previous reports due to variation in procedures between groups. Accordingly, we formed an initial hypothesis that resistance of the contacts should be greater than the channel to adequately induce a space charge. Thus, Au electrodes were decorated with self-assembled monolayers (SAMs) of alkanethiols, which are expected to form insulating interfaces [159].

Prior to SAM formation, Au electrode substrates were cleaned by the same procedure described in Section 2.1, followed by a 15 min soak in base piranha (5:1:1 v/v of DI water:H_2O_2:30 % NH_4OH(aq)) at 80 °C. SAMs were prepared by incubating substrates in a 3 mM solution of 16-amino-1-hexadecanethiol (Dojindo) in a 97:3 v/v mixture of ethanol:NH_4OH(aq) for 1 h. A water contact angle of $43 \pm 5°$ ($N = 5$) was determined by the sessile drop method, shown in Fig. 4.2, and confirmed the presence of amines [160].

To prevent the detachment of DN hydrogels caused by stresses associated with large-scale conformation changes, coupling of the amine head group in the SAM to carboxyl groups included in the hydrogel by the azo initiator (cf. Section 2.1) was performed. First, carboxyl groups were activated by treating hydrogels for 15 min in a 20 mM solution of 1-ethyl-3-(3-dimethylaminopropyl) carbodiimide (EDC, Dojindo) in PBS. Subsequently, hydrogels were positioned on Au-SAM electrodes and coupling proceeded by amide bond formation overnight at 4 °C. To ensure removal of urea side-products released during amine coupling, bonded hydrogels were incubated for 2 h in PBS, with replacement by fresh solution at the 1 h mark.

4.3 Results and Discussion

4.3.1 Dependence on structure evolution in CV

Similar structural evolution was observed in CV of PBA-0 and PBA-6 hydrogels shown in Fig. 4.3. Following EDC coupling and incubation in PBS (top row), DN hydrogels present with CV characteristic of compacted CPs [115]. Calculated coulovoltammograms (not shown) exhibit characteristic shapes related to structural evolution in the CP with incomplete oxidation. Here, current density is small, with an apparent shift of the PEDOT oxidation peak to >600 and ∼200 mV for PBA-0 and PBA-6, respectively. This relationship agrees with previous discussions (cf. Section 2.2.2) and may be attributed to the secondary doping of PBA or more abundant negative charge in PBA-6.

By holding the electrodes at their OCP vs. Ag/AgCl for an additional 4 h (Fig. 4.3, middle row), the shape of CV returns to the pseudo-capacitive box-shape, except for a precipitous drop in current density at the anodic switching potential of 160 mV. In contrast to the overoxidation shown in Fig. 4.1, this change of electrochemical state appears sudden and rapid. It is likely that this transformation is non-adiabatic, and because de-swelling is accompanied by a decrease in conformational entropy, the process is also endothermic[2]. The required energy may be provided electrically, as evidenced by the small peak in current density immediately before the drop. Thus, the transition from low resistance to high resistance is irreversible, until sufficiently cathodic potentials are applied ($V_{WE} < 0\,\mathrm{V}$) to reduce accumulated oxidized PEDOT monomers. The fact that corresponding reduction peaks appear larger in PBA-0 hydrogels may be due to a smaller amount of anionic charge in the second network to balance oxidized PEDOT, resulting in more reduction occurring.

It is also apparent that strains associated with repeated structural and charge relaxation that accompanies resistance switching are not completely mitigated by EDC coupling, as the PBA-6 hydrogel exhibits contact instability as indicated by the shifting of oxidation potential (cf. discussion in Section 2.2). After a dry, storage, and re-swell cycle (Fig. 4.3, bottom row), the contacts improved. Although resistance switching is still observed, the extremely minimized current density in the high resistance state is increased (cf. middle row CVs). This suggests that the hydrogel micro-structure was altered by the drying cycle and became more porous to ions. At the same time, the reduction peak in PBA-0 is reduced to similar current densities as in PBA-6 in both conditions. A possible explanation for this is that increased ion permemability allows solvated anions to compensate charges from oxidized PEDOT before restoration of polaronic states.

[2]That is, energy is required balance the relaxation energy released in the formation of a polaron.

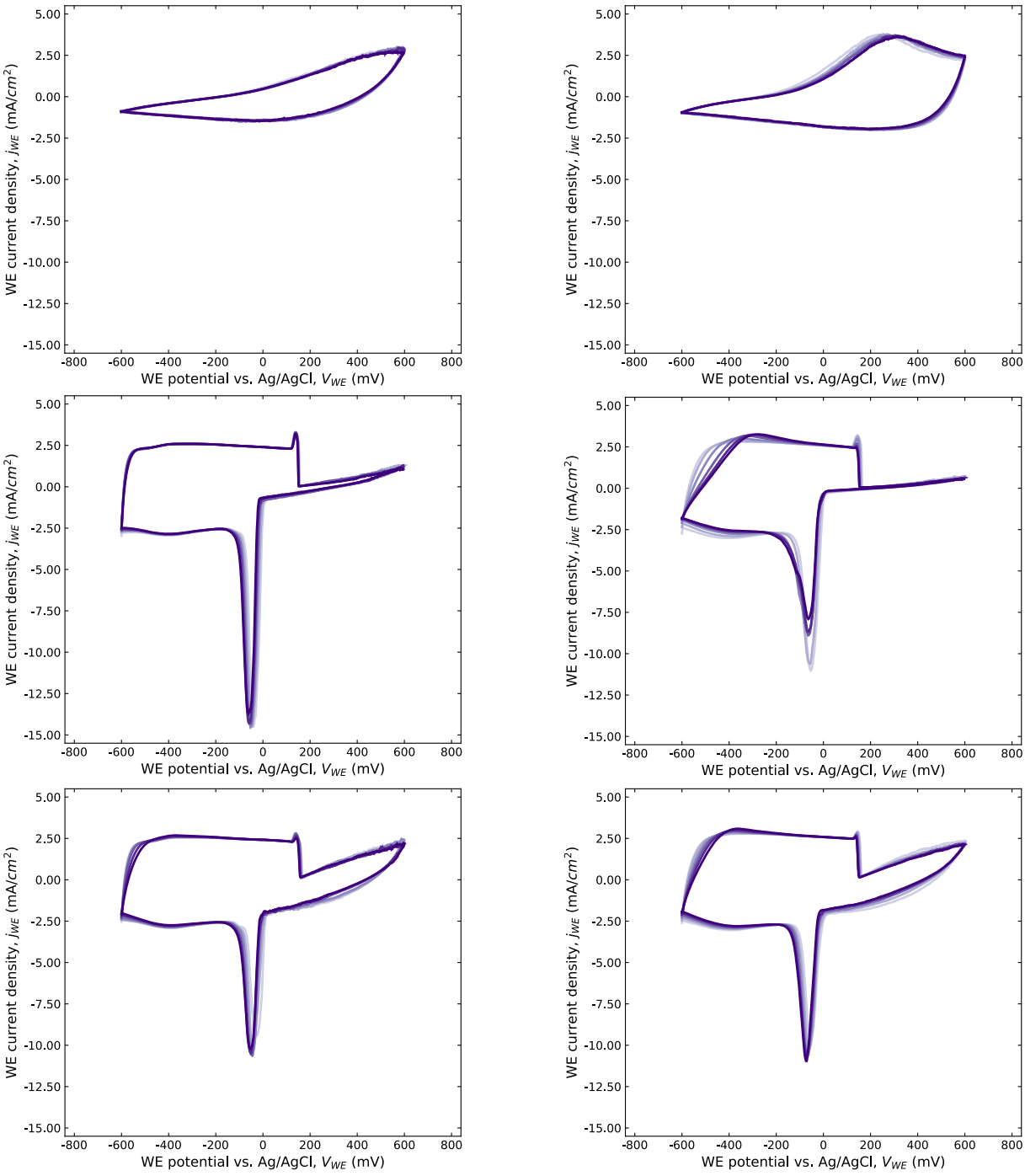

(a) PBA-0

(b) PBA-6

Figure 4.3: Evolution of cyclic voltammograms of DN hydrogels in 1 × PBS, following EDC treatment on SAM-decorated Au electrodes. Data were collected at a sweep rate of 50 mV/s for 6 cycles, with later cycles appearing in darker shades. Conditions (top to bottom): following EDC-coupling, after OCP measurement for 4 h, and after a dry/re-swell cycle.

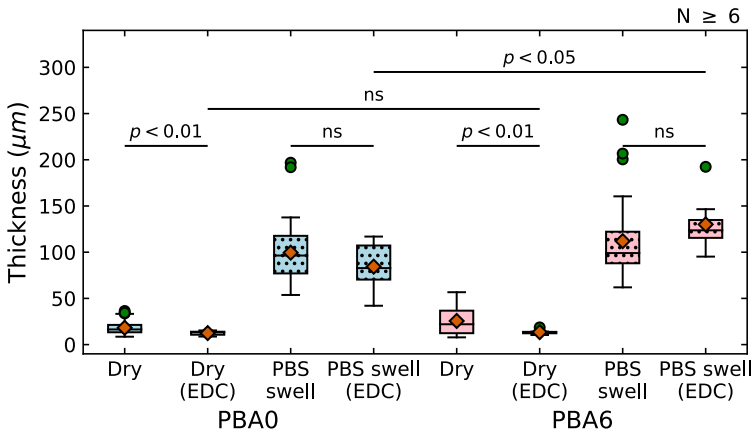

Figure 4.4: Comparison of thickness of PEDOT hydrogels with 0 and 6 mol% PBA in the dry state or swollen in PBS as in Fig. 2.6, after treatment with EDC. Statistical significance between pairs of untreated/EDC treated datasets is determined by unequal variances (Welch's) t-test.

4.3.2 Changes in hydrogel thickness

Following the final set of CV measurements, thickness and swelling data of DN hydrogels were collected as presented in Fig. 4.4. In the dry state, EDC treated hydrogels are more compacted than their untreated counterparts, although this difference does not appear statistically significant upon swelling. Note that the swollen thickness is measured after the structure evolution discussed in the previous section, so the initial compaction may not be accurately reflected. The presence of PBA appears to also increase swelling in treated films, albeit at a lower significance level than the previous comparisons.

4.3.3 Observations in OECT characteristics

Although the prevalence of resistance switching in hydrogels grafted on to Au-SAM supports our initial hypothesis about the required ratio of contact to channel resistance, exceptionally high conductivity hydrogels with good bond quality can still exhibit resistance switching without modification. Figure 4.5a,c presents transfer and output curves of such a PBA-0 hydrogel sample. In both curves, box-shaped hysteresis is apparent with a rapid decrease in conductance when $V_{LG} < -200\,\mathrm{mV}$. Once in this high resistance state, returning to $V_{LG} \sim 0\,\mathrm{V}$ restores the low resistance state and OECT operation. In the output curves, this order is reversed because the local electrode potential moves towards $0\,\mathrm{V}$ when V_{DS} is increased.

Rapid switching between resistance states results in a non-monotonic transfer curve, for which large negative transconductance peaks are observed in Fig. 4.5b. The ratio of

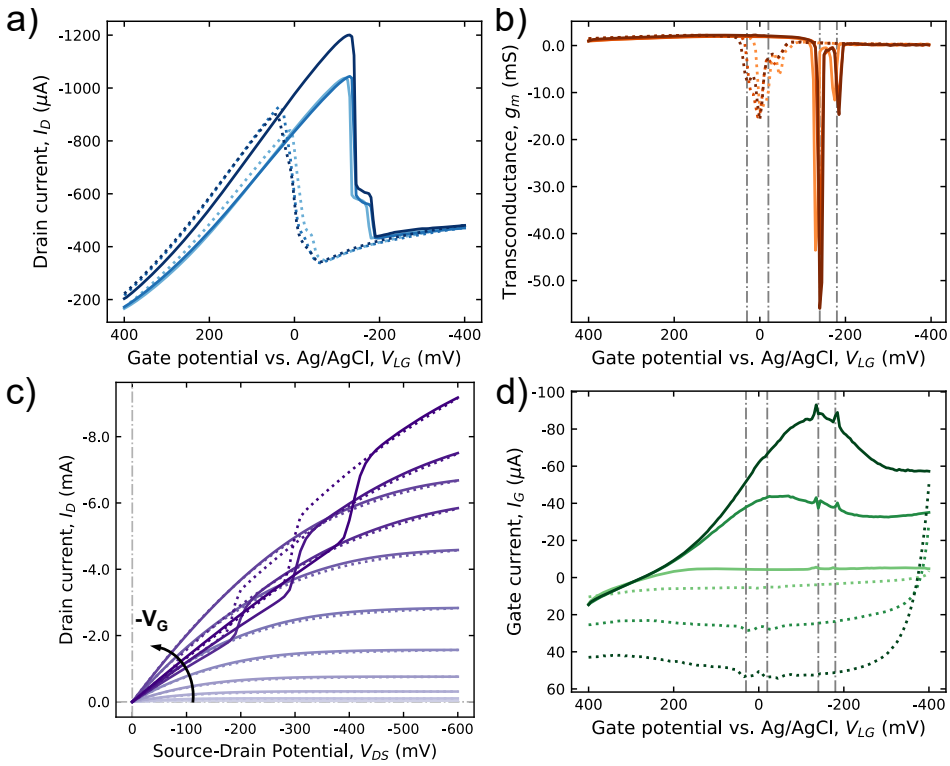

Figure 4.5: Transfer (a) and output (c) curve of a PBA-0 DN hydrogel OECT in 1 × PBS. Transconductance (b) and gate leakage (d) taken during (a), with $V_{DS} = -50\,\text{mV}$ and dV_{LG}/dt set as 4.7, 30, to 60 mV/s (light to dark lines). Dashed lines serve a guide to the eye. In (c), V_{LG} varied from 600 to $-400\,\text{mV}$ light to dark). Resistance switching occurred for $V_{LG} < -200\,\text{mV}$.

peak g_m is ca. -20 and $-7\times$ compared to peak g_m of 2 mS prior to switching for the high-to-low and low-to-high transition, respectively. The peak positions in voltage align with the oxidation and reduction peaks at ca. -160 and 0 mV in the gate current (Fig. 4.5d), respectively, and are in excellent agreement with the switching potentials observed in CV. Both the redox couples and transconductance peaks appear as doublets, with a separation of ∼50 mV corresponding to the magnitude of V_{DS}. When V_{DS} is small, the step in I_D during the transition disappears, and for large V_{DS} the current in the high resistance state remains large. Moreover, constant peak positions with increasing scan rates from 4.7 to 60 mV/s indicate that the reaction is not kinetically limited.

The fact that reversible, box-shaped hysteresis loops are observed in both transfer and output curves indicates that this switching is not due to the disconnection of hydrogel at source or drain electrodes, but rather a change in the nature of electronic transport. Moreover, output remains ohmic, even when the measurement begins with the channel in the high-resistance state. Interestingly, an abrupt change in the gate current is not observed as in CV, while residual current in the high-resistance remains large. This suggests that

the disruption of electronic transport is not complete in this example. Therefore, mapping of the density of states near the HOMO edge while the hydrogel operates in aqueous media will be required to further elucidate this switching phenomena.

4.4 Conclusions

In this chapter, we made the first observations of an electrochemically controlled, reversible resistance switching occurring in our highly conductive DN hydrogels. We hypothesized that this phenomena arises due to the electro-mechanical interaction of the second network, which contains acrylamides with sulfonic acid known to alter conformation with ionic activity. From characterization of electrochemical electrodes and OECTs, we identified a likely physical origin, which is the disruption of polaronic bands for electronic transport. A key trigger is the formation of space charge in the hydrogel, which occurs when contact resistance is greater than a low channel resistance.

While the use of a SAM on Au brought about this condition, other factors such as the workfunction of the electrode, the density of fixed charges in the hydrogel, and the degree of cross-linking must be further explored to build up the requisite foundation for engineering of this switching effect. There is significant potential here for the design of advanced electrical functions in hydrogels applied as biosensors and bioelectronic interfaces, because the electrochemical potentials involved in switching are readily accessible in aqueous media and physiological conditions.

Chapter 5

Conclusions and Outlook

In this thesis, we demonstrated a simple method for the fabrication of highly conductive IPN hydrogels composed of PEDOT:PSS and a second network based on P(AAMm-*co*-AMPS). Despite a high 1:1 loading of non-conductive acrylamide polymers, these CP hydrogels maintain the high electrical transport properties of PEDOT:PSS, which is thanks to the fact that hole mobility is not impeded because of good compatibility between PEDOT and the hydrogel scaffold by the inclusion of sulfonic acid moieties in AMPS. We also developed a simple method to form reliable ohmic contacts to hydrogels in wet media.

We have also investigated the influence of co-polymerization with AAPBA on the electrochemical properties of PEDOT. This is predominant when the material is operated in cathodic potentials, which has conventionally been kept outside the scope of biosensing applications due to stability concerns. However, from our exceptionally performing materials, we were able to identify a sensing mechanism based on the electrocatalytic activity of PEDOT for the oxygen reduction reaction, which is coupled to the equilibrium of boronic acid and boronate-diol esters such as glucose. These functionalized CP hydrogels thus generate an electrochemical signal within their bulk that can be directly detected and amplified in the channel of a single OECT.

Simultaneously, we observed electrochemically controlled resistance switching effect at very low potentials in some of the samples prepared in this work. This was attributed to the electro-mechanical coupling of the polyelectrolytic nature of AMPS with the formation of electronic band structure in PEDOT. The trigger for this effect was identified as the accumulation of ions in the channel, and could be controlled by altering the contact resistance. To do this, we demonstrated that a self-assembled monolayer of alkanethiols on Au is effective. The output of such devices demonstrate reversible box-shaped hysteresis loops, which are promising for the development of novel bioelectronic devices.

Outlook

Though we have demonstrated interesting results with DN hydrogels by our simple fabrication method, a more thorough excursion into the monomer composition space will be useful to clarify the properties that each component affects. For instance, it may be possible to include acrylamides with different affinities to form molecularly imprinted binding sites [135]. Alternatively, other bio-functions such as mitigation of non-specific binding (i.e., bio-fouling) may be achievable by including zwitterionic (acrylamide) monomers [161]. Finally, tuning of the mechanisms discussed here will most likely involve the adjustment of the sign and density of fixed charges in the second network.

At the same time, apart from composition, the processing techniques used here may still be optimized, for instance, by inclusion of conductivity enhancers or solvent based post-treatments. Importantly, a mechanical approach to quantify the improvement of bond strengths by the simple thermo-mechanical annealing used here will be necessary to understand the factors to increase device-to-device reliability. Moreover, the electrochemical probing of electronic structure (i.e., HOMO and defect states) in aqueous media will be required to build foundational knowledge for the design of electrochemically active binding sites and biosensing application.

Finally, we envisage that these free-standing, highly conductive hydrogels, which can be readily electrochemically functionalized, will contribute to an emerging class of soft, structural bioelectronic devices, such as biomolecularly controlled memory cells, negative transconductance amplifiers, neural interfaces, bio-actuators, and neuromorphic devices.

Appendices

Appendix A

Thin-film PEDOT:PSS OECTs

A.1 Background

As discussed in Chapter 1, a significant reason for the popularity of PEDOT:PSS as a CP for technological applications is the ease afforded by solution-based processing. Along with this popularity, substantial work has been performed on optimization of its thin-film properties [25]. Accordingly, most studies of PEDOT:PSS devices involving operation in aqueous media are prepared from a mixture of aqueous PEDOT:PSS solution with high boiling point organic co-solvents, a surfactant to enhance reorganization of polyelectrolyte, and a cross-linker to stabilize against dissolution. The most popular formulation being ethylene glycol as the co-solvent [27], 2-dodecylbezenesulfonic acid (DBSA) as the surfactant [162], and (3-glycidoxypropyl)trimethoxysilane (GOPS) as cross-linker [163, 164]. This is typically followed by filtration (ca. 0.5 µm) to remove large aggregates of PEDOT:PSS prior to spin-coating of thin-films.

Due to the heavy optimization of this formula towards high electrical conductivity, OECTs prepared from this material exhibit high performance as ionic amplifiers [70]. The trade-off is that it becomes difficult to incorporate additional biological or chemical function (e.g., for sensing) without also degrading the electrical performance. For example, in PEDOT:PSS films composited with poly(vinyl alcohol) (PVA) to increase the availability of hydroxyl groups for subsequent grafting of aminated biomolecules and proteins via the epoxide of GOPS as a linkage [165]. While alternative cross-linkers, such as poly(ethylene glycol) diglycidyl ether (PEDGE) [166], have been investigated that directly incorporate epoxide groups into the thin-film to simultaneously stabilize the swelled structure and improve cell adhesion and biocompatibility of PEDOT:PSS, these chemical components must be applied during the fabrication process, requiring each new variation to be compatible with the existing process.

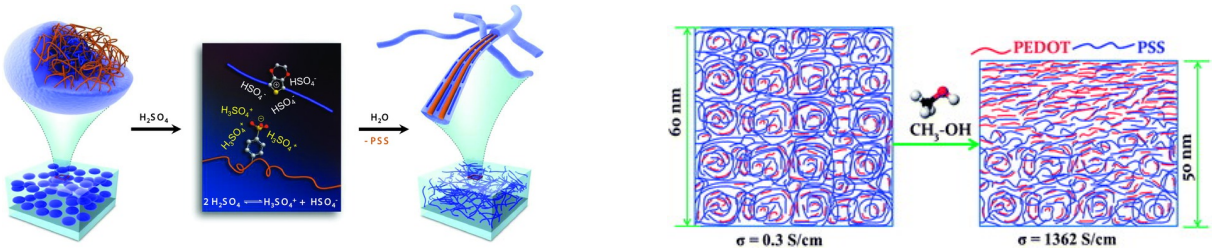

(a) H_2SO_4 (b) methanol

Figure A.1: Post-fabrication enhancement of PEDOT:PSS thin-film conductivity by application of (a) concentrated H_2SO_4 to remove excess PSS, and (b) methanol to facilitate enrichment of PEDOT content. Adapted with permission from [36] and [14]. Copyright 2014 John Wiley and Sons, and 2012 Royal Society of Chemistry, respectively.

In this regard, means of enhancing electrical performance after device fabrication, such as the re-crystallization of PEDOT by removing excess PSS with H_2SO_4 [26, 36], or re-distribution of non-conductive PSS-rich phases by soaking in methanol [14] as shown in Fig. A.1 are interesting as it enables a focus on designing the sensing function first. Therefore, we began the work for this thesis by investigating PEDOT:PSS thin-films made from neat PEDOT:PSS solution[1], without applied optimization strategies.

A.2 Methods

A.2.1 Fabrication of thin-film devices

Au/Cr electrode structures were defined by photolithography and RF sputtering as shown schematically in Fig. A.2. To produce the van der Pauw and four-point measurement motifs, a photomask was designed using computer-aided design software and commissioned (Kyodo International Inc.). Before photolithography, glass substrates cleaned by sonication in acetone, methanol, and DI water for 5 min each and dried with flowing N_2. Thereafter, the substrates were masked using OFPR photoresist (Tokyo Ohka Kogyo Co. Ltd.) deposited by spin-coating at 3000 rpm for 30 s and pre-cured at 120 °C for 5 min. A mask aligner (Quintel Q-2001 CT) was used to position the glass substrates for an exposure time of 30 s. Following this, patterned substrates were post-baked at the same conditions as for the pre-bake, then developed for 60 s in NMD-3 developer (Tokyo Ohka Kogyo Co. Ltd.), and finally rinsed in DI water and dried with N_2. RF sputtering (ULVAC, Inc.) using Ar plasma was performed at a power of 100 W. Acetone was used for lift-off after electrode deposition.

[1]Note that Orgacon™ ICP 1050 was selected because it is marketed as being surfactant-free.

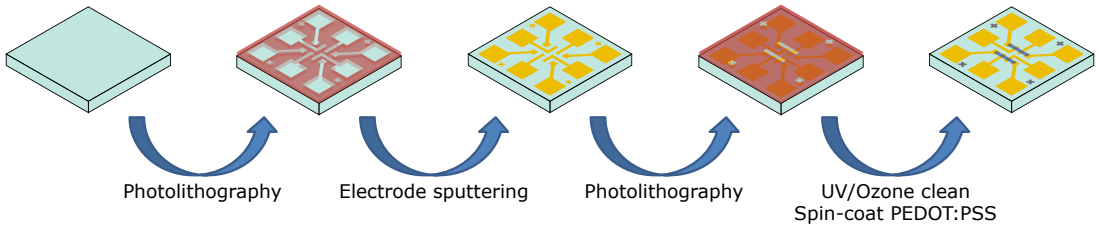

Figure A.2: Preparation of PEDOT:PSS thin-film OECTs using a photolithographic process. Typically, a glass substrate was used with OFPR photoresist (coloured red).

(a) van der Pauw (b) four-point

Figure A.3: Photographs of thin-film PEDOT:PSS devices. Dashed lines indicate the area containing PEDOT:PSS, which is highly transparent as a thin-film. Annotations indicate the electrical connections for applied potential and ammeter readings to determine sheet resistance.

To define the thin-film area, the same photolithography steps as above were repeated with the complementary pattern. Prior to spin-coating of PEDOT:PSS, patterned substrates were cleaned by exposure to UV/ozone for 10 min, which improved wetting and adhesion of the PEDOT:PSS layer. Spin-coating of PEDOT:PSS (Orgacon™ ICP 1050, Sigma-Aldrich) without filtration[2] and without additives was performed at 500 rpm for 5 s, then 3000 rpm for 30 s. The wet film was dried in a vacuum oven at 120 °C for 1 h, and lift-off of unused PEDOT:PSS film area was achieved by soaking in methanol for 1 to 10 min and mechanical agitation. Longer soaking times gave thin-films with higher conductivity, in agreement with Ref. 14.

Device substrates were subsequently rinsed with DI water, dried, and stored in air for characterization. Figure A.3 shows photographs of typical devices for van der Pauw and four-point resistance measurements. For devices measured in solution, a short section of glass tubing was affixed to the substrate by poly(dimethylsiloxane) (PDMS), prepared in a ratio of 10:1 resin to curing agent (Dow Corning Sylgard 184) and cured at 120 °C for 1 h under vacuum.

[2]We observed significant clogging of 0.45 µm syringe filters typically used for this purpose.

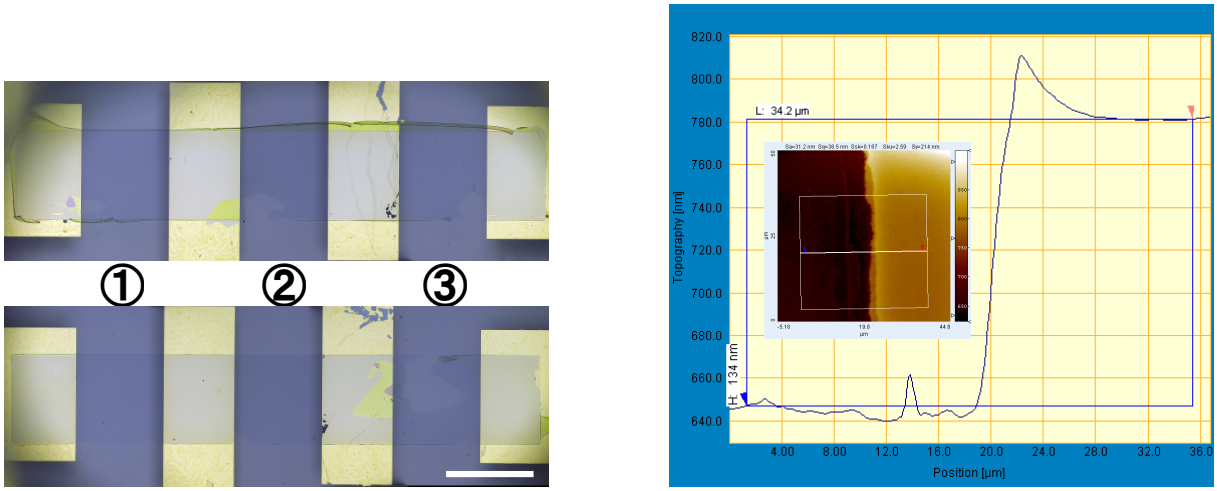

(a) stitched optical micrograph

(b) atomic force micrograph (inset)

Figure A.4: Micrographs of thin-film PEDOT:PSS devices. In (a), annotated numbers indicate the three junctions formed by current-forcing and potential-sensing electrodes. Scale bar is 1000 µm. In (b), the height profile obtained by averaging over an area in the micrograph. Inset of (b) shows the raw data and area used.

A.3 Results and Discussion

A.3.1 Determining thin-film conductivity

When patterning thin-films of PEDOT:PSS, a physical lift-off process using a sacrificial layer of parylene C is typically used, which avoids exposure of the CP to organic solvents or bases used to remove photoresist [53]. However, in this study, access to physical vapor deposition of parylenes was not available and thus necessitated the consideration of chemical changes to the PEDOT:PSS film during typical lithographic processing.

Indeed, in the earliest devices fabricated for this study, time spent in methanol for lift-off was minimized to ca. 1 min. This produced devices with low electrical conductivity, ca. 2 to 7 S/cm, as expected for neat PEDOT:PSS solutions without additives. Such thin-films were used for the measurement of pH sensitivity in Section A.3.3. However, by simply increasing the treatment time in methanol, it is possible to drastically enhance the electrical conductivity [14]. Considering it is rather difficult to reproducibly limit the exposure of PEDOT:PSS to methanol while ensuring complete lift-off[3], this realization comes as a benefit to our process. For illustration, Fig. A.4 shows optical and atomic force micrographs of representative thin-film devices.

[3]PEDOT:PSS thin-films exhibit flagging (i.e., partial connection to lifted portions) in some regions during lift-off in methanol, requiring *careful* mechanical agitation to completely break free.

Sheet resistance

Sheet resistances (R_S) were determined from van der Pauw and four-point measurements of PEDOT:PSS thin-films as described in Section 2.2. While R_S may be estimated from four-point measurements by fitting to a transmission line model or by direct comparison with the two-point resistance, by measuring additional combinations of parallel resistances, enough for two unknowns at each junction[4], it is possible to estimate the contact resistances and extract the R_{Si} of individual junctions formed between electrode probes in the four-point configuration. To do this, minimize the sum-of-squares error of the following non-linear system of equations:

$$\begin{aligned}
R_{1-2} &= (R_{S1} + R_{S2})L^* + 2(R_{C1} + R_{C2}) \\
R_{2-3} &= (R_{S2} + R_{S3})L^* + 2(R_{C2} + R_{C3}) \\
R_{1-2-3} &= (R_{S1} + R_{S2} + R_{S3})L^* + 2(R_{C1} + R_{C2} + R_{C3}) \\
R_{1|2} &= \frac{R_{S1}R_{S2}(L^{*2} + L^*L^*_{T1} + L^*L^*_{T2} + L^*_{T1}L^*_{T2})}{R_{S1}(L^* + L^*_{T1}) + R_{S2}(L^* + L^*_{T2})} + \frac{(R_{S1} + R_{S2})(L^*_{T1} + L^*_{T2})}{4} \\
R_{2|3} &= \frac{R_{S2}R_{S3}(L^{*2} + L^*L^*_{T2} + L^*L^*_{T3} + L^*_{T2}L^*_{T3})}{R_{S2}(L^* + L^*_{T2}) + R_{S3}(L^* + L^*_{T3})} + \frac{(R_{S2} + R_{S3})(L^*_{T2} + L^*_{T3})}{4} \\
R_{1|3} &= \frac{R_{S1}R_{S3}(L^{*2} + L^*L^*_{T1} + 2L^*L^*_{T2} + 4L^*_{T1}L^*_{T3})}{R_{S1}(L^* + L^*_{T1}) + R_{S2}(L^* + L^*_{T3})}
\end{aligned} \tag{A.1}$$

where - and | denote series and parallel connections of i-th junctions, respectively. The associated contact resistance is $R_{Ci} = R_{Si}L^*_{Ti}$ for a contact length of L^*_{Ti}, giving a measured resistance of $R_i = R_{Si}(L^* + 2L^*_{Ti})$ for a junction. Note that it is assumed that the aspect ratio of each channel is the same (i.e., $L^* = L/W$), which may not be true if channels contain defects[5]. Accordingly, such outliers are excluded from the sample dataset, shown in Fig. A.5a, which includes the regressed and directly calculated R_S values from the aforementioned treatment of four-point measurements.

Thin-film thickness

Thickness (t) measurements were sampled from PEDOT:PSS thin-films in the dry state using an Agilent 5500 scanning probe microscope in tapping mode. Typically, the probe was scanned over an area of $50 \times 50\,\mu m$ with a resolution of 512 points/µm and a rate of 0.5 lines/s. To collect correlated R_S and t data, the measurement sampled the same devices used for electrical characterization, with four sampling spots in van der Pauw geometries

[4]This is made possible by the asymmetry of the 1|3 connection, because the probes of junction 2 are used to bridge the connection.

[5]See also the lower third channel depicted in Fig. A.4a.

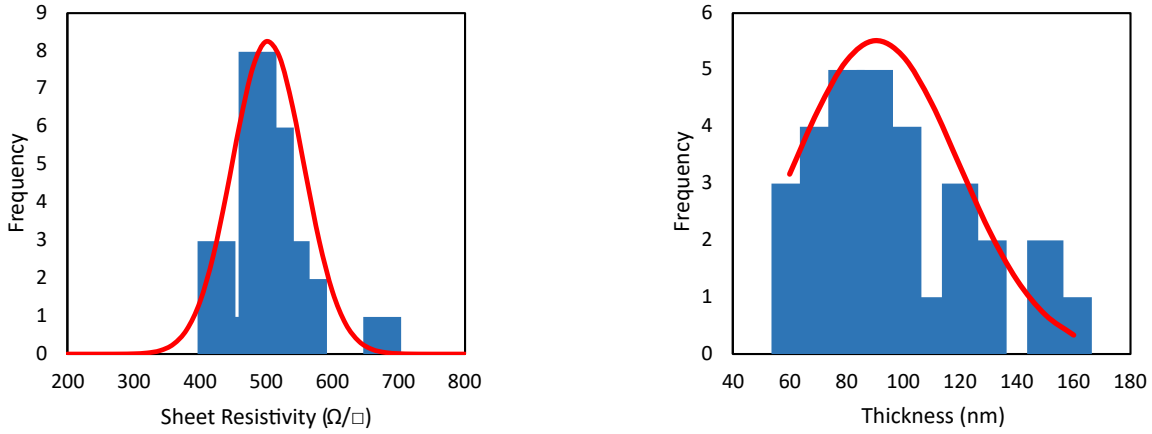

(a) (b)

Figure A.5: Sample distributions of PEDOT:PSS thin-films ($N = 9$). (a) Sheet resistivity determined by van der Pauw and transmission line measurements (bin size: $25\,\Omega/\square$). (b) Thickness determined by AFM (bin size: 10 nm). Red lines show fits to a normal distribution to extract statistical parameters.

(i.e., once per edge) and three sampling spots for four-point geometries (i.e., once per channel edge). After tilt correction, the height profile was averaged over a suitably large area and the thickness was read off by comparing the values across the step change. An example of the data is shown in Fig. A.4b, and the distribution is given in Fig. A.5b. In the absence of R_S data, these samples represent the repeatability of lithographic processing and uniformity of the film.

Specific electrical conductivity

Qualitatively, good fits to a normal distribution is observed in the sample data shown in Fig. A.5. The R_S data has a mean and sample standard deviation of $503 \pm 54\,\Omega/\square$, whereas this is 96 ± 29 nm for the t data. Assuming that R_S and t are independent variables, which is reasonable by the definition of R_S, propagation of uncertainty gives a value for the specific electrical conductivity, $\sigma = (R_S \cdot t)^{-1}$, as 208 ± 67 S/cm. However, as we have the full dataset, the covariance and correlation between R_S and t in this experiment may be estimated by taking [167]:

$$\begin{aligned} S_{\text{indep}} &\approx |\hat{x}| \sqrt{\left(\frac{S_{R_s}}{\hat{x}_{R_s}}\right)^2 + \left(\frac{S_t}{\hat{x}_t}\right)^2} \\ S_{\text{corr}} &\approx |\hat{x}| \sqrt{\left(\frac{S_{R_s}}{\hat{x}_{R_s}}\right)^2 + \left(\frac{S_t}{\hat{x}_t}\right)^2 + 2\frac{S_{\text{cov}}}{\hat{x}_{R_s}\hat{x}_t}} \end{aligned} \tag{A.2}$$

where $\hat{x}$ and S are the mean and standard deviation of the independent or correlated σ, R_S, or t, respectively. The covariance, S_{cov}, can be estimated from the data by assuming the underlying distributions in the correlated samples are unchanged from the independent ones. The distribution of σ when each datum is tracked with the corresponding device gives $207 \pm 47\,\text{S/cm}$. Applying Eq. (A.2) thus gives a covariance of $1250\,\text{nm}\,\Omega/\square$ and corresponds to a correlation, $\rho = S_{\text{cov}}/(S_{R_s} S_t)$, of 0.8.

This positive valued correlation is surprisingly large, considering the initial assumption of no correlation and seems to indicate that R_S increases with thickness. This may be due to the effect of increased variation, structural disorder, or additional contact resistances in spin-coated films that are thicker (i.e., less uniformly coated). In terms of the uncertainty, excluding the corresponding device information increases its value by ca. 40 %. Therefore, statistical descriptions of device performance should include this correlation whenever it is feasible.

A.3.2 OECT characterization and operation

In the dry state, our PEDOT:PSS thin films exhibit σ of ca. 200 S/cm, which is exceptionally high considering the lack of performance enhancing additives, although we note the incidental methanol treatment performed here did not improve σ to the degree reported by Ref. 14 (cf. 1000 ×). Regardless, they are sufficiently conductive and, most importantly, retain their structure in aqueous media without additional cross-linker which allows them to be operated as OECTs, according to the methods described in Section 2.1. Figure A.7 shows the characteristic curves in PBS (pH 7.4) for a representative OECT formed from a junction in the four-point structure (Fig. A.4a).

Comparison of polarizable and non-polarizable gate electrodes

At this point, it is helpful to illustrate the difference in control over the OECT channel conductance between a polarizable (e.g., Au or Pt) and non-polarizable electrode (e.g., Ag/AgCl) used as the gate. Figure A.6 shows three sets of output curves (I_D vs. V_{DS}) collected using: Ag/AgCl in saturated KCl connected over a salt bridge, an adjacent Au electrode, or both in a reference/counter electrode connection.

It is obvious that gating with the non-polarizable electrode is improved, with the OECT output displaying the saturation behaviour expected when the drain is depleted (i.e. pinch-off) [49]. This is because the Ag/AgCl electrode is able to efficiently inject cations into the bulk of PEDOT:PSS, or in other words, more of the applied potential drops at the electrical double layer interface at CP chains [79]. On the other hand, in the polarizable electrode, a larger impedance at the gate (i.e., electrode capacitance is small)

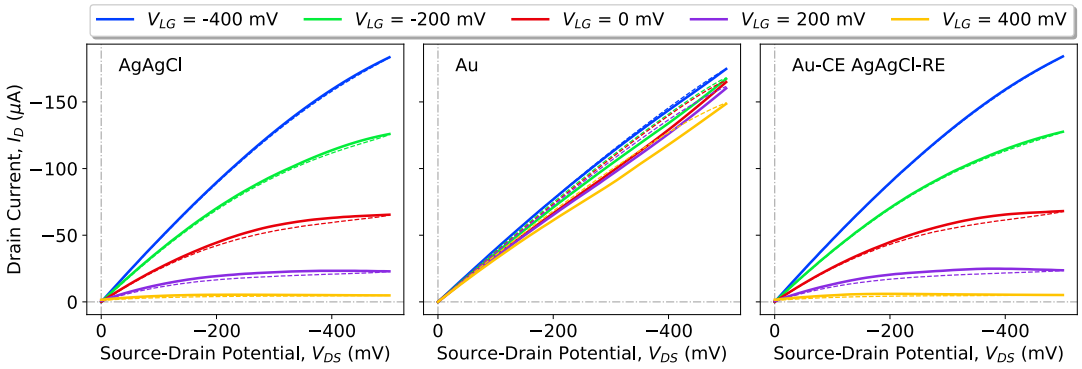

Figure A.6: Output curves taken in PBS (pH 7.4) at an average $dV_{DS}/dt = 60\,\text{mV/s}$, collected using Ag/AgCl in saturated KCl connected over a salt bridge, an adjacent Au electrode, or both in a reference/counter electrode connection. Dashed lines represent the second half of cyclic sweeps of V_{DS}.

shifts the potential drop away from the OECT channel according to the voltage divider of the ionic circuit. This is the reason that OECT studies typically use Ag/AgCl as a pseudo-reference electrode, or otherwise coat metal electrodes with CP to increase surface area. When a proper thermodynamic reference and counter electrode arrangement is used, the sensing of potential between reference and OECT source electrodes requires that the same current be injected through the counter electrode as for the case of direct gating with a pseudo-reference.

Characterization in saturation regime

Transfer characteristics (I vs. V_{LG}, Fig. A.7d) typical of a p-type semiconductor are observed, with appreciable current at $V_{LG} = 0\,\text{V}$ indicative of depletion mode operation. A slight hysteresis is observed in cyclic sweeps, which may be attributed to capacitive charging of the channel due to the region near the drain contact being depleted of carriers ($V_D = -400\,\text{mV}$ and $V_S = 0\,\text{V}$). Simultaneous measurements of source and gate leakage currents (Fig. A.7e, f) corroborate this view, with the source current exhibiting less hysteresis. However, an obvious redox couple can be observed in the source and gate currents, indicating the presence of an electrochemical side reaction localized at the source electrode. Considering its potential relative to Ag/AgCl, this peak current may possibly be due to the leakage of Ag^+ into the electrolyte [168, 169]. Regardless, we can exploit this to gain insight into our system and realize that charge is conserved in the three-terminal electrochemical cell, i.e. $I_D + I_S + I_G = 0$, as seen in the inset of Fig. A.7e.

In this case, because redox current is localized to the source when the OECT is in saturation, i.e. $V_D < V_G - V_p$, readings of the OECT output at the drain are not

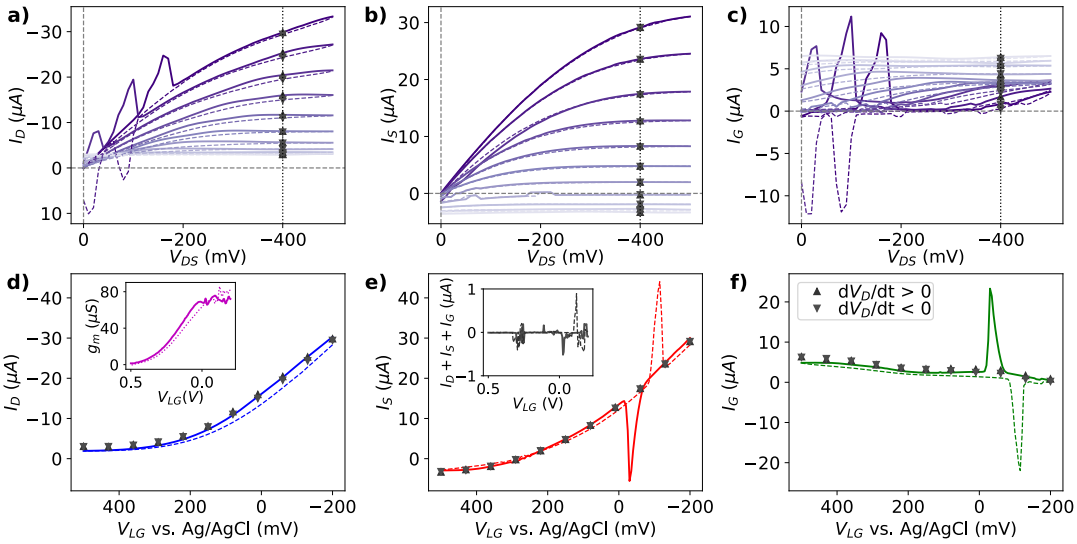

Figure A.7: Steady-state output (a, b, c) and transfer (d, e, f) curves of a representative PEDOT:PSS thin-film OECT. Drain, I_D, (a, d); source, I_S, (b, e); and gate, I_G, (c, f) currents are simultaneously measured, to confirm the conservation of charge in the electrochemical cell. Output curves were taken at $dV_{DS}/dt = 8\,\mathrm{mV/s}$ for V_{LG} ranging from -200 to $500\,\mathrm{mV}$, with accumulating V_{LG} in darker shades. Dotted lines and markers show the slice at $V_{DS} = -400\,\mathrm{mV}$ to extract the steady-state transfer curve for comparison in (d, e, f). Transfer curves were taken at $dV_{LG}/dt = 4\,\mathrm{mV/s}$ at the same V_{DS} in saturation. Insets: (d) shows the transconductance, g_m, by numerical differentiation; (e) shows the sum of electrode currents. In all subfigures, solid lines with heavier weights represent the first half of a cyclic sweep of the independent variable.

significantly affected, although fluctuations in g_m can be observed at the corresponding redox potentials [83]. Additionally, when the whole channel is depleted at $V_G < V_p$, both drain and source sink the cathodic current, becoming negative in proportion with current injected from the gate [55]. Note that V_p for this device was determined to be 469 to 517 mV by extrapolation of $\sqrt{I_D}$ (see also Eq. (1.4)), which is typical of PEDOT:PSS devices gated by Ag/AgCl.

This situation is reversed in the output curves, as when V_D increases from low values the local potential $(V_D - V_{LG})$ allows redox activity to occur. However, because the gate and source potentials are at steady-state[6], no electrochemical current will flow there. Accordingly, steady-state transfer curves can be extracted from the output curves by slicing as shown by the point markers in Fig. A.7. Good quantitative agreement with the transfer curves taken by sweeping V_{LG} is observed, with reduced hysteresis.

[6]Whether steady state is actually reached will depend on the sweep rate, which in the present measurement is sufficiently slow.

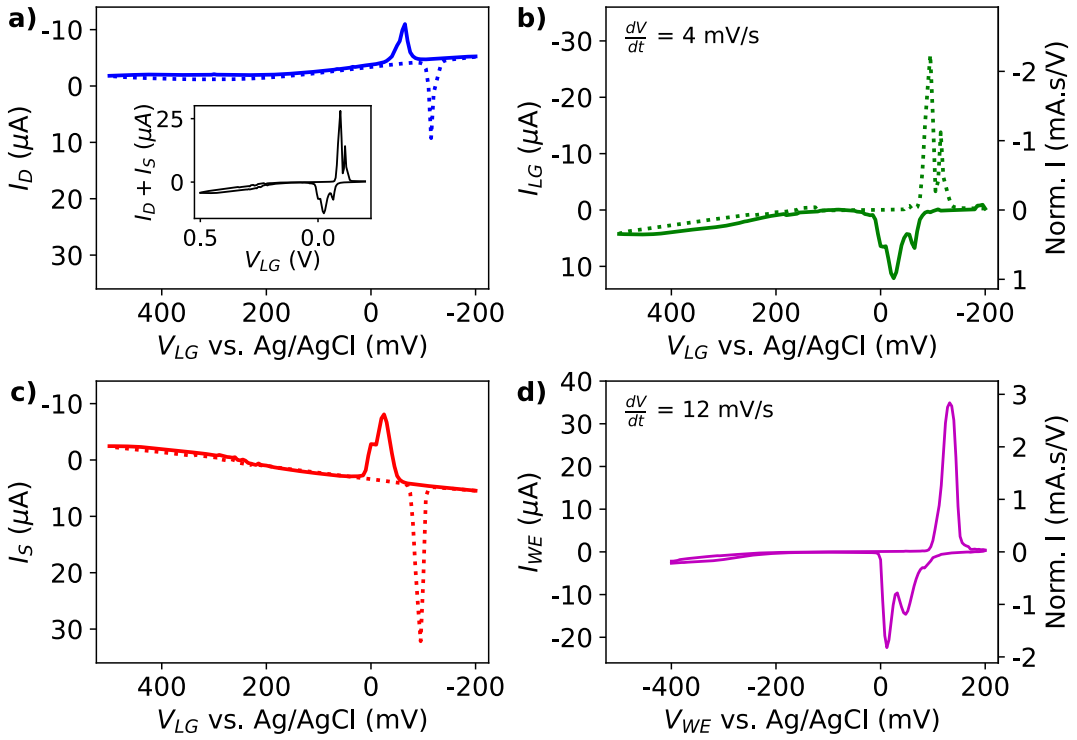

Figure A.8: Transfer curves (a, b, c) of a representative PEDOT:PSS thin-film OECT operating in the linear regime ($V_{DS} = -10\,\text{mV}$) in PBS (pH 7.4). Cyclic voltammogram (d) of a similar thin-film. Note that the abscissa is inverted as $V_{WE} = -V_{LG}$. Current values of (b, d) normalized to the sweep rate used are shown on the right axes. Inset in (a) shows the sum of drain and source currents, which reproduces the inverted gate current waveform. Potential sweep rates for each measurement are indicated in (b) and (d), respectively. Solid lines with represent the first half of a cyclic sweep of V_{LG}.

Characterization in linear regime

In contrast to the behaviour of the steady-state output curves shown in Fig. A.7, during transfer measurements of the OECT biased in the linear regime (i.e., V_{DS} is small and negative), redox current flows jointly between source and drain. As shown in Fig. A.8, the small operating bias results in leakage currents to the gate on the same order of magnitude as the lateral OECT current. The sum of I_D and I_S reproduce the shape and magnitude of I_G well, indicating that redox currents are superimposed on the transistor output.

To demonstrate the correspondence of the gate leakage to the electrochemical behaviour of the PEDOT:PSS thin-film, cyclic voltammetry was performed on an adjacent electrode which had its channel disconnected (Fig. A.8d). Qualitatively, the same peak features are observed, with merging of the doublet in the oxidative peaks around $V_{LG} = -150\,\text{mV}$ in Fig. A.8b. From this we infer that this peak splitting in the OECT gate leakage is caused by the applied source-drain bias, $V_{DS} = -10\,\text{mV}$.

A.3.3 pH responsivity of large area films

Owing to the fact that polaronic charge transport in CPs relies on anionic counter-ions to balance the positive hole left behind by oxidation of the conjugated monomer unit (see also Section 1.2.1), which is fulfilled in PEDOT:PSS by the sulfonic acid moiety, intrinsic pH dependence of carrier density may be expected according to the titration curve of PSS [43]. Thus, we investigated the transient current response of a PEDOT:PSS thin-film in varying buffer solutions at pH 1.7, 4.0, 7.4, and 10.0 (oxalate, phthalate, phosphate, and carbonate, respectively; Wako Pure Chem. Corp.). A device configured for a van der Pauw measurement was used (i.e., a four-terminal configuration), ensuring that the measured current is attributable to the channel and not contact resistance effects.

In a chemiresistor arrangement (i.e., floating gate), a positive $V_{DS} = 200\,\mathrm{mV}$ was used ensure a supply of holes into the channel. Figure A.9 shows the data for two starting conditions, acidic or alkaline, with output current normalized by the initial steady-state value in air (I/I_o). As expected, the response is enhanced in acidic buffers and suppressed in alkaline ones. This is due to the decrease of anionic charge of PSS with increasing pH [43]. Moreover, the response time is slower in Fig. A.9a on account of the difference in area of the devices used (ca. $200\,\mu\mathrm{m}^2$ vs. $128\,\mu\mathrm{m}^2$).

At steady-state, both traces exhibit a linear response to pH (shown in the insets), with a slope of -9×10^{-3} and $-8 \times 10^{-3}\,\mathrm{pH}^{-1}$ for the acidic and alkaline starting conditions, respectively. Though the sensitivity is unchanged with the reversing of pH, significant hysteresis is observed with an extended linear response when pH is decreasing. At the same time, the response shifts after the turning point suggest that an irreversible or slow change is occurring in the PEDOT:PSS thin-films. Results from molecular dynamics simulations of anionic polyelectrolytes have shown that, depending on the polymer conformation and its effects on electrostatic screening, local pH at the polymer and bulk pH in the buffer may differ up to two or more units [142]. Such effects may be exacerbated in conductive polymer hydrogels, as the change in carrier concentration can effect large scale structural (i.e. swelling) changes [115, 118].

A.4 Conclusions

Though the direction of this thesis ultimately arrived at thick channels composed of CP hydrogels, the early work on characterizing the electrical and electrochemical behaviour of PEDOT:PSS as a thin-film, and operating conditions of OECTs proved exceptionally useful in performing and analyzing the later experimental results.

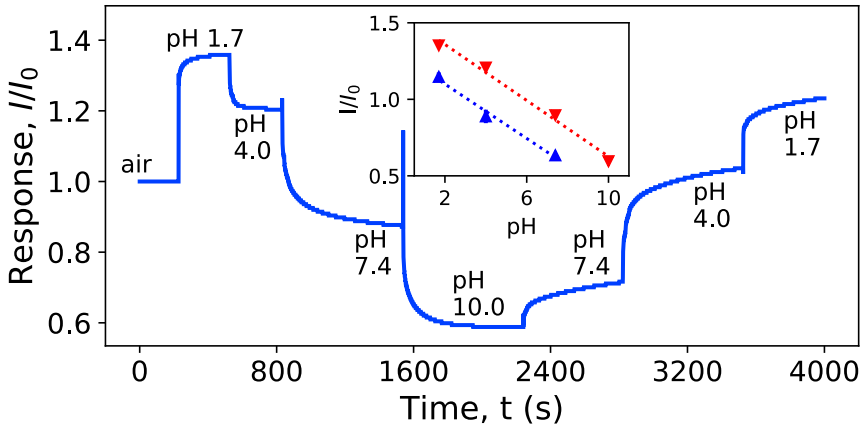

(a) acidic start

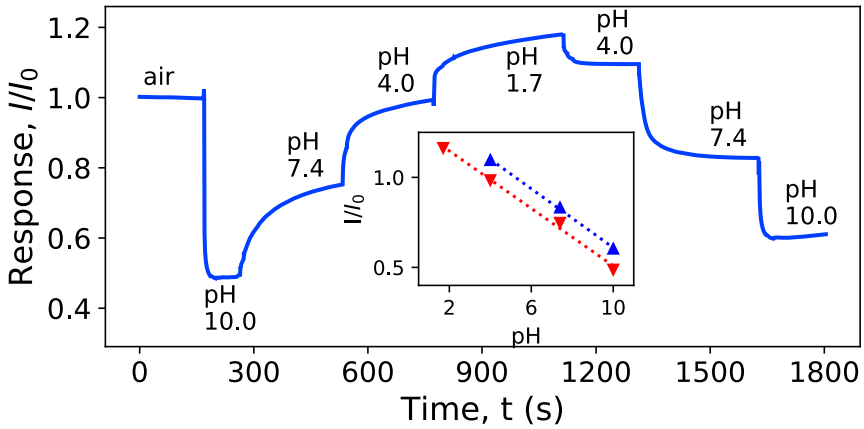

(b) alkaline start

Figure A.9: Normalized current response for large area PEDOT:PSS thin-films operated as four-terminal chemiresistors ($V_{DS} = 200\,\mathrm{mV}$, floating gate). Insets show the change of response with pH for increasing (blue △) and decreasing (red ▽) pH steps.

Appendix B

Publications associated with this Thesis

Original papers for the Journal with peer review

1. **Tseng, Alex C.**; Ito, K.; Lynall, D.; Savelyev, I. G.; Blumin, M.; Wang, S.; Ruda, H. E.; Sakata, T. Ion sensitivity from current hysteresis in InAs nanowire field-effect transistors functionalized with ionophore-doped fluorosilicone membranes. *Sensors and Actuators B: Chemical* **2021**, *336*, 129704

2. **Tseng, Alex C.**; Sakata, T. Direct electrochemical signaling in organic electrochemical transistors comprising high-conductivity double-network hydrogels, *in preparation*, 2021

3. **Tseng, Alex C.**; Sakata, T. Redox-mediated, reversible resistance switching in conductive polymer hydrogels, *in preparation*, 2021

Original papers for the Journal without peer review

Proceedings for the Conferences with peer review

1. **Tseng, Alex C.**; Ruda, H. E.; Sakata, T. Evaluation of sodium ion responsivity with InAs nanowire field-effect transistors functionalized by ionophore-doped fluorosilicone membranes, oral presentation in The 80th Japan Society of Applied Physics Autumn Meeting, Sapporo, Japan, Sept. 18-21, 2019

2. **Tseng, Alex C.**; Ruda, H. E.; Sakata, T. Ion sensitivity from current hysteresis in InAs nanowire field-effect transistors functionalized by ionophore-doped fluorosilicone membranes, oral presentation at Reiwa 3rd General Meeting of the Sensors and Micromachines Technical Society of The Institute of Electrical Engineers of Japan, held online, July 26-27, 2021

3. **Tseng, Alex C.**; Sakata, T. Electrochemical characterization of highly conductive PEDOT:PSS:Poly(acrylamide)-based hydrogels containing phenylboronic acid, oral presentation in The 82nd Japan Society of Applied Physics Autumn Meeting, held online, Sept. 10-13, 2021

4. **Tseng, Alex C.**; Sakata, T. Electrochemical detection of glucose with highly conductive PEDOT:PSS:Poly(acrylamide)-based hydrogels containing phenylboronic acid, oral presentation in 2021 Materials Research Society Fall Meeting & Exhibit, hybrid meeting (Virtual), Dec. 6-8, 2021

5. **Tseng, Alex C.**; Sakata, T. Evaluation of organic electrochemical transistors with highly conductive hydrogel channels for biosensing application, *accepted for* oral presentation in The 69th Japan Society of Applied Physics Spring Meeting, Mar. 22-26, 2022

Proceedings for the Conferences without peer review

1. **Tseng, Alex C.**; Ruda, H. E.; Sakata, T. Evaluation of sodium ion responsivity with InAs nanowire field-effect transistors functionalized by ionophore-doped fluorosilicone membranes, oral presentation in Biosensor Summer Seminar 2019, Shiga, Japan, Aug. 21-22, 2019

Review, books and others

Bibliography

(1) Sakata, T. *ACS Omega* **2019**, *4*, 11852–11862.

(2) Someya, T.; Bao, Z.; Malliaras, G. G. *Nature* **2016**, *540*, 379–385.

(3) Jiang, F.; Jiang, Y.; Zhi, H.; Dong, Y.; Li, H.; Ma, S.; Wang, Y.; Dong, Q.; Shen, H.; Wang, Y. *Stroke and Vascular Neurology* **2017**, *2*, DOI: 10.1136/svn-2017-000101.

(4) Wang, J. *Chemical Reviews* **2008**, *108*, 814–825.

(5) Tereshchenko, A.; Bechelany, M.; Viter, R.; Khranovskyy, V.; Smyntyna, V.; Starodub, N.; Yakimova, R. *Sensors and Actuators B: Chemical* **2016**, *229*, 664–677.

(6) Xu, S. *Microchimica Acta* **2012**, *178*, 245–260.

(7) Jianrong, C.; Yuqing, M.; Nongyue, H.; Xiaohua, W.; Sijiao, L. *Biotechnology Advances* **2004**, *22*, 505–518.

(8) Zhang, A.; Lieber, C. M. *Chemical Reviews* **2016**, *116*, 215–257.

(9) Axpe, E.; Orive, G.; Franze, K.; Appel, E. A. *Nature Communications* **2020**, *11*, 3423.

(10) Zeglio, E.; Rutz, A. L.; Winkler, T. E.; Malliaras, G. G.; Herland, A. *Advanced Materials* **2019**, *31*, 1806712.

(11) Shirakawa, H.; Louis, E. J.; MacDiarmid, A. G.; Chiang, C. K.; Heeger, A. J. *Journal of the Chemical Society, Chemical Communications* **1977**, 578–580.

(12) Chiang, C. K. *Physical Review Letters* **1977**, *39*, 1098–1101.

(13) Balint, R.; Cassidy, N. J.; Cartmell, S. H. *Acta Biomaterialia* **2014**, *10*, 2341–2353.

(14) Alemu, D.; Wei, H.-Y.; Ho, K.-C.; Chu, C.-W. *Energy & Environmental Science* **2012**, *5*, 9662–9671.

(15) Hoppe, H.; Sariciftci, N. S. *Journal of Materials Research* **2004**, *19*, 1924–1945.

(16) Wang, Y.; Vogel, A.; Sachs, M.; Sprick, R. S.; Wilbraham, L.; Moniz, S. J. A.; Godin, R.; Zwijnenburg, M. A.; Durrant, J. R.; Cooper, A. I.; Tang, J. *Nature Energy* **2019**, *4*, 746–760.

(17) Bubnova, O. et al. *Nature Materials* **2014**, *13*, 190–194.

(18) Liu, J.; Wang, J.; Xu, C.; Jiang, H.; Li, C.; Zhang, L.; Lin, J.; Shen, Z. X. *Advanced Science* **2018**, *5*, 1700322.

(19) Bryan, A. M.; Santino, L. M.; Lu, Y.; Acharya, S.; D'Arcy, J. M. *Chemistry of Materials* **2016**, *28*, 5989–5998.

(20) Gustafsson, J. C.; Liedberg, B.; Inganäs, O. *Solid State Ionics* **1994**, *69*, 145–152.

(21) Bredas, J. L.; Street, G. B. *Accounts of Chemical Research* **1985**, *18*, 309–315.

(22) MacDiarmid, A. G.; Mammone, R. J.; Kaner, R. B.; Porter, S. J.; Pethig, R.; Heeger, A. J.; Rosseinsky, D. R. *Philosophical Transactions of the Royal Society of London. Series A, Mathematical and Physical Sciences* **1985**, *314*, 3–15.

(23) Zozoulenko, I.; Singh, A.; Singh, S. K.; Gueskine, V.; Crispin, X.; Berggren, M. *ACS Applied Polymer Materials* **2019**, *1*, 83–94.

(24) Groenendaal, L.; Jonas, F.; Freitag, D.; Pielartzik, H.; Reynolds, J. R. *Advanced Materials* **2000**, *12*, 481–494.

(25) Shi, H.; Liu, C.; Jiang, Q.; Xu, J. *Advanced Electronic Materials* **2015**, *1*, 1500017.

(26) Van Reenen, S.; Scheepers, M.; van de Ruit, K.; Bollen, D.; Kemerink, M. *Organic Electronics* **2014**, *15*, 3710–3714.

(27) Ouyang, J.; Xu, Q.; Chu, C.-W.; Yang, Y.; Li, G.; Shinar, J. *Polymer* **2004**, *45*, 8443–8450.

(28) Database, H. M. Human Metabolome Database: Showing metabocard for Polystyrene sulfonate (HMDB0015435) `https://hmdb.ca/metabolites/HMDB0015435` (accessed 11/22/2021).

(29) Neumann, M. G.; Pastre, I. A.; Chinelatto, A. M.; El Seoud, O. A. *Colloid and Polymer Science* **1996**, *274*, 475–481.

(30) Martin, D. C.; Wu, J.; Shaw, C. M.; King, Z.; Spanninga, S. A.; Richardson-Burns, S.; Hendricks, J.; Yang, J. *Polymer Reviews* **2010**, *50*, 340–384.

(31) Wang, X.; Zhang, X.; Sun, L.; Lee, D.; Lee, S.; Wang, M.; Zhao, J.; Shao-Horn, Y.; Dincă, M.; Palacios, T.; Gleason, K. K. *Science Advances* **2018**, *4*, eaat5780.

(32) Leaf, M. A.; Muthukumar, M. *Macromolecules* **2016**, *49*, 4286–4294.

(33) Samitsu, S.; Shimomura, T.; Ito, K.; Fujimori, M.; Heike, S.; Hashizume, T. *Applied Physics Letters* **2005**, *86*, 233103.

(34) Cao, Y.; Kovalev, A. E.; Xiao, R.; Kim, J.; Mayer, T. S.; Mallouk, T. E. *Nano Letters* **2008**, *8*, 4653–4658.

(35) Xia, Y.; Ouyang, J. *ACS Applied Materials & Interfaces* **2010**, *2*, 474–483.

(36) Kim, N.; Kee, S.; Lee, S. H.; Lee, B. H.; Kahng, Y. H.; Jo, Y.-R.; Kim, B.-J.; Lee, K. *Advanced Materials* **2014**, *26*, 2268–2272.

(37) Kim, S.-M.; Kim, C.-H.; Kim, Y.; Kim, N.; Lee, W.-J.; Lee, E.-H.; Kim, D.; Park, S.; Lee, K.; Rivnay, J.; Yoon, M.-H. *Nature Communications* **2018**, *9*, 1–9.

(38) Gueye, M. N.; Carella, A.; Faure-Vincent, J.; Demadrille, R.; Simonato, J.-P. *Progress in Materials Science* **2020**, *108*, 100616.

(39) Lu, B.; Yuk, H.; Lin, S.; Jian, N.; Qu, K.; Xu, J.; Zhao, X. *Nature Communications* **2019**, *10*, 1043.

(40) Rivnay, J.; Inal, S.; Collins, B. A.; Sessolo, M.; Stavrinidou, E.; Strakosas, X.; Tassone, C.; Delongchamp, D. M.; Malliaras, G. G. *Nature Communications* **2016**, *7*, 11287.

(41) Tybrandt, K.; Zozoulenko, I. V.; Berggren, M. *Science Advances* **2017**, *3*, eaao3659.

(42) Savva, A.; Wustoni, S.; Inal, S. *Journal of Materials Chemistry C* **2018**, *6*, 12023–12030.

(43) Mochizuki, Y.; Horii, T.; Okuzaki, H. *Transactions of the Materials Research Society of Japan* **2012**, *37*, 307–310.

(44) Lin, P.; Yan, F.; Chan, H. L. W. *ACS Applied Materials & Interfaces* **2010**, *2*, 1637–1641.

(45) Martinez, J. G.; Berrueco, B.; Otero, T. F. *Frontiers in Bioengineering and Biotechnology* **2015**, *3*, 15.

(46) Stavrinidou, E.; Leleux, P.; Rajaona, H.; Khodagholy, D.; Rivnay, J.; Lindau, M.; Sanaur, S.; Malliaras, G. G. *Advanced Materials* **2013**, *25*, 4488–4493.

(47) White, H. S.; Kittlesen, G. P.; Wrighton, M. S. *Journal of the American Chemical Society* **1984**, *106*, 5375–5377.

(48) Robinson, N. D.; Svensson, P.-O.; Nilsson, D.; Berggren, M. *Journal of The Electrochemical Society* **2006**, *153*, H39–H44.

(49) Bernards, D. A.; Malliaras, G. G. *Advanced Functional Materials* **2007**, *17*, 3538–3544.

(50) Friedlein, J. T.; Shaheen, S. E.; Malliaras, G. G.; McLeod, R. R. *Advanced Electronic Materials* **2015**, *1*, 1500189.

(51) Sze, S.; Ng, K. K. In *Physics of Semiconductor Devices*, 3rd; John Wiley & Sons, Inc.: Hoboken, New Jersey, 2007.

(52) Friedlein, J. T.; McLeod, R. R.; Rivnay, J. *Organic Electronics* **2018**, *63*, 398–414.

(53) Khodagholy, D.; Rivnay, J.; Sessolo, M.; Gurfinkel, M.; Leleux, P.; Jimison, L. H.; Stavrinidou, E.; Herve, T.; Sanaur, S.; Owens, R. M.; Malliaras, G. G. *Nature Communications* **2013**, *4*, 2133.

(54) Koutsouras, D. A.; Gkoupidenis, P.; Stolz, C.; Subramanian, V.; Malliaras, G. G.; Martin, D. C. *ChemElectroChem* **2017**, *4*, 2321–2327.

(55) Faria, G. C.; Duong, D. T.; Salleo, A. *Organic Electronics* **2017**, *45*, 215–221.

(56) Rivnay, J.; Leleux, P.; Sessolo, M.; Khodagholy, D.; Hervé, T.; Fiocchi, M.; Malliaras, G. G. *Advanced Materials* **2013**, *25*, 7010–7014.

(57) Friedlein, J. T.; Donahue, M. J.; Shaheen, S. E.; Malliaras, G. G.; McLeod, R. R. *Advanced Materials* **2016**, *28*, 8398–8404.

(58) Rivnay, J.; Leleux, P.; Ferro, M.; Sessolo, M.; Williamson, A.; Koutsouras, D. A.; Khodagholy, D.; Ramuz, M.; Strakosas, X.; Owens, R. M.; Benar, C.; Badier, J.-M.; Bernard, C.; Malliaras, G. G. *Science Advances* **2015**, *1*, e1400251.

(59) Hempel, F.; Law, J. K.-Y.; Nguyen, T. C.; Munief, W.; Lu, X.; Pachauri, V.; Susloparova, A.; Vu, X. T.; Ingebrandt, S. *Biosensors and Bioelectronics* **2017**, *93*, 132–138.

(60) Tyrrell, J. E.; Boutelle, M. G.; Campbell, A. J. *Advanced Functional Materials* **2021**, *31*, 2007086.

(61) Savva, A.; Hallani, R.; Cendra, C.; Surgailis, J.; Hidalgo, T. C.; Wustoni, S.; Sheelamanthula, R.; Chen, X.; Kirkus, M.; Giovannitti, A.; Salleo, A.; McCulloch, I.; Inal, S. *Advanced Functional Materials* **2020**, *30*, 1907657.

(62) Wu, X.; Surendran, A.; Ko, J.; Filonik, O.; Herzig, E. M.; Müller-Buschbaum, P.; Leong, W. L. *Advanced Materials* **2019**, *31*, 1805544.

(63) Spyropoulos, G. D.; Gelinas, J. N.; Khodagholy, D. *Science Advances* **2019**, *5*, eaau7378.

(64) Khodagholy, D.; Doublet, T.; Quilichini, P.; Gurfinkel, M.; Leleux, P.; Ghestem, A.; Ismailova, E.; Hervé, T.; Sanaur, S.; Bernard, C.; Malliaras, G. G. *Nature Communications* **2013**, *4*, 1575.

(65) Rivnay, J.; Ramuz, M.; Leleux, P.; Hama, A.; Huerta, M.; Owens, R. M. *Applied Physics Letters* **2015**, *106*, 043301.

(66) Gu, X.; Yao, C.; Liu, Y.; Hsing, I.-M. *Advanced Healthcare Materials* **2016**, *5*, 2345–2351.

(67) Yeung, S. Y.; Gu, X.; Tsang, C. M.; Tsao, S. W. G.; Hsing, I.-m. *Sensors and Actuators B: Chemical* **2019**, *297*, 126761.

(68) Tybrandt, K.; Kollipara, S. B.; Berggren, M. *Sensors and Actuators B: Chemical* **2014**, *195*, 651–656.

(69) Kaphle, V.; Liu, S.; Al-Shadeedi, A.; Keum, C.-M.; Lüssem, B. *Advanced Materials* **2016**, *28*, 8766–8770.

(70) Inal, S.; Malliaras, G. G.; Rivnay, J. *Nature Communications* **2017**, *8*, 1–7.

(71) Van Hal, R. E. G.; Eijkel, J. C. T.; Bergveld, P. *Advances in Colloid and Interface Science* **1996**, *69*, 31–62.

(72) Bergveld, P. *IEEE Transactions on Biomedical Engineering* **1970**, *BME-17*, 70–71.

(73) Lowe, B. M.; Sun, K.; Zeimpekis, I.; Skylaris, C.-K.; Green, N. G. *Analyst* **2017**, *142*, 4173–4200.

(74) Sessolo, M.; Rivnay, J.; Bandiello, E.; Malliaras, G. G.; Bolink, H. J. *Advanced Materials* **2014**, *26*, 4803–4807.

(75) Ito, K.; Nishimura, K.; Ikeda, K.; Matsuzawa, K.; Tezuka, T.; Sakata, T. *Journal of The Electrochemical Society* **2018**, *165*, B571–B575.

(76) Gualandi, I.; Scavetta, E.; Mariani, F.; Tonelli, D.; Tessarolo, M.; Fraboni, B. *Electrochimica Acta* **2018**, *268*, 476–483.

(77) Demelas, M.; Scavetta, E.; Basiricò, L.; Rogani, R.; Bonfiglio, A. *Applied Physics Letters* **2013**, *102*, 193301.

(78) Cicoira, F.; Sessolo, M.; Yaghmazadeh, O.; DeFranco, J. A.; Yang, S. Y.; Malliaras, G. G. *Advanced Materials* **2010**, *22*, 1012–1016.

(79) Tarabella, G.; Santato, C.; Yang, S. Y.; Iannotta, S.; Malliaras, G. G.; Cicoira, F. *Applied Physics Letters* **2010**, *97*, 123304.

(80) Lin, F.; Lonergan, M. C. *Applied Physics Letters* **2006**, *88*, 133507.

(81) Liao, J.; Si, H.; Zhang, X.; Lin, S. *Sensors* **2019**, *19*, 218.

(82) Gualandi, I.; Marzocchi, M.; Scavetta, E.; Calienni, M.; Bonfiglio, A.; Fraboni, B. *Journal of Materials Chemistry B* **2015**, *3*, 6753–6762.

(83) Gualandi, I.; Tonelli, D.; Mariani, F.; Scavetta, E.; Marzocchi, M.; Fraboni, B. *Scientific Reports* **2016**, *6*, 35419.

(84) Gualandi, I.; Marzocchi, M.; Achilli, A.; Cavedale, D.; Bonfiglio, A.; Fraboni, B. *Scientific Reports* **2016**, *6*, 1–10.

(85) Mariani, F.; Gualandi, I.; Tessarolo, M.; Fraboni, B.; Scavetta, E. *ACS Applied Materials & Interfaces* **2018**, *10*, 22474–22484.

(86) Mantione, D.; Del Agua, I.; Sanchez-Sanchez, A.; Mecerreyes, D. *Polymers* **2017**, *9*, 354.

(87) Wustoni, S.; Combe, C.; Ohayon, D.; Akhtar, M. H.; McCulloch, I.; Inal, S. *Advanced Functional Materials* **2019**, *0*, 1904403.

(88) Lin, H.-A.; Zhu, B.; Wu, Y.-W.; Sekine, J.; Nakao, A.; Luo, S.-C.; Yamashita, Y.; Yu, H.-H. *Advanced Functional Materials* **2018**, *28*, 1703890.

(89) Zeglio, E.; Schmidt, M. M.; Thelakkat, M.; Gabrielsson, R.; Solin, N.; Inganäs, O. *Chemistry of Materials* **2017**, *29*, 4293–4300.

(90) Zeglio, E.; Vagin, M.; Musumeci, C.; Ajjan, F. N.; Gabrielsson, R.; Trinh, X. T.; Son, N. T.; Maziz, A.; Solin, N.; Inganäs, O. *Chemistry of Materials* **2015**, 6385–6393.

(91) Means, A. K.; Grunlan, M. A. *ACS Macro Letters* **2019**, *8*, 705–713.

(92) Zhang, S. et al. *Advanced Functional Materials* **2020**, *30*, 1906016.

(93) Fan, J.; Montemagno, C.; Gupta, M. *Organic Electronics* **2019**, *73*, 122–129.

(94) Ait Yazza, A.; Blondeau, P.; Andrade, F. J. *ACS Applied Electronic Materials* **2021**, *3*, 1886–1895.

(95) Guex, A. G.; Puetzer, J. L.; Armgarth, A.; Littmann, E.; Stavrinidou, E.; Giannelis, E. P.; Malliaras, G. G.; Stevens, M. M. *Acta Biomaterialia* **2017**, *62*, 91–101.

(96) Bertana, V.; Scordo, G.; Parmeggiani, M.; Scaltrito, L.; Ferrero, S.; Gomez, M. G.; Cocuzza, M.; Vurro, D.; D'Angelo, P.; Iannotta, S.; Pirri, C. F.; Marasso, S. L. *Scientific Reports* **2020**, *10*, 13335.

(97) Xu, Y.; Yang, X.; Thomas, A. K.; Patsis, P. A.; Kurth, T.; Kräter, M.; Eckert, K.; Bornhäuser, M.; Zhang, Y. *ACS Applied Materials & Interfaces* **2018**, *10*, 14418–14425.

(98) Yao, B.; Wang, H.; Zhou, Q.; Wu, M.; Zhang, M.; Li, C.; Shi, G. *Advanced Materials* **2017**, *29*, 1700974.

(99) Zhang, S. et al. *Advanced Materials* **2020**, *32*, 1904752.

(100) Feig, V. R.; Tran, H.; Lee, M.; Bao, Z. *Nature Communications* **2018**, *9*, 1–9.

(101) Dai, T.; Qing, X.; Zhou, H.; Shen, C.; Wang, J.; Lu, Y. *Synthetic Metals* **2010**, *160*, 791–796.

(102) Kishi, R.; Hiroki, K.; Tominaga, T.; Sano, K.-I.; Okuzaki, H.; Martinez, J. G.; Otero, T. F.; Osada, Y. *Journal of Polymer Science Part B: Polymer Physics* **2012**, *50*, 790–796.

(103) An, Y.; Iwashita, K.; Okuzaki, H. *Multifunctional Materials* **2018**, *2*, 014001.

(104) Wu, Q.; Wei, J.; Xu, B.; Liu, X.; Wang, H.; Wang, W.; Wang, Q.; Liu, W. *Scientific Reports* **2017**, *7*, 41566.

(105) Wustoni, S.; Savva, A.; Sun, R.; Bihar, E.; Inal, S. *Advanced Materials Interfaces* **2019**, *6*, 1800928.

(106) Ouyang, J. *ACS Applied Materials & Interfaces* **2013**, *5*, 13082–13088.

(107) Chen, S.; Song, L.; Tao, Z.; Shao, X.; Huang, Y.; Cui, Q.; Guo, X. *Organic Electronics* **2014**, *15*, 3654–3659.

(108) Kim, S.; Kim, S. Y.; Chung, M. H.; Kim, J.; Kim, J. H. *Journal of Materials Chemistry C* **2015**, *3*, 5859–5868.

(109) Stellwagen, E.; Prantner, J. D.; Stellwagen, N. C. *Analytical Biochemistry* **2008**, *373*, 407–409.

(110) Van der Pauw, L. *Philips Research Reports* **1958**, *13*.

(111) Kaphle, V.; Paudel, P. R.; Dahal, D.; Radha Krishnan, R. K.; Lüssem, B. *Nature Communications* **2020**, *11*, 2515.

(112) Bisquert, J.; Garcia-Belmonte, G.; García-Cañadas, J. *The Journal of Chemical Physics* **2004**, *120*, 6726–6733.

(113) Savva, A.; Cendra, C.; Giugni, A.; Torre, B.; Surgailis, J.; Ohayon, D.; Giovannitti, A.; McCulloch, I.; Di Fabrizio, E.; Salleo, A.; Rivnay, J.; Inal, S. *Chemistry of Materials* **2019**, *31*, 927–937.

(114) Giridharagopal, R.; Flagg, L. Q.; Harrison, J. S.; Ziffer, M. E.; Onorato, J.; Luscombe, C. K.; Ginger, D. S. *Nature Materials* **2017**, *16*, 737–742.

(115) Otero, T. F.; Alfaro, M.; Martinez, V.; Perez, M. A.; Martinez, J. G. *Advanced Functional Materials* **2013**, *23*, 3929–3940.

(116) Luo, H.; Wu, K.; Wang, Q.; Zhang, T. C.; Lu, H.; Rong, H.; Fang, Q. *Journal of Membrane Science* **2020**, *593*, 117406.

(117) Inoue, A.; Yuk, H.; Lu, B.; Zhao, X. *Science Advances* **2020**, *6*, eaay5394.

(118) Otero, T. F.; Boyano, I. *The Journal of Physical Chemistry B* **2003**, *107*, 6730–6738.

(119) Paasch, G.; Nguyen, P. H.; Fisher, A. J. *Chemical Physics* **1998**, *227*, 219–241.

(120) Macdonald, J. R. *Annals of Biomedical Engineering* **1992**, *20*, 289–305.

(121) Schauer, F.; Nádaždy, V.; Gmucová, K.; Váry, T. *Journal of Applied Physics* **2018**, *124*, 165702.

(122) Schauer, F.; Nádaždy, V.; Gmucová, K. *Journal of Applied Physics* **2018**, *123*, 161590.

(123) Anderson, E. L.; Bühlmann, P. *Analytical Chemistry* **2016**, *88*, 9738–9745.

(124) Fletcher, S. *Electrochemistry Communications* **2001**, *3*, 692–696.

(125) Dost, R.; Das, A.; Grell, M. *Journal of Applied Physics* **2008**, *104*, 084519.

(126) Weis, M.; Lin, J.; Taguchi, D.; Manaka, T.; Iwamoto, M. *The Journal of Physical Chemistry C* **2009**, *113*, 18459–18461.

(127) Friedlein, J. T.; Rivnay, J.; Dunlap, D. H.; McCulloch, I.; Shaheen, S. E.; McLeod, R. R.; Malliaras, G. G. *Applied Physics Letters* **2017**, *111*, 023301.

(128) Arkhipov, V. I.; Heremans, P.; Emelianova, E. V.; Adriaenssens, G. J.; Bässler, H. *Applied Physics Letters* **2003**, *82*, 3245–3247.

(129) Tanase, C. *Physical Review Letters* **2003**, *91*, DOI: `10.1103/PhysRevLett.91.216601`.

(130) W. Colburn, A.; J. Levey, K.; O'Hare, D.; V. Macpherson, J. *Physical Chemistry Chemical Physics* **2021**, *23*, 8100–8117.

(131) Paulsen, B. D.; Frisbie, C. D. *The Journal of Physical Chemistry C* **2012**, *116*, 3132–3141.

(132) Ding, M.; He, Q.; Wang, G.; Cheng, H.-C.; Huang, Y.; Duan, X. *Nature Communications* **2015**, *6*, 7867.

(133) Tseng, A. C.; Ito, K.; Lynall, D.; Savelyev, I. G.; Blumin, M.; Wang, S.; Ruda, H. E.; Sakata, T. *Sensors and Actuators B: Chemical* **2021**, *336*, 129704.

(134) Wang, N.; Liu, Y.; Fu, Y.; Yan, F. *ACS Applied Materials & Interfaces* **2018**, *10*, 25834–25840.

(135) Sakata, T.; Nishitani, S.; Kajisa, T. *RSC Advances* **2020**, *10*, 16999–17013.

(136) Li, M.; Zhu, W.; Marken, F.; James, T. D. *Chemical Communications* **2015**, *51*, 14562–14573.

(137) Vancoillie, G.; Hoogenboom, R. *Polymer Chemistry* **2016**, *7*, 5484–5495.

(138) Furikado, Y.; Nagahata, T.; Okamoto, T.; Sugaya, T.; Iwatsuki, S.; Inamo, M.; Takagi, H. D.; Odani, A.; Ishihara, K. *Chemistry – A European Journal* **2014**, *20*, 13194–13202.

(139) Hiller, N. d. J.; do Amaral e Silva, N. A.; Tavares, T. A.; Faria, R. X.; Eberlin, M. N.; de Luna Martins, D. *European Journal of Organic Chemistry* **2020**, *2020*, 4841–4877.

(140) Graham, B. J.; Windsor, I. W.; Gold, B.; Raines, R. T. *Proceedings of the National Academy of Sciences* **2021**, *118*, DOI: `10.1073/pnas.2013691118`.

(141) Hai, W.; Pu, S.; Wang, X.; Bao, L.; Han, N.; Duan, L.; Liu, J.; Goda, T.; Wu, W. *Langmuir* **2020**, *36*, 546–553.

(142) Nová, L.; Uhlík, F.; Košovan, P. *Physical Chemistry Chemical Physics* **2017**, *19*, 14376–14387.

(143) Mitraka, E.; Gryszel, M.; Vagin, M.; Jafari, M. J.; Singh, A.; Warczak, M.; Mitrakas, M.; Berggren, M.; Ederth, T.; Zozoulenko, I.; Crispin, X.; Głowacki, E. D. *Advanced Sustainable Systems* **2019**, *3*, 1800110.

(144) Stojek, Z.; Osteryoung, J. *Analytical Chemistry* **1991**, *63*, 839–841.

(145) Wong, C. M.; Wong, K. H.; Chen, X. D. *Applied Microbiology and Biotechnology* **2008**, *78*, 927–938.

(146) Ofer, D.; Crooks, R. M.; Wrighton, M. S. *Journal of the American Chemical Society* **1990**, *112*, 7869–7879.

(147) Hulea, I. N. *Physical Review Letters* **2004**, *93*, DOI: 10.1103/PhysRevLett.93.166601.

(148) Ahonen, H. J.; Lukkari, J.; Kankare, J. *Macromolecules* **2000**, *33*, 6787–6793.

(149) Zotti, G.; Zecchin, S.; Schiavon, G.; Vercelli, B.; Berlin, A.; Dalcanale, E.; Groenendaal, L. B. *Chemistry of Materials* **2003**, *15*, 4642–4650.

(150) Pomerantz, Z.; Zaban, A.; Ghosh, S.; Lellouche, J.-P.; Garcia-Belmonte, G.; Bisquert, J. *Journal of Electroanalytical Chemistry* **2008**, *614*, 49–60.

(151) Skompska, M.; Mieczkowski, J.; Holze, R.; Heinze, J. *Journal of Electroanalytical Chemistry* **2005**, *577*, 9–17.

(152) Panzer, M. J.; Frisbie, C. D. *Journal of the American Chemical Society* **2007**, *129*, 6599–6607.

(153) Bhansali, U. S.; Khan, M. A.; Cha, D.; AlMadhoun, M. N.; Li, R.; Chen, L.; Amassian, A.; Odeh, I. N.; Alshareef, H. N. *ACS Nano* **2013**, *7*, 10518–10524.

(154) Nguyen, V. C.; Lee, P. S. *Scientific Reports* **2016**, *6*, 19594.

(155) Fabiano, S.; Sani, N.; Kawahara, J.; Kergoat, L.; Nissa, J.; Engquist, I.; Crispin, X.; Berggren, M. *Science Advances* **2017**, *3*, e1700345.

(156) Geise, G. M.; Freeman, B. D.; Paul, D. R. *Journal of Membrane Science* **2013**, *427*, 186–196.

(157) Maw, S.; Smela, E.; Yoshida, K.; Stein, R. B. *Synthetic Metals* **2005**, *155*, 18–26.

(158) Bay, L.; Jacobsen, T.; Skaarup, S.; West, K. *The Journal of Physical Chemistry B* **2001**, *105*, 8492–8497.

(159) Kajisa, T.; Sakata, T. *Japanese Journal of Applied Physics* **2015**, *54*, 04DL06.

(160) Yu, H. Z.; Zhao, J. W.; Wang, Y. Q.; Cai, S. M.; Liu, Z. F. *Journal of Electroanalytical Chemistry* **1997**, *438*, 221–224.

(161) Zheng, L.; Sundaram, H. S.; Wei, Z.; Li, C.; Yuan, Z. *Reactive and Functional Polymers* **2017**, *118*, 51–61.

(162) Zhang, S.; Kumar, P.; Nouas, A. S.; Fontaine, L.; Tang, H.; Cicoira, F. *APL Materials* **2014**, *3*, 014911.

(163) Håkansson, A.; Han, S.; Wang, S.; Lu, J.; Braun, S.; Fahlman, M.; Berggren, M.; Crispin, X.; Fabiano, S. *Journal of Polymer Science Part B: Polymer Physics* **2017**, *55*, 814–820.

(164) ElMahmoudy, M.; Inal, S.; Charrier, A.; Uguz, I.; Malliaras, G. G.; Sanaur, S. *Macromolecular Materials and Engineering* **2017**, *302*, 1600497.

(165) Strakosas, X.; Sessolo, M.; Hama, A.; Rivnay, J.; Stavrinidou, E.; Malliaras, G. G.; Owens, R. M. *Journal of Materials Chemistry B* **2014**, *2*, 2537–2545.

(166) Solazzo, M.; Krukiewicz, K.; Zhussupbekova, A.; Fleischer, K.; Biggs, M. J.; Monaghan, M. G. *Journal of Materials Chemistry B* **2019**, *7*, 4811–4820.

(167) Fornasini, P., *The Uncertainty in Physical Measurements: An Introduction to Data Analysis in the Physics Laboratory*; Springer New York: 2008; 289 pp.

(168) Elgrishi, N.; Rountree, K. J.; McCarthy, B. D.; Rountree, E. S.; Eisenhart, T. T.; Dempsey, J. L. *Journal of Chemical Education* **2018**, *95*, 197–206.

(169) McCarthy, B. D.; Martin, D. J.; Rountree, E. S.; Ullman, A. C.; Dempsey, J. L. *Inorganic Chemistry* **2014**, *53*, 8350–8361.